Heavy alkali-metal intercalated fullerenes under high pressure and high temperature conditions: Rb6C60 and Cs6C60

Roberta Poloni

N^o d'ordre 214–2007 Année 2007

THÈSE

présentée

devant l'UNIVERSITÉ CLAUDE BERNARD - LYON 1

pour l'obtention

du DIPLOME DE DOCTORAT

arrêté du 7 août 2006

présentée et soutenue publiquement le

31 Octobre 2007

par

Roberta POLONI

TITRE:

Heavy alkali metal-intercalated fullerenes under high pressure and high temperature conditions: Rb_6C_{60} and Cs_6C_{60}

Directeur de thèse

Prof. Alfonso SAN MIGUEL

JURY:	Pascale Launois	*Rapporteur*
	Bertil Sundqvist	*Rapporteur*
	Xavier Blase	*Président*
	Marco Saitta	*Examinateur*
	Kosmas Prassides	*Examinateur*
	Alfonso San Miguel	*Directeur*
	Sakura Pascarelli	*Codirecteur*

Contents

Introduction

The identification of the C_{60} molecule by Kroto *et al.* [1] and the invention of a method of isolation of bulk quantities by Krätschmer *et al.* [2], have led to intense studies of the resulting materials. The similarity of the C_{60} structure with the geodesic domes of R. Buckminster Fuller [3] has given rise to the name *fullerenes* for the C_n molecules and to *buckminsterfullerene* or *buckyball* to the C_{60} molecule in particular.

Very soon, Haddon *et al.* [4] found that the intercalation of alkali metal atoms in solid C_{60} led to metallic behavior. Subsequently, in the last two decades, many experimental and theoretical studies followed in order to fully characterize and compare the solid C_{60} with its different compounds. In particular, many of these materials have attracted much attention due to the great variety of physical properties observed in these systems at both ambient and extreme conditions. We underline two of these properties with a potential wide range of applications in the everyday life. These are, the extremely high "hardness" (around 200–300 GPa) of three-dimensional (3D) polymerized-C_{60} structures obtained at high pressure (HP) and high temperature conditions (HT) [5] and secondly, the relative high superconducting critical temperature found in various fullerides with the M_3C_{60} stoichiometry [6, 7, 8] (for Cs_3C_{60} T_c=40 K).

The synthesis of new materials, displaying both high hardness and superconducting properties was the initial motivation of my thesis, as explained in more detail in chapter 1. Such materials consist of 3D C_{60} polymers obtained in presence of alkali metal atoms. In the majority of the cases, the C_{60} polymerization consists of a [2+2] cycloaddition, meaning that two double bonds of two neighbouring molecules break up in order to form two different σ bonds between the molecules. In the so formed "four membered ring" (i.e. the connection ring between two molecules including four carbon atoms) each carbon atom is covalently bonded to four other carbon atoms through sp^3 hybridized bondings.

In this study we coupled the presence of heavy alkali ions [9, 10], whose pressure behaviour has been observed to favour the $sp^2 \rightarrow sp^3$ transition, with the application of HP and HT conditions in order to synthesize three-dimensional (3D) polymerized C_{60}

structures starting from the body-centered cubic Rb_6C_{60} and Cs_6C_{60} systems.

These new materials, consisting of 3D polymerized C_{60} molecules connected through small carbon nanocages having partial sp^3 character, are expected to exhibit a high electron-phonon coupling parameter which could lead to superconductors with critical temperature exceeding 200 Kelvin [11, 12, 13].

Nevertheless, as in most experimental PhD theses, our initial aim was frustrated by several technical problems and also by some unexpected results. In order to clarify this, in the following I want to briefly present the history of my thesis. From the beginning, we had to face different experimental problems concerning the synthesis of the samples and their high reactivity. In particular, we soon realized that the synthesis of the Rb_6C_{60} and Cs_6C_{60} compounds was a difficult task. The appendix A of this thesis briefly mentions the procedure that we followed for the sample synthesis and how we finally managed to obtain pure compounds.

Subsequently, due to the extremely high sensitivity of the M_6C_{60} fullerides to air and humidity, their manipulation was done in inert atmosphere making the preparation of the high pressure cell containing the sample, for x-ray measurements (discussed in chapter 3) extremely difficult. In addition, during the experiments, in many cases the measurements showed that the contamination of the sample occurred either during the sample loading or during the transport of the cell from the glove box to the high pressure cell, adding more complications to the experiments.

Then, after the first studies performed under extreme conditions, we soon realized that our purpose, i.e. the synthesis of 3D C_{60} polymers, was difficult to achieve. On the contrary, we observed that the two systems exhibit a wide pressure range of stability, more than twice as large as the stability range of the non-intercalated solid C_{60}. After several x-ray studies, we concluded that the presence of heavy alkali metal atoms and hence, of charge transfer from the Rb and Cs atoms to the molecules, should be responsible for such pressure stabilization of the fullerenes and therefore of the solid structure.

Moreover, it soon turned out that the pressure evolution of the two systems presented slightly different features. For instance, Raman experiments performed at room temperature, showed a continuous evolution of the Raman modes up to 45 GPa in Cs_6C_{60}, while a reversible Raman transition was observed at around 35 GPa in Rb_6C_{60}.

For these reasons we decided to perform *ab initio* calculations in order to better understand the different structural evolutions of the two systems and the stability of both compounds under pressure. Moreover, we expected to clarify the importance of the presence of the alkali metal atoms in such systems and in particular the implication of the

presence of ionic interactions on the pressure evolution and stability of the C_{60} molecules.

We performed x-ray absorption spectroscopy (XAS), x-ray diffraction (XRD) and Raman spectroscopy measurements on the two systems in a wide range of pressure and temperature in order to check for the occurrence of phase transitions leading to the formation of high-dimensional polymers. In addition, *ab initio* calculations were performed in order to better understand the results obtained from the experiments.

The XAS and XRD data have been collected at the ESRF (European Synchrotron Radiation Facility, Grenoble) and the Raman scattering data have been collected at "Laboratoire de Science de La Terre" at the ENS (École Normale Supérieure, Lyon). The *ab initio* DFT calculations have been performed in collaboration with the CECAM (Centre Européen de Calcul Atomique et Moléculaire).

Chapter 1

The C_{60} fullerene and the heavy alkali metal-intercalated fullerenes

This chapter firstly presents the motivation for this work and then describes the main properties of the isolated C_{60} molecule and of its solid structures, including fullerite (solid C_{60}) and alkali fullerides (alkali metal-intercalated fullerenes). Many article and book reviews about fullerenes nowadays exist and it would be a hard task to mention all of them. Nevertheless, the references [14, 15, 16, 17, 18, 19, 20] have been particulary useful and helpful during my thesis work and finally for the writing of this chapter.

1.1 Motivation

This thesis work was primarly motivated by the discovery of superconducting properties in the group-IV based materials (see Figure 1.1). The superconductivity in graphite intercalated compounds has been known for decades [21, 22, 23] but these systems were found to exhibit a very low critical temperature, around 1K. Subsequently, the investigation aimed at the discovery of new high superconducting critical temperature materials has attracted much attention due to their wide range of potential applications in the everyday life.

Carbon-based materials showed a greater variety of systems with superconducting properties. Shortly after the discovery that intercalation of alkali-metal atoms in solid C_{60} leads to metallic behavior [4], the M_3C_{60} (with M alkali metal) compounds where observed to be superconducting. An exhaustive review on the superconducting fullerenes can be found in Ref. [8]. In particular, the critical temperature was measured to be 33 K for $RbCs_2C_{60}$ [6] and 40 K for Cs_3C_{60} [7]. Additionally, more recently, both B-doped diamond [24] and graphite intercalated compounds like C_6Yb and C_6Ca were observed to

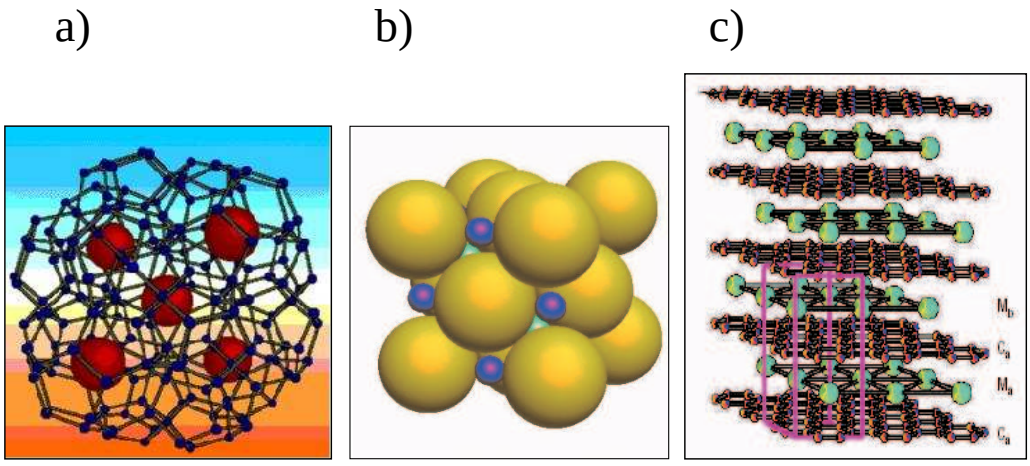

Figure 1.1: *Schematic view of three different column-IV based materials showing superconducting properties: a) the Ba_8Si_{46} silicon intercalated clathrates; b) the A_3C_{60} fullerides and c) the graphite intercalated compounds like C_6Ca.*

be superconducting with transition temperature of 4 K, 6.5 K and 11.5 K [25], respectively.

Very soon, the discovery of superconductivity in such nanostructured carbon systems motivated the investigation of the superconductivity on intercalated silicon clathrates which constitute nanocage-based materials. The maximum measured critical temperature on these systems is 8K, obtained in the Ba_8Si_{46} compound [26].

Subsequently, many theoretical studies were performed in order to explain the mechanism responsible for superconductivity in all these systems [11, 12, 27]. In the majority of the cases, the presence of a high transition temperature was understood, according to the BCS theory, in terms of strong electron-phonon interactions. This theory (whose name derives from its developers Bardeen, Cooper and Schrieffer) interprets the superconductivity as a macroscopic quantum mechanical effect. It proposes the formation of *Cooper pairs*, i.e. paired electrons with opposite spin, whose attraction is mediated by the lattice distortion (phonon). The Cooper pairs are thus responsible for carrying the supercurrent. The McMillan formula for the superconducting critical temperature within the BCS theory is :

$$T_c \propto (\hbar\omega_{ph}) exp\Big(\frac{-1}{N(\epsilon_F)V}\Big) = (\hbar\omega_{ph}) exp\Big(-\frac{1}{\lambda}\Big) \tag{1.1}$$

where ω_{ph} is the average intramolecular phonon frequency, V is the electron-phonon interaction potential and $N(\epsilon_F)$ is the density of states at the Fermi energy. The $\lambda = N(\epsilon_F)V$ parameter is known as the electron-phonon coupling parameter. Hence, by increasing either V or $N(\epsilon_F)$ T_c also increases.

In Ref. [11], Connétable *et al.* showed that the superconductivity is an intrinsic property of the sp^3 silicon network and that carbon clathrates are predicted to yield large critical temperatures with an effective electron-phonon interaction 10 times larger than in the superconducting A_3C_{60} systems. A previous study performed by Breda *et al.* [13] showed that the electron-phonon coupling parameter λ increases for small fullerenes and the smaller the fullerene, the higher is the critical temperature. In the particular case of the fullerene C_{28} they demonstrated that the superconducting critical temperature for C_{28}-based systems is expected to be around 8 times higher than in the A_3C_{60} fullerides ($T_c(C_{28})=8T_c(C_{60})$) leading to very high critical temperatures, close to ambient temperature. Moreover, they affirm the central role of the sp^3 curvature induced hybridization on the electron-phonon coupling, as also shown by Connétable *et al.* [11].

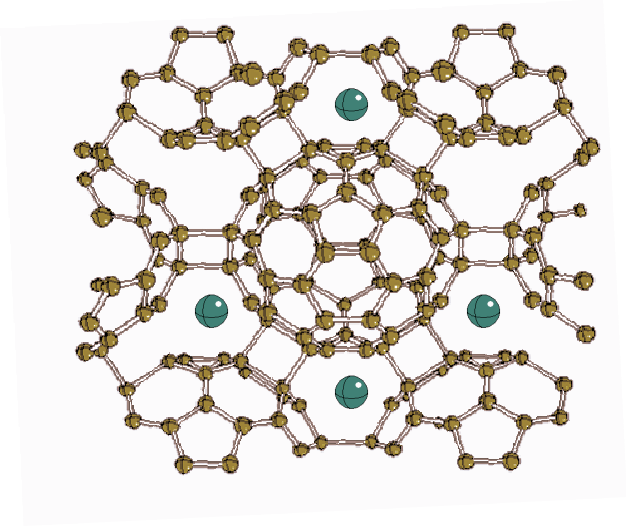

Figure 1.2: *Picture showing a possible 3D polymerization starting from heavy-alkali metal intercalated fullerenes presented in section 1.4 . The small nanocages formed between the fullerenes have sp^3 hybridized bondings making possible a high electron-phonon coupling and thus a high T_c.*

All these interesting results motivated this work, whose goal was the synthesis under high pressure and high temperature conditions of three-dimensional (3D) polymers of heavy alkali-metal intercalated C_{60}, starting from the Rb_6C_{60} and Cs_6C_{60} systems, in order to obtain very high critical temperature superconductors. The C_{60} polymerization has actually been observed to form through the formation of sp^3 hybridized covalent intermolecular bonds. Moreover, if 3D polymerization is achieved, this will possibly lead to the formation of small fullerenes (nanocages formed by a few C atoms) between the C_{60}, as shown in Figure 1.2, allowing to obtain a high electron-phonon coupling parameter.

The so formed carbon clathrates will exhibit a high superconducting critical temperature due to the presence of small nanocages between the fullerenes and to the presence of sp^3 hybridized bonds.

The intercalation with heavy alkali metal ions is important firstly, for increasing the density of state $N(\epsilon_F)$ at the Fermi level and secondly because they have been observed to favour, under pressure, the $sp^2 \rightarrow sp^3$ transition (graphite $\rightarrow$ diamond) in carbon. In particular, the ability of metals to act as catalysts for the conversion of graphite to diamond increases with the increase of its number of electrons in the *d*-orbitals [10] and in metallic cesium a gradual pressure-induced 6s $\rightarrow$ 5d electronic transition is observed from ambient pressure up to 6 GPa [9] .

In addition, the second motivation for this study concerning the formation of superhard materials, is given by the experimental and theoretical discovery of the extremely high "hardness" properties of the three-dimensional C_{60} polymers [28, 5, 29], displaying a high bulk modulus value around 280 GPa. More details about three-dimensional polymers are given in section 1.3.

In conclusion, the aim of this work was to synthesize 3D polymerized C_{60} structures in presence of heavy alkali metal ions under HP and HT conditions, in order to obtain new materials displaying both high hardness and superconducting properties.

1.2 The C_{60} fullerene

"... It is hardly original to state that the identification of the C_{60} molecule by Kroto *et al.* [1] and the subsequent discovery by Krätschmer *et al.* [2] of a simple method to produce large amounts of this, must be counted among the most important scientific discoveries during the last three decades of this century ..." from Ref. [18].

Subsequently, the C_{60} fullerene has been largely and extensively studied and in this section we summarize the main properties of this molecule.

1.2.1 Generalities

In the C_{60} molecule the carbon nuclei reside on a sphere of about 7 Å diameter. More precisely, the atoms are positioned at the 60 vertices of a truncated icosahedron structure with 90 edges, 12 pentagons and 20 hexagons. Two differents C-C bond lengths exist in C_{60} and they measure 1.40 and 1.46 Å. The 30 short bonds, are double bonds and lie on the edges that are shared by two hexagons. The longer ones, that are single bonds, lie at

the 60 edges shared by a hexagons and a pentagon. In Figure 1.3 the double and single bonds are reported in yellow and in red, respectively.

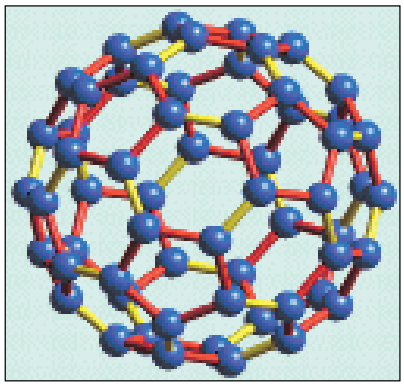

Figure 1.3: *Schematic view of the C_{60} molecule*

Symmetries of the C_{60} molecule include the inversion symmetry, the mirror planes, the rotation by 72° and 144° around axes piercing the centres of two opposing pentagons, 120° rotations around axes through opposing hexagons and 180° rotations around the axes going through the midpoints of opposing double bonds. The relationship of the 120 possible different symmetry operations defines a symmetry point group equivalent to the icosahedral I_h group. This group can be decomposed into irreducible representation denoted by A, T_1, T_2, G and H of dimensionality d=1,3,3,4 and 5, respectively. Due to the inversion symmetry, the representations come in pairs with symmetric and antisymmetric character, yielding g and u labels, respectively, for each representation[1]. The electronic states and molecular vibrations are labelled according to the irreducible representations, using lower- and upper-case characters, respectively. For example, t_{1u} labels a threefold-degenerate asymmetric molecular electronic state and T_{1u} denotes a threefold-degenerate asymmetric vibrational mode. For a more detailed discussion of the symmetry group and its application to C_{60} we refer the reader to the extensive literature on the subject reported in Ref. [17].

1.2.2 Electronic structure

As the carbon atom has 4 valence electrons ($2s$+$2p$), the C_{60} molecule has 240 valence electrons. Each atom forms three σ bonds to its neighbours, using up to a total of 180

[1]Notice that the number of elements in a d-dimensional representation is equal to d^2, thus in this case the total number of elements in the group is indeed $120=2(1^2+3^2+3^2+4^2+5^2)$. The factor 2 stands for the u and g symmetries.

electrons for this purpose. These electrons stabilize the structure but do not contribute to the conduction. These σ bonds are covalent bonds formed between the not purely sp^2 hybridized orbitals. In fact, because of the curvature of the C_{60} surface, the "fullerene hybridization" falls between graphite (sp^2) and diamond (sp^3)'s.

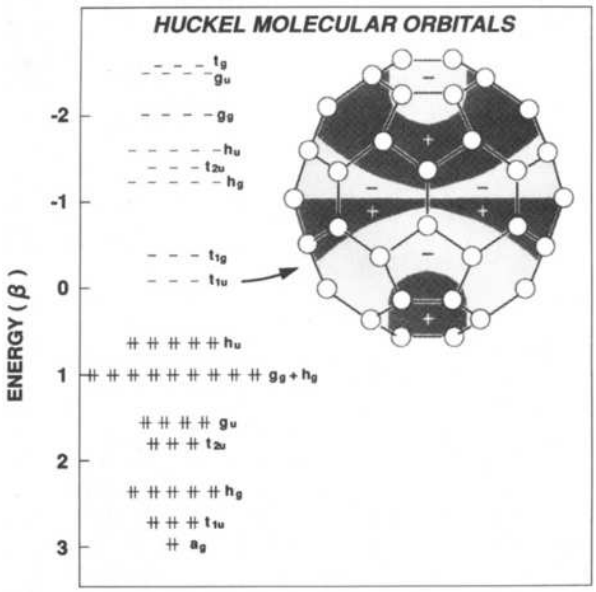

Figure 1.4: *Hückel* molecular orbitals and schematic illustration of the t_{1u} wavefuncion (from Haddon [30]).

The remaining 60 electrons are distributed around the molecule on orbitals that originate from the C-C π orbitals. These orbitals are somewhat similar to the π electron orbits of a graphene plane with the difference that in C_{60} they are not truly delocalized around the six-membered carbon ring (as in graphene) but they are distributed over the 30 short bonds as discussed in the previous section.

The inclination of the theoretician is to first simplify to the lowest possible level and for the spherical C_{60} molecule this leads to a model for the C_{60} electronic structure which considers the electrons confined into a sherical potential. In this case the states are labelled by quantum numbers n, l and m. Soon after, it was clear that this approximation was not reasonable and that the discrete nature of the C_{60} must be considered by taking into consideration the true atomic potential.

When considering the true atomic potential in the fullerene, l is no more a good quantum number and the electronic orbitals are labelled according to the irreducible representations of the icosahedral symmetry group. The correspondance between the spheric and the icosahedral symmetry given by the the relationship between the spherical har-

monics of quantum number l and the irreducible representations of the I_h point group is:

s→a_g

p→t_{1u}

d→h_g

f→t_{2u}+g_u

g→g_g+h_g

h→hu+t_{1u}+t_{1g}

Hence, the electronic structure of the neutral C_{60} molecule was first investigated by a number of semiempirical calculations [31], by Hartree-Fock [32] and by both non-self-consistent [33] and self-consistent [34] calculations within the local density approximation. Subsequently, much insight into the electronic structure of neutral C_{60} was provided by the Hückel molecular orbital calculations [35] originally treating only the 60 π electrons and later extended to include all 240 electrons of the 60 carbon atoms. This model confirms the picture of the electronic structure of the C_{60} molecule discussed below.

The C_{60} electrons fill all the states up to the h_h level as shown in Figure 1.4. The h_u level which is fivefold-degenerate is completely filled and is the highest occupied molecular orbital (HOMO) while t_{1u} is threefold-degenerate and becomes the lowes unoccupied molecular orbital (LUMO). The HOMO-LUMO gap is around 2 eV.

1.2.3 Molecular vibrations

For a molecule of 60 atoms there are (3×60)-6=174 vibrational modes (the term 6 stands for the three translational and the three rotational modes to be subtracted from the total number of modes). Group theory classifies the 174 modes of the I_h symmetry group molecule into two $2A_g$+$3T_{1g}$+$5T_{2g}$+$6G_g$+$8H_g$ modes and an equal number of antisymmetric (u) counterparts. The symmetries of the molecule cause degeneracies in the vibrational frequencies yielding a total of 46 different vibrational frequencies for the isolated C_{60} molecule, with equal numbers of symmetric and antisymmetric modes. In the I_h symmetry group, only 14 normal modes are Raman ($2A_g$+$8H_g$) and infrared ($4T_{1u}$) active and these have been assigned with certainty while the identification of the remaining 32 silent modes has been difficult due to the complexity of the vibrational spectrum.

1.3 The C_{60} phase diagram

In this section we shortly describe the phase diagram of solid C_{60}, i.e. the fullerite. We firstly present the different phases observed at ambient pressure as a function of temperature and secondly, even if the solid C_{60} phase diagram is still under exploration, we depict the different structures so far observed under high pressure and high temperature conditions.

1.3.1 Low-temperature and low-pressure phases

The fullerite is, at room temperature and ambient pressure, a molecular van der Waals solid. In the solid phase at ambient conditions of pressure and temperature, the molecules have their centers of mass on a face-centered cubic (fcc) lattice (space group $Fm\bar{3}m$). The size of the cubic unit cell is 14.17 Å and the nearest-neighbouring intermolecular distance (between the centres of the C_{60}s) is 10.02 Å. The molecules are orientationally disordered at room temperature and the disorder is dynamic with the C_{60} reorienting very rapidly about their fixed centers and on time average the molecules are undistinguishable. Although the C_{60} molecules were considered as freely rotating it was soon recognized that this assumption was erroneus and that there are pronounced intermolecular orientation correlation even in this fcc phase [36, 37, 38]. In particular, Bragg and diffuse scattering data together with some theoretical models have proved the coexistense of several favorable configurations present with different probabilities [39].

As the temperature is lowered, the rotation of the molecules slows down and below 260 K the molecules become orientationally ordered. The basic structure of this low-temperature phase is identical to that of the fcc phase except that the four molecules in the cubic unit cell have different orientations, changing the fcc symmetry into a simple cubic (sc) structure of $Pa\bar{3}$ symmetry. In this phase, there are two possible orientations obtained by rotating the molecules by 38° and 98° respectively around the <111> axes of the crystal with respect to the "standard" orientation [41]. These orientations are also known as H orientation and P orientation, respectively. In particular, the electron-rich double bonds on one molecule face the electron-poor centres of hexagons (H-oriented) and (P-oriented) pentagons respectively on its neighbour, as schematically shown in Figure 1.5. The energy difference between the two configurations is very small and the fraction of molecules in the more stable P orientation continuously increases from 60% at 260 K up to 84% at 90 K. Below this temperature, the thermal energy becomes too small compared to the energy threshold between the two states and below 90 K this orientational disorder

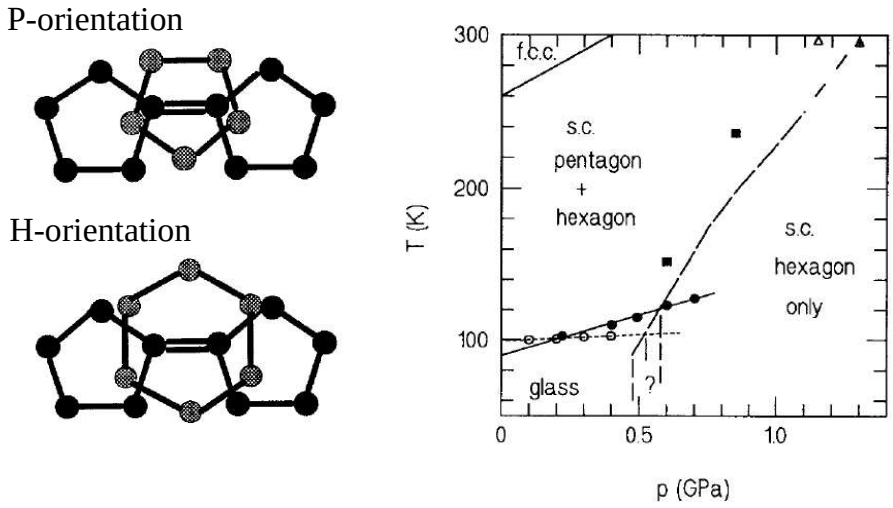

Figure 1.5: *The left panel reports the two different H- (bottom) and P-orientation (top) of the molecules in the simple cubic structure. Figure from [18]. The right panel shows the low-temperature phase diagram of C_{60} reported in Ref. [40].*

becomes frozen and an orientational glass is formed. In Figure 1.5 we show the low temperature phase diagram reported in Ref. [40].

1.3.2 High-temperature and high-pressure phases

The synthesis of new C_{60} phases by application of high pressure and high temperature on pristine C_{60} has attracted a lot of attention, in the last ten years, due to the extraordinary properties of these new phases [18].

At room temperature and relative low pressure, a first order fcc $\rightarrow$ sc transition is observed at around 0.2 GPa where molecules can jump between two different orientational states, the H and the P orientations, mentioned in the previous section. Above this pressure, the fraction of molecules in the H orientation has been observed to increase for increasing pressure [42] but the "line" determining the P $\rightarrow$ H orientational ordering transition is not well investigated.

When applying higher pressure to solid C_{60}, due to the extremely low compressibility of fullerenes compared to the "interstitial volume" between molecules (as shown both by previous works [43, 44] and in also in chapter 4 of this thesis), the molecules weakly bonded by van der Waals forces approach each other rapidly. As the distance between carbon atoms on different molecules becomes comparable to the intramolecular C-C bond lengths these unsaturated molecules are able to develop chemical bonds. At room temperature, under non-hydrostatic pressure Duclos *et al.* [45] observed a transition that was

probably associated to polymerization. Soon after, Snoke *et al.* [46] observed an irreversible transition by Raman spectroscopy towards an amorphous phase around 22 GPa. Additionally, Núñez-Regueiro *et al.* verified the existence of an irreversible transition after 20 GPa. After quenching from a rapid non-hydrostatic compression they observed that that transition was associated to the formation af polycrystalline diamond [47].

The high pressure and high temperature diagram of C_{60} exhibits many different phases and it is still under exploration due to its complexity [48]. Nevertheless, in the following we briefly report the nowadays knowledge of the C_{60} phase diagram by summarizing the x-ray diffraction results performed on recovered metastable high-pressure- and high-temperature-treated materials. Since the P-T phase diagram of C_{60} has been mostly obtained by *ex situ* investigation, it should be rather considered as a "P-T reaction diagram". This is reported in Figure 1.6.

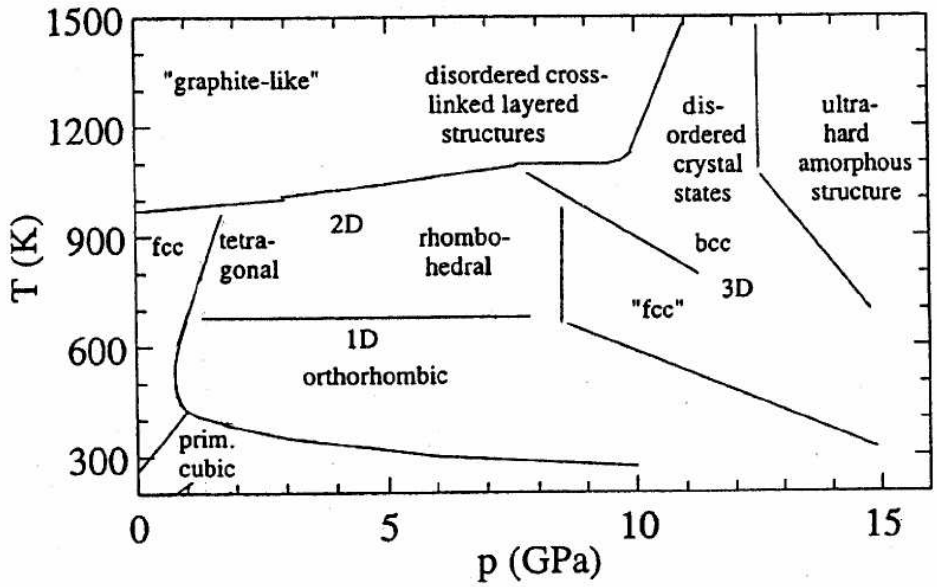

Figure 1.6: *"P-T reaction diagram" of C_{60} fullerite. Picture from Ref. [49].*

By looking at Figure 1.6, it turns out that under high pressure and high temperature conditions, there is the formation of covalent bonds between molecules, i.e. the C_{60} polymerization, reported by different groups [50, 28, 51, 52]. All the high pressure studies showed that, by increasing both pressure and temperature, a progressively higher degree of the C_{60} polymerization was obtained (see Figure 1.6).

In the majority of the cases, the polymerization takes place *via* [2+2] cycloaddition, meaning that two double bonds of two neighbouring molecules break up in order to form two different σ bonds between the molecules. In the so formed "four membered ring" (i.e.

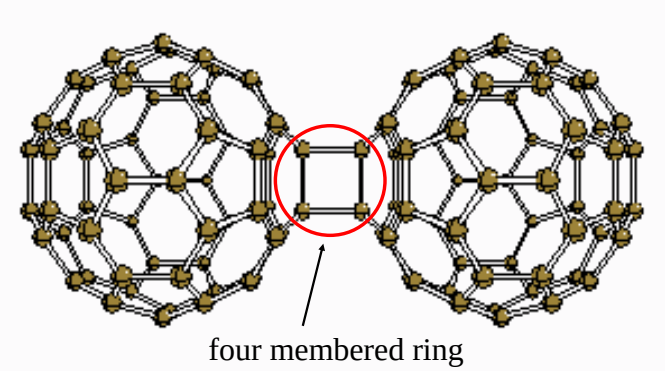

Figure 1.7: *Dimerization by [2+2] cycloaddition: the red ring indicates the four membered ring, i.e the connection ring between two covalently bonded molecules including 4 C atoms.*

the connection ring between two molecules including 4 C atoms, see Figure 1.7) each C atom is covalently bonded to four other C atoms through a sp^3 mixed sp^2 hybridization.

Different polycrystalline structures consisting of one (1D) and two-dimensional (2D) polymers have been obtained and well characterized [53]. In parallel, several works [54, 50, 52] concerning both Raman and x-ray diffraction studies have been reported on single crystals of dimerized C_{60}, 1D chains and 2D polymerized C_{60}, obtained after high pressure and high temperature treatment. In particular, after a compression between 1 and 8 GPa at 600 K, 1D polymerization (see Figure 1.8) in an orthorhombic lattice was identified and the structure can be viewed as a distortion of the C_{60} fcc cell by compressing the molecule along the <110> fcc direction. The space group reported in Ref. [53] for the orthorhombic structure is the $Immm$ while in Ref. [50] it was found to exhibit $Pmnn$ symmetry. The <110> direction was found to correspond to the polymerization direction and the inter-molecular distance between the centres of two polymerized fullerene is 9.26 Å according to Ref. [53] and 9.14 Å in Ref. [50].

At higher temperature (around 900–1000 K), between 4 and 9 GPa, a mixed tetragonal and rhombohedral 2D polymerized phase is obtained (see Figure 1.8). The tetragonal phase ($Immm$ space group in Ref. [53] and $P4_2/mmc$ in Ref. [52]) results from the in-plane compression of the (001) fcc planes and the distance between the centres of two polymerized molecules is 9.09 Å [53] and 9.02 Å [52]. The rhombohedral phase ($R\bar{3}m$ space group) can be viewed as an in-plane compression of the (111) fcc plane where the nearest-neighboring intermolecular distance is 9.19 Å.

The exploration of the C_{60} phase diagram under higher pressure and higher temperature conditions, performed by Blank *et al.* [55, 49, 56], leads to the synthesis of graphitic-amorphous mixed phases with sp^2-sp^3 mixed sites. These materials exhibit a

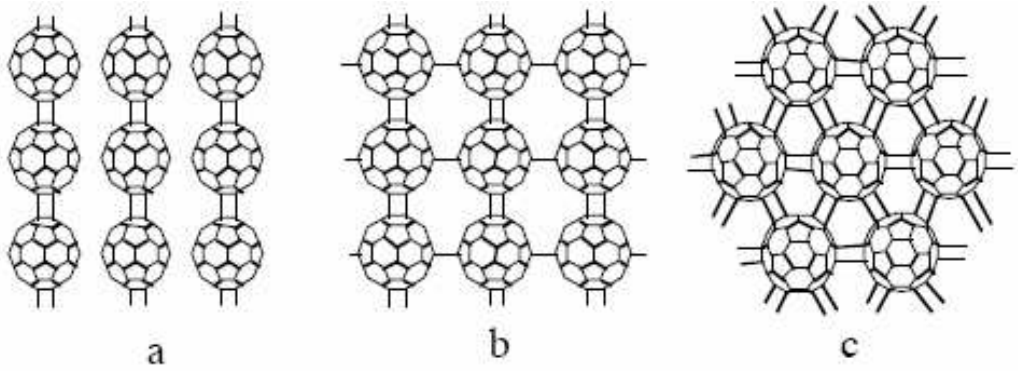

Figure 1.8: *Different polymers structures: (a) orthorhombic structure where each molecule is covalently bonded to the two nearest neighbouring molecules along a <110> fcc direction; (b) tetragonal lattice where each molecule is covalently linked to its four neighbouring molecules in a (100) fcc plane; (c) rhombohedral structure where each molecule is covalently linked to its six other neighbouring molecules molecules in a (111) fcc plane. The picture is from Ref. [51].*

bulk modulus between 590 and 640 GPa, exceeding significantly that of diamond (around 440 GPa). A 3D polymerized structure was unambiguougly identified by Marques *et al.* [28]. They observed a polycrystalline phase where intermolecular bonds exist among all the 12 first neighbours of a pseudo face-centered cubic (fcc) C_{60} network. Such a structure was later observed to exhibit a very high bulk modulus coefficient, around 280 GPa. More recently, Yamanaka *et al.* [57] obtained single crystals of 3D polymers where the covalent bonding between the molecules is achieved through [3+3] cycloaddition. The new synthesized materials consisted of a 3D metallic crystalline carbon network with fullerenes having a cuboidal shape.

1.4 Alkali metal-intercalated fullerenes

The early discovery by Haddon *et al.* [4] that C_{60}, like graphite, could be intercalated with alkali metal atoms to form metallic compounds immediately sparked much interest.

In the close-packed fcc structure of pristine C_{60} the interstitial sites have either octahedral (O) or tetrahedral (T) sites. The tetrahedral sites are smaller and there are twice as many of them as octahedral sites. The M_nC_{60} (n=1, 2, 3, 4, 6, 10) compounds formed by the intercalated alkali metal atoms on the original fcc structure of pure C_{60} are commonly known as fullerides (see Figure 1.9).

When the O sites are filled with alkali ions the M_1C_{60} compound is obtained and it

preserves the fcc structure. If the T sites are also filled, the M_nC_{60} with n=2, 3 are formed having again fcc structure. On the other hand, Na and Li are small enough for more than one of them to fit into the O sites and M_nC_{60} systems with n=6 and 10 were made [58].

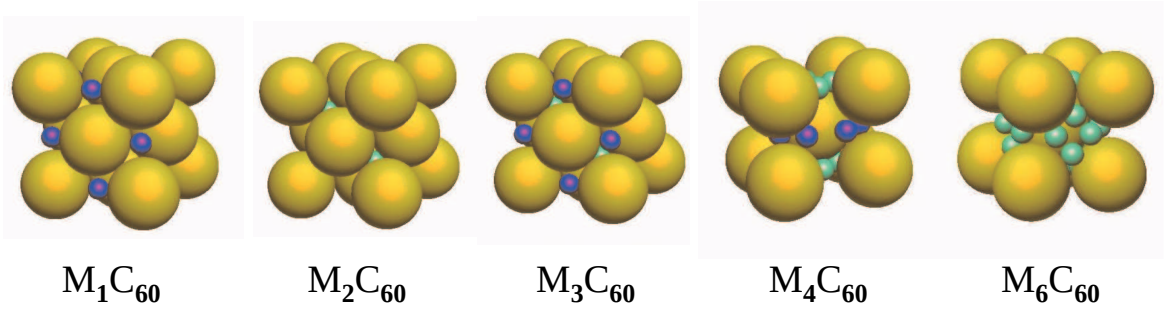

Figure 1.9: *Starting from the right side: in M_1C_{60} all the octahedral (O) sites (dark blue) are occupied (one per molecule); in M_2C_{60} all the tetrahedral (T) sites (light blue) are occupied (two per molecule); in M_3C_{60} both the O and the T sites (one O and two T per molecule) are occupied. In M_4C_{60} the structure is rearranged in a body-centered tetragonal (bct) cell and both the O and the T sites of the bct lattice are occupied. M_6C_{60} adopts a bcc lattice and all its T sites are occupied.*

For $n > 3$, the fcc is rearranged and for n=4 and 6 the body-centered tetragonal (bct) and body-centered cubic (bcc) structures are formed, respectively.

In contrast to pristine fcc C_{60}, in these intercalated materials the nearly free rotation of the molecules is hampered by the ionic interactions.

Let's briefly mention the main properties of fullerides.

The study of these compounds actually increased significantly after the discovery of superconducting properties in the M_3C_{60} compounds [59, 60, 6, 61].

The M_nC_{60} compounds (M=K, Rb and Cs) with n=1, undergo a structural transition from a high-temperature monomer to a polymer phase for T $<$ 350 K [62, 63]. The 1D polymerized structure displays an orthorhombic structure and the chains of fullerenes are linked by [2+2] cycloaddition and consequently by "double" C-C bonds (two covalent bonds).

In the C_{60}-based compounds intercalated with light alkali atoms (Li and Na) the ionic interaction between the alkali metal M^{n+} and the fullerene molecule C_{60}^{n-} has been shown to act as a catalyst for the polymerization. In particular, Na_2RbC_{60} and Na_4C_{60} have been observed to spontaneously form 1-D and 2-D polymers, respectively, at ambient conditions [64, 65] through singly bonded C_{60}. More recently the Li_4C_{60} system has been observed to display a 2D polymerization characterized by the coexistence of single and double C-

C bonds [66]. In Figure 1.10 we report the C-C bridging structural motifs observed in different fullerides. Also the $Li_xNa_{(4-x)}C_{60}$ systems (with $0 \leq x \leq 4$), have been observed to form 2D polymers [67].

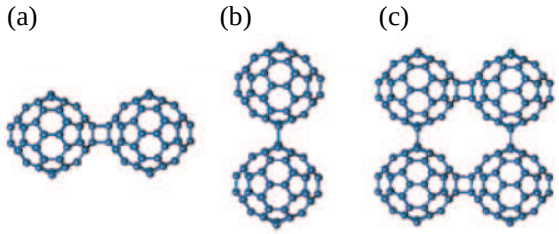

Figure 1.10: *Figure from Ref. [65]. Schematic drawing of the interfullerene C-C bridging structural motifs in fullerides: (a) [2+2] cycloaddition in RbC_{60}; (b) single C-C covalent bonds in Na_2RbC_{60}; (c) mixed bondings in Li_4C_{60}.*

For stoichiometries with $3 < x \leq 6$, 2-D and 3-D polymerized forms have not been observed yet and a detailed study of their phase diagram does not exist.

1.4.1 The Rb_6C_{60} and Cs_6C_{60} systems

In this section, we briefly describe the systems studied during this thesis work, i.e. Rb_6C_{60} and Cs_6C_{60}. In the M_6C_{60} compounds (with M=K, Rb and Cs), characterized by x-ray powder diffraction by Zhou *et al.*, [68] the crystalline phase adopts a bcc structure with $Im\bar{3}$ space group.

Contrary to the case of solid C_{60}, in the intercalated-fullerenes systems, at ambient conditions, the rotation of the C_{60} molecules is substantially hindered. In particular, when large cations are introduced, such as in this case, no molecular rotation is observed as it is hampered by the presence of strong ionic interaction between the negatively charged C_{60} molecule and the positively charged alkali metals.

In this structure two equivalent C_{60} molecules per cell are centered at (0,0,0) and (1/2, 1/2, 1/2) oriented with their two-fold axes along the cube edges. Twelve alkali atoms per cell are located in the 12(e) positions at (0, 0.5, 0.2822) and (0, 0.5, 0.2781) in Rb_6C_{60} and the Cs_6C_{60}, respectively. Each C_{60} is surrounded by 24 alkali metal atoms and each alkali ion is in a distorted tetrahedral environment of four C_{60}'s. Figure 1.11 shows in more detail the bcc unit cell as reported in Ref. [68].

The Rb_6C_{60} and the Cs_6C_{60} systems have a cubic lattice parameter of 11.54 and 11.79 Å, respectively [68] (at ambient pressure and room temperature). The nearest-neighbour

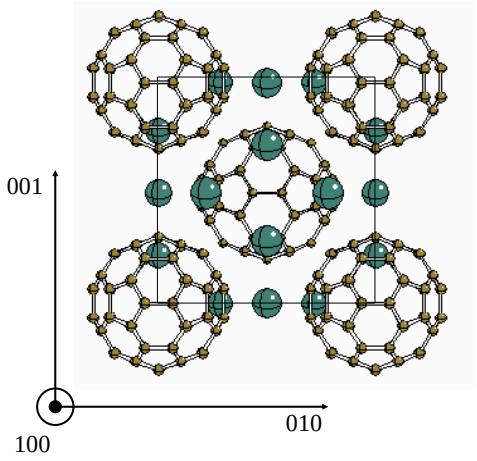

Figure 1.11: *Bcc unit cell of Rb_6C_{60} and Cs_6C_{60}.*

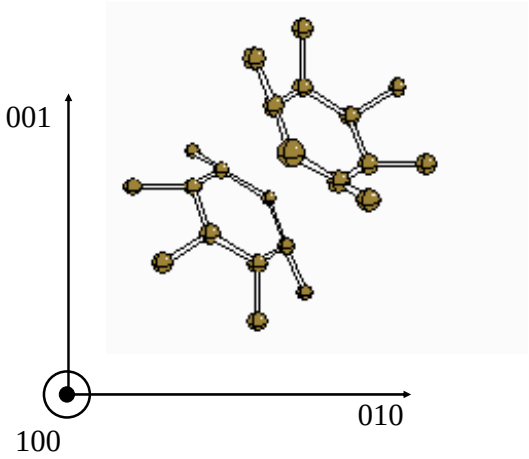

Figure 1.12: *Facing mechanism of two nearest-neighbour molecules along the <111> bcc direction: a hexagon of one molecule parallely faces a hexagon of the neighbouring molecule.*

distance between two molecules along the <111> bcc direction is 9.99 and 10.21Å for the Rb and Cs case, respectively. This distance corresponds to the half-diagonal length of the cubic lattice ($\frac{\sqrt{3}a}{2}$). Figure 1.12 reports the facing mechanism of two nearest-neighbour molecules along the <111> bcc direction: a hexagon of one molecule parallely faces a hexagon of the neighbouring molecule.

A theoretical study performed by Andreoni *et al.* [69] reported that the ionic interactions in K_6C_{60} and Rb_6C_{60}, due to alkali intercalation, give rise to a distortion of the C_{60} compared to the isolated molecule as shown in Figure 1.13. Such distortion which preserves the T_h symmetry, can be viewed as a slight breathing of the C_{60} compared to the free molecule. In particular, they observed that the single bonds which had equal

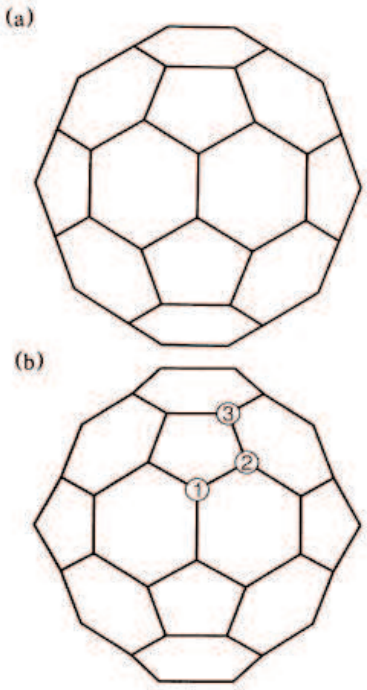

Figure 1.13: *Figure from Ref. [69]. C_{60} viewed from a two fold symmetry axis: (a) isolated molecule, (b) in the K_6C_{60} crystal. The atomic displacements have been amplified by a factor 5 to make them more clearly visible. The (1), (2) and (3) carbon atoms are the three non-equivalent sites predicted for the T_h symmetry.*

lengths in the isolated C_{60} now split into three groups of slightly different lengths. More remarkably, the six double bonds that point towards the Cartesian axes undergo substantial lengthening to the point of becoming the largest ones. Nevertheless, no experimental evidence of such deformation has been provided up to now.

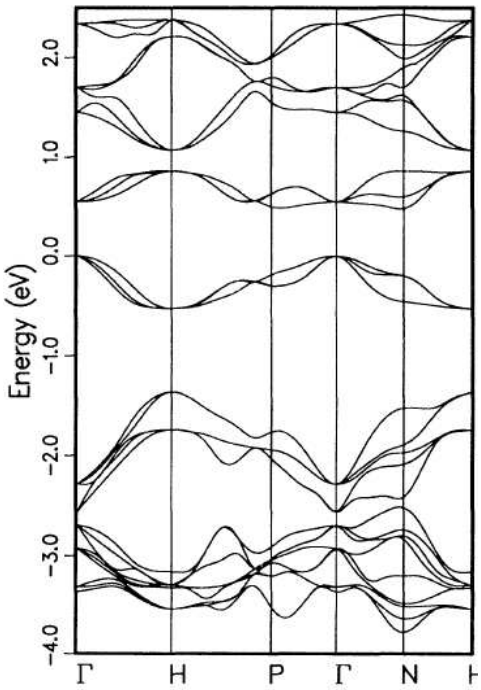

Figure 1.14: *Figure from Ref. [70]. Electronic bands structure of crystalline K_6C_{60}. The zero energy is set to the valence-band maximum.*

Concerning the electronic structure of these systems, it was first studied by first-principles calculations by Erwin and Pederson [70] for the particular case of K_6C_{60}. They

calculated the energy bands of solids potassium intercalated fullerenes K_nC_{60}, n=0, 3, 4, 6 and observed that they correspond to broadened versions of the molecular orbitals (MO) energies. Although differences in the bands themselves are observed for the four systems due to the different symmetries, the presence of alkali metals does not contribute to modify significantly the band structure.

For the K_6C_{60} system, they observed a complete charge transfer from the K atoms to the molecule meaning that each K atom transfers its $4s$ electron to the C_{60} which is stabilized in a high charge state with six additional electrons. The obtained electronic band structure, reported in Figure 1.14, shows that the systems is an insulator with an indirect gap of 0.48 eV. The highest occupied band (t_{1u}), deriving from the t_{1u} MO of the isolate C_{60}[2], is approximately 0.5 eV while the lowest unoccupied band (t_{1g}) deriving from the t_{1g} MO shows appreciable dispersion, in the range of 1.0–1.5 eV.

Very few high pressure studies on the evolution of both electronic and solid structure of Rb_6C_{60} and Cs_6C_{60} have been reported up to now. The only existing high pressure study has been performed by x-ray diffraction on Rb_6C_{60}. In this work, carried out by Sabouri-Dodaran *et al.* [71] the C_{60} molecules are observed to be stable in the bcc phase at least up to 22 GPa, which also corresponds to the amorphization pressure in solid C_{60}. This result stimulates further studies in order to precisely determine the stability range of the C_{60} molecule in these fullerides and compare it to the case of the non-intercalated solid C_{60}.

[2]We remind here, that in the isolated C_{60} molecule, the t_{1u} orbital correponds to the LUMO (lowest unoccupied molecular orbital). In the solid K_6C_{60}, the t_{1u}, originating from the t_{1u} MO, becomes the highest occupied band since it is three-fold degenerate and hence completely filled by the six $4s$ electrons of K atoms.

Chapter 2

Methods

This chapter briefly presents the methods used in this work. It introduces both the experimental methods by describing the principle of each technique, i.e. x-ray absorption spectroscopy, x-ray diffraction and Raman spectroscopy and the key ideas of the *ab initio* DFT calculations. The purpose of this chapter is to provide some fundamental tools in order to allow even the reader not used to some of these methods, to understand the results that we have obtained within this thesis.

2.1 X-ray absorption spectroscopy

X-ray absorption spectroscopy (XAS) is a probe of the local structure around selected atom species in solids, liquids and molecular gases. For atoms in a condensed system, the observed x-ray absorption spectrum is not a smooth function of energy but oscillates for several hundreds eV above the absorption edge. The details of these oscillations, called EXAFS (extended x-ray absorption fine structure), depend strongly on the local atomic environment of the absorbing atom, with a few nearest neighbouring atoms accounting for essentially all the observed variations in the absorption.

X-ray absorption spectroscopy is a useful complement to x-ray diffraction which provides accurate long-range information about the structure of crystalline materials.

In a typical XAS experiment, performed in transmission geometry, the intensity $I(x, E)$ of transmitted x-rays through a sample of thickness x is measured as a function of energy. The loss of x-ray intensity is given by the exponential Lambert-Beer attenuation law:

$$\frac{I(x,E)}{I(0,E)} = e^{-\mu(E)x} \tag{2.1}$$

where $\mu(E)$ is the linear absorption coefficient. As well as depending on the energy of the incident beam, μ also depends on the composition of the irradiated sample. The absorption coefficient $\mu(E)$ is well approximated by a sum of the absorption coefficients of individual atoms, proportional to the x-ray absorption cross section $\sigma(E)$.

In the x-ray region (below approximately 50 keV), the cross section for the interaction of radiation with matter is dominated by photo-electric excitation processes which manifest themselves as sharp rises in the absorption, usually termed edges (i.e. K, L_1, L_2 and L3), when the incident photon has an energy equal to the binding energy of a core-level electron (i.e. $1s$, $2s$, $2p_{1/2}$ and $2p_{3/2}$). Clear oscillations of the absorption coefficent are observed in a wide energy region above the edge (of about 1000 eV). The absence of such modulations in low density systems and gases points to a strict relationship between EXAFS oscillations and the presence of neighbouring atoms.

EXAFS and its local nature are best understood in terms of wave-behaviour of the photo-electron created in the absorption process. The wave associated with the photo-excited electron can be scattered by neighbouring atoms as shown in Figure 2.1 and returns to the photo-absorber. Interference between the outgoing and backscattered components lead to modulations of the final state wavefunction as a function of the electron energy. This in turn modulates the absorption coefficient $\mu(E)$ producing the EXAFS oscillations.

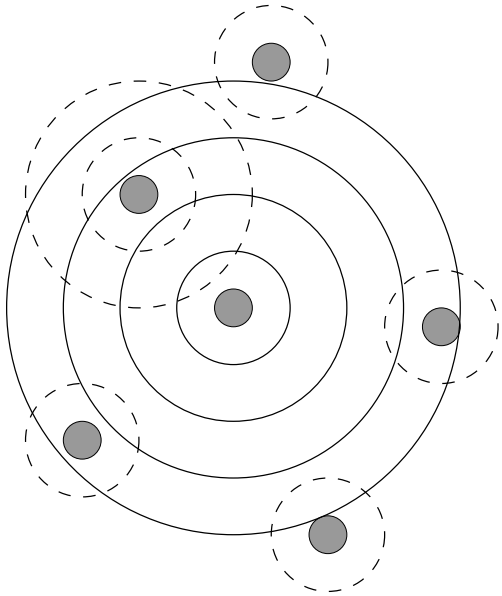

Figure 2.1: *Schematic view of the radial component of the outgoing (continuous line) and backscattered parts (dashed lines) of the photo-electron wave in a condensed system. Inteference between these two components leads to modulations of the final state.*

The x-ray absorption spectrum is traditionally divided into two regimes: x-ray absorp-

tion near edge structure (XANES) and extended x-ray absorption fine structure (EXAFS). Though the two regions overlap and have the same physical origin, this distinction is convenient for the interpretation:

- XANES region: (within about 50-100 eV above the absorption edge) the photo-electron is strongly scattered by the atoms surrounding the photo-absorber and the amplitude of the multiple scattering is important. The shape of the XAS spectra in this region is strongly sensitive to the formal oxidation state and coordination chemistry of the absorbing atom;

- EXAFS region: (from about 80 eV above the edge) the photo-electron has sufficient energy for treating the multiple scattering in terms of distinct two-, three-, ..., n-body contributions. Nevertheless, the two-body contributions are generally the dominant terms.

The EXAFS function is defined as

$$\chi(k) = \frac{\mu(k) - \mu_0(k)}{\mu_0(k)} \tag{2.2}$$

where $k = \sqrt{\frac{2m}{\hbar^2}(E - E_0)}$ is the wave-vector of the photo-electron (E_0 is the core binding energy) and μ_0 is a smooth, atomic-like, background absorption of an "embedded atom", in the ideal absence of neighbouring scatterers.

In the following we report the simple analytic form of the EXAFS signal $\chi(k)$ obtained from the *Diffusion Theory*. It assumes both the approximation of spherical waves for the wavefunction associated to the outgoing and backscattered photo-electrons and the *single scattering* approximation (meaning that it considers only two-body contributions). Even though this formulation assumes the rude single scattering approximation to the problem, it is useful at present because it provides an easy general comprehension of XAS. The final analytic form for equation 2.2 is expressed as:

$$\chi(k) = \sum_j A(r_j, k) \sin[2kr_j + \Phi_j(k, r)] e^{-2\sigma_j^2 k^2} e^{-2r_j/\lambda_j(k)} \tag{2.3}$$

where

- the sum over j involves all the coordination shells around the photo-absorber atom;

- the amplitude factor $A(r_j, k)$ is proportional to N_j, i.e. the number of atoms in the j-th shell and it is inversely proportional to kr_j^2 (r_j is the distance between the photo-absorber site and the atoms in the j shell);

- the $e^{-2\sigma_j^2 k^2}$ term is similar to the diffraction Debye-Waller factor and it is related to the thermal disorder with the difference that in EXAFS σ_j^2 is the mean-square relative displacement (MSRD) of j atom (or shell) with respect to the absorber atom a. The relationships between the EXAFS MSRD and the diffraction mean-square displacement (MSD) is:

$$\sigma_{a-j}^2 = \sigma_a^2 + \sigma_j^2 - 2\sigma_a\sigma_j\rho \tag{2.4}$$

where σ_{a-j}^2 is the EXAFS MSRD and σ_a^2 and σ_j^2 are the MRD of atoms a and j, respectively, with respect to their absolute position; ρ is the correlation factor ($-1 \leq \rho \geq 1$);

- the $e^{-2r_j/\lambda_j(k)}$ term describes the inelastic processes during the propagation of the photo-electron and $\lambda(k)$ is the limited mean-free-path of the electron;

- $\Phi_j(k,r)$ is the phase shift due to photo-electron diffusion from the photoabsorber site and from the neighbouring atoms.

More recently, the EXAFS theory has been further developed in order to take into account *multiple scattering* (MS) components. This leads to information even about many-body distributions. The approach to the solution of the structural problem proposed by Filipponi, Di Cicco and Natoli [72] allows to obtain a linear relationship between the signal and the distribution of atoms around the photoabsorber atom. This approach, employed in the GNXAS [72, 73] code used for the data analysis in this work, is based on the decomposition of the cross section in n-body terms which include all the MS contributions for a given set of n-atoms. For a generic fixed atom configuration surrounding the photoabsorber atom, the EXAFS signal is expressed as a sum of the space integrals of the many-body *irreducible signals* γ^n (where γ^n are dimensionless quantities proportional to the cross section) multiplied by the corresponding n-body density-probability function $g_n(r)$:

$$\begin{aligned}
\langle\chi(k)\rangle &= \int_0^\infty dr\ 4\pi r^2\rho\ g_2(r)\ \gamma^{(2)}(r,k) + \\
&+ \int dr_1 dr_2 d\phi\ 8\pi^2 r_1^2 r_2^2\ \sin(\phi)\ \rho^2\ g_3(r_1,r_2,\phi)\ \gamma^{(3)}(r_1,r_2,\phi,k) + \\
&+ \int dr_1 dr_2 dr_3\ d\phi\ d\Omega\ 8\pi^2 r_1^2 r_2^2 r_3^2\ \sin(\phi)\ \rho^3\ g_4(r_1,r_2,\phi,r_3,\Omega)\cdot \\
&\cdot\ \gamma^{(4)}(r_1,r_2,\phi,r_3,\Omega,k) + \cdots
\end{aligned} \tag{2.5}$$

In this thesis we have considered only two-body contributions to the total $\chi(k)$ signal and for the $g_2(r)$ function we used an analytic non-gaussian function in order to consider

the structural disorder of our systems. This function is usually used to describe asymmetric distribution and its functional form is:

$$g_j(r) = \frac{N_j}{4\pi\rho r^2} \frac{2}{\sigma|\beta|\Gamma(4/\beta^2)} \left[\frac{4}{\beta^2} + \frac{2(r-R)}{\sigma\beta}\right]^{\frac{4}{\beta^2}-1} \exp\left[-\left(\frac{4}{\beta^2} + \frac{2(r-R)}{\sigma\beta}\right)\right] \quad (2.6)$$

where R is the average distance (in this case from the photo-absorber site and the j-th shell), σ is the variance of the distribution and β is the asymmetry parameter (for $\beta \to 0$, $g_j(r)$ becomes a gaussian function).

2.2 X-ray powder diffraction

Powder diffraction is the technique used in this thesis work for the study of the evolution of the crystalline structure of our systems under extreme conditions. It was developed as early in 1913. It is nowadays one of the most important techniques available to material scientists and its success rests essentially on two features:

- a diffraction pattern is determined by the exact atomic arrangement in a material; powder diffraction is an effective method of phase identification;
- in spite of its inherent limitations, powder diffraction provides information not only about the structure (detailed atomic arrangement), but also about the texture and the morphology (anisotropy and particle size) of crystalline matter.

In the method we used to perform x-ray powder diffraction, the sample is illuminated by a monochromatic beam with wavelength λ_0. Different d-spacings of the crystal are measured at different angles (angular dispersive diffraction) of the detector according to Bragg's law:

$$n\lambda_0 = 2d_{h,k,l}sin\theta_{h,k,l} \quad (2.7)$$

where (h,k,l) are the Miller indices associated to the $d_{h,k,l}$-spacing and n is an integer. The intensity of a diffracted line (h,k,l) is given by the following expression:

$$I_{h,k,l} = Sj_{h,k,l}L_{h,k,l}\left|F_{h,k,l}\right|^2 \quad (2.8)$$

where

- S is a constant depending on the incident beam intensity, on the wavelength of the radiation source and on the sample-to-detector distance;

- $j_{h,k,l}$ is the multiplicity for the reflection (h,k,l);

- $L_{h,k,l}$ is the combination of the Lorentz and polarization factors for the diffractometer geometry; in the case of a non polarized monochromatic beam it is equal to $(1+\cos^2 2\theta_{h,k,l})/(\sin^2\theta_{h,k,l}\cos\theta_{h,k,l})$ and

- $F_{h,k,l}$ is the structure factor for reflection (h,k,l) that relates the intensity to the atomic arrangement in the unit cell. The structure factor is given by

$$F_{h,k,l} = \sum_{i=1}^{unit-cell} f_i e^{-B_i \frac{sin^2\theta_{h,k,l}}{\lambda^2}} e^{2\pi i(hx_i+ky_i+lz_i)} \tag{2.9}$$

where x_i, y_i and z_i are the fractional coordinates of atom i in the unit cell, $e^{-B_i \frac{sin^2\theta_{h,k,l}}{\lambda^2}}$ is the isotropic Debye-Waller factor (with $B_i=8\pi^2\sigma_i^2$) and f_i is the atomic scattering factor for atom i defined as:

$$f_i^2 = (f_0 + \Delta f_i')^2 + (\Delta f_i'')^2 \tag{2.10}$$

with $\Delta f_i'$ and $\Delta f_i''$ the real and imaginary parts of the dispersion correction.

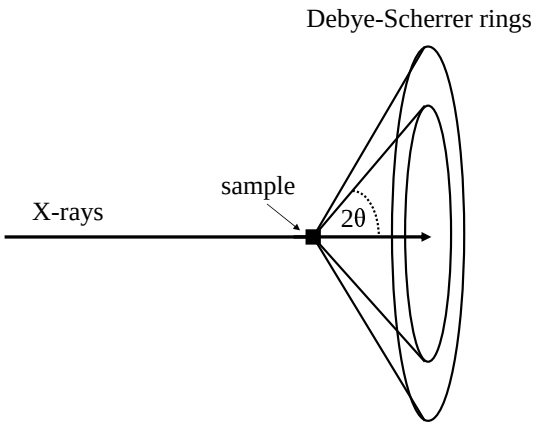

Figure 2.2: *Scheme of the Debye-Scherrer geometry. When the incident monochromatic beam scatters along different cones, their intersection with the detector is observed (Debye-Scherrer rings).*

As an ideal powder sample consists of a large number of small crystallites randomly oriented with respect to each other, the incident beam is scattered symmetrically along different cones whose intersection with the image plate detector gives rise to concentric rings called Debye-Scherrer rings (Figure 2.2). Maxima of intensity of the diffracted beam are observed at those $2\theta_{h,k,l}$ corresponding to the interplanar distances $d_{h,k,l}$.

2.3 Raman spectroscopy

Raman spectroscopy is a spectroscopic technique used in condensed matter physics and chemistry to study vibrational, rotational, and other low-frequency modes in a system. The Raman effect was first observed by C. V. Raman in 1928 [74].

The laser light interacts with phonons or other excitations in the system, resulting in the energy of the detected laser photons being shifted up or down. The shift in energy gives information about the phonon modes in the system. Raman spectra have their origin in the electronic polarization caused by ultraviolet, visible, near infrared, or near ultraviolet range. If a molecule is irradiated by monochromatic light of frequency ν (laser), then, because of electronic polarization induced in the molecule by this incident beam, the light of frequency ν ("Rayleigh" or elastic scattering) as well as that of frequency $\nu \pm \nu_i$ ("Raman" or inelastic scattering) is scattered where ν_i represents a vibrational frequency of the molecule. Hence, Raman spectra are presented as $shifts$ from the incident frequency.

The origin of Raman spectra can be explained by an elementary classical theory. Let's consider a light wave of frequency ν with an electric field $\mathbf{E}$. Since $\mathbf{E}$ fluctuates at frequency ν, we can write

$$\mathbf{E} = \mathbf{E}_0 cos 2\pi\nu t \tag{2.11}$$

where $\|\mathbf{E}_0\|$ is the amplitude and t the time. If a diatomic molecule is irradiated by this light, the dipole moment $\mathbf{R}$ given by

$$\mathbf{R} = \alpha\mathbf{E} = \alpha\mathbf{E}_0 cos 2\pi\nu t \tag{2.12}$$

is induced. Here α is a proportionality constant and is called *polarizability*. If the molecule is vibrating with frequency ν_i, the nuclear displacement $\mathbf{q}$ is written as

$$\mathbf{q} = \mathbf{q}_0 cos 2\pi\nu_i t \tag{2.13}$$

where $\|\mathbf{q}_0\|$ is the vibrational amplitude. For small amplitudes of vibration, α is a linear function of $\mathbf{q}$. Thus, we can write

$$\alpha = \alpha_0 + \left(\frac{\partial\alpha}{\partial q}\right)_0 q \tag{2.14}$$

Here, α_0 is the polarizability at the equilibrium position and $(\partial\alpha/\partial q)_0$ is the rate of change of α with respect to the change in q, evaluated at the equilibrium position. If we combine equations 2.12- 2.14, we have

$$\mathbf{R} = \alpha \mathbf{E}_0 cos2\pi\nu t = \alpha_0 \mathbf{E}_0 cos2\pi\nu t + \Big(\frac{\partial\alpha}{\partial q}\Big)_0 q_0 \mathbf{E}_0 cos2\pi\nu t cos2\pi\nu_i t$$

$$= \alpha_0 \mathbf{E}_0 cos2\pi\nu t + \frac{1}{2}\Big(\frac{\partial\alpha}{\partial q}\Big)_0 q_0 \mathbf{E}_0 \{cos[2\pi(\nu+\nu_i)t] + cos[2\pi(\nu-\nu_i)t]\} \quad (2.15)$$

According to classical theory, the first term describes an oscillating dipole which radiates light of frequency ν (Rayleigh scattering).

The second term gives the Raman scattering of frequencies $\nu + \nu_i$ (*anti-Stokes*) and $\nu - \nu_i$ (*Stokes*). Hence, the Stokes and the anti-Stokes lines appear at lower and higher energy, respectively, compared to that of the incident laser (Figure 2.3). If $(\partial\alpha/\partial q)_0$ is zero, the second terms vanishes. Thus, we can conclude that the vibration is Raman active only if the polarizability changes during the vibration. This is the selection rule for Raman-active vibrations and these can be established from the symmetry properties of the system.

Figure 2.3: *Mechanism of Raman scattering (left panel) and schematic view of a Raman spectra (right panel). The Stokes and anti-Stokes lines are symmetric compared to the Rayleigh line (elastic scattering). The intensity of the Stokes lines is always higher that the anti-Stokes lines due to the Maxwell-Botzmann distribution law.*

Now we discuss the Stokes and anti-Stokes lines in terms of energy of the molecule. In the case of Stokes lines, the molecule at ν_0=0 is excited to the ν_1=1 state by scattering light of frequency $\nu_0 - \nu_1$, meaning that the molecule is absorbing energy. Anti-Stokes lines arise when the molecule initially in the ν_0=1 state scatters radiation of frequency $\nu_0 + \nu_1$ and reverts to the ν_1=0 state, the molecule is emitting energy (Figure 2.3). Since the population of molecules is larger at ν=0 that at ν=1 (*Maxwell-Boltzmann distribution law*),

the Stokes lines are always stronger than the anti-Stokes lines. Thus, it is customary to measure Stokes lines in Raman spectroscopy. Consequently, the Raman spectra presented in this work correspond to Stokes lines.

In crystalline solids, the Raman effect deals with phonons, instead of molecular vibration. Similarly to the case of molecules, for every crystal symmetry class, it is possible to calculate which phonons are Raman active. A more detailed treatment of the principles of Raman spectroscopy in molecules and solids together with group theory can be found in Refs. [75, 76].

2.4 Simulations

In this section we shortly describe the principle of *ab initio* density functional theory (DFT) approximation adopted by the SIESTA code employed for this work. Moreover, we mention those particular features of the code used for the analysis of our results.

2.4.1 *Ab initio* DFT calculations

In physics and chemistry, a calculation is said to be *ab initio*, or from first principles, if it starts directly at the level of established laws of physics. Nevertheless, some approximations are needed to make achievable such calculations as discussed below.

This method provides the main tools for the understanding of the properties of matter, in all its possible states, by solving the fundamental equations for electrons.

In quantum mechanics a system is described by a wave function Ψ which is determined by the solution of the Schrödinger equation describing the nuclear and electronic motions:

$$\hat{H}(\mathbf{r},\mathbf{R})\Psi(\mathbf{r},\mathbf{R}) = (-\sum_{i=1}^{N_e}\frac{\hbar^2\nabla_i^2}{2m_e} - \sum_{I=1}^{N_i}\frac{\hbar^2\nabla_I^2}{2M_I} + \frac{1}{2}\sum_{I\neq I'}\frac{ZZ'e^2}{|\mathbf{R}_I-\mathbf{R}_{I'}|} + \tag{2.16}$$

$$+\frac{1}{2}\sum_{i\neq j}\frac{e^2}{|\mathbf{r}_i-\mathbf{r}_j|} - \sum_{i,I}\frac{Z_Ie^2}{|\mathbf{r}_i-\mathbf{R}_I|})\Psi(\mathbf{r},\mathbf{R}) = \tag{2.17}$$

$$= (\hat{T}_e+\hat{T}_i+\hat{V}_{i-i}+\hat{V}_{e-e}+\hat{V}_{i-e})\Psi(\mathbf{r},\mathbf{R}) = E\Psi(\mathbf{r},\mathbf{R}) \tag{2.18}$$

where $\mathbf{r}$ and $\mathbf{R}$ correspond to the positions of the N_e electrons and N_i ions, $\hat{T}_e$ and $\hat{T}_i$ are the electronic and nuclear kinetic energies and $\hat{V}_{i-i}$, $\hat{V}_{e-e}$ and $\hat{V}_{i-e}$ are the ion-ion, electron-electron and ion-electron coulombic interaction, respectively.

Due to the impossibility of solving exactly this equation when dealing with many body particles some approximations are needed. In the following we briefly describe the approximations adopted during this work.

- Adiabatic (or Born-Oppenheimer) approximation: as the general electronic velocities are much larger than the nuclear ones, hence, the nuclear and electronic motions can be decoupled and treated separately. In particular, the Schrödinger equation for the system can be decomposed as:

$$\Psi(\mathbf{r}, \mathbf{R}) = \psi_{\mathbf{R}}(\mathbf{r})\Phi(\mathbf{R}) \tag{2.19}$$

with the electronic wavefunction $\psi_{\mathbf{R}}(\mathbf{r})$ only parametrically depending on the nuclear position variable $\mathbf{R}$. Hence, each electronic structure calculation is performed for a fixed nuclear configuration.

- Density functional theory (DFT): within this approximation the electronic properties of a system of many interacting particles can be viewed as a functional of the ground state density $\rho(\mathbf{r})$. The modern formulation of density functional theory originated in a famous work written in 1964, where Hohenberg and Kohn provided the proofs for the existence of such a functional [77].

Kohn-Sham equations

Subsequently, Kohn and Sham [78], starting from the variational principle established by Hohenberg and Kohn, proposed to replace the original many-body problem by an "auxiliary" independent particle problem. The *ansatz* of Kohn and Sham assumes that the ground state density of the original interacting system is equal to that of some chosen non- interacting system. This leads to independent particle equations that are exactly solvable with the many-body terms incorporated into an exchange-correlation functional of the density. The Kohn-Sham (KS) equations for the auxiliary system of N non interacting electrons are:

$$\{-\frac{1}{2}\nabla^2 + v_{eff}(\mathbf{r})\}\psi_i = \varepsilon_i\psi_i \tag{2.20}$$

and

$$\rho(\mathbf{r}) = \sum_{i=1}^{N} |\psi_i(\mathbf{r})|^2 \tag{2.21}$$

where $\rho(\mathbf{r})$ is the density of the system, $v_{eff}(\mathbf{r})$ is an effective potential resulting from the external potential, the Hartree electronic interaction and the exchange and correlation potential $E_{xc}[\rho(\mathbf{r})]$ (which is discussed below); ε_i (multipliers of the KS equations) are related, in first approximation, to the energy levels occupied by the interacting electrons. The procedure to obtain the total energy of the system

is completely autoconsistent. The solution of equation 2.20 produces the wave functions ψ_i and then the electronic density from equation 2.21 which is used to define the effective potential in equation 2.20. This process is repeated until the tolerance imposed on the difference between the input and the output density is reached.

Exchange and correlation energy

The local density approximation (LDA) holds when $\rho(\mathbf{r})$ is a smooth function of $\mathbf{r}$. In this case, the exchange and correlation functional ($E_{xc}[\rho((\mathbf{r})]$) is approximated by an integral over space of the exchange and correlation energy which is assumed to be the same as in a homogeneous electron gas of $\rho(\mathbf{r})$ density. Its expression is:

$$E_{xc}[\rho(\mathbf{r})]^{LDA} = \int \rho(\mathbf{r})\epsilon_{xc}^{LDA}(\rho(\mathbf{r}))d\mathbf{r} \tag{2.22}$$

where $\epsilon_{xc}^{LDA}(\rho(\mathbf{r}))$ is the exchange and correlation energy of a homogeneous electron gas with density $\rho(\mathbf{r})$.

On the other hand, for very inhomogeneus systems the generalised-gradient approximation (GGA), which depends on the density and on its gradient is preferably used. In this work we have used the LDA approximation. The use of the GGA approximation was initially planned for a comparison but finally not performed.

- Pseudopotentials: the physical properties of solids are dependent on the valence electrons to a much greater degree than on the tightly bound core electrons. This approximation uses this fact to replace the complicated effects of the motion of the core electrons of an atom or ion and its nucleus with an effective potential, or pseudopotential. This fictitiuous potential acts in the internal region of the atoms, reproducing the screening effect of the core electrons within the core region. The "all-electron", i.e. the exact wavefunctions, are replaced by pseudo wavefunctions.

  The pseudopotential is then generated by fulfilling the following requirements:

  - the corresponding pseudo wavefunctions and the all-electron agree beyond a chosen core radius R_c;

  - pseudo and all-electron eigenvalues agree for a chosen atomic reference configurations meaning that the pseudopotential must describe the valence properties in a different environment including atoms, ions, molecules and condensed matter (*transferability*);

- the logarithmic derivatives of the pseudo and the all-electron wavefunctions agree at R_c;

- the integrated charge inside R_c for each wavefunction agrees meaning that the pseudo and the all-electron wavefunctions have the same norm (*norm-conserving pseudopotential*)

In particular, in this work we have used nonlocal [79], norm-conserving [80] fully separable Trouiller-Martins pseudopotentials. This means that they are built from a smooth and identical for all the angular momentum channels local part plus a non local part.

- Basis set expansion: in order to solve the 2.20 and 2.21 KS equations it is necessary to reduce the problem to a finite number of variables. This is done by expanding the unknown $\psi_i(\mathbf{r})$ wavefunctions in terms of known basis function. The most common basis function sets are plane waves and localized atomic orbitals.

2.4.2 The SIESTA code

The DFT code employed within this thesis work is SIESTA, a LCAO (*local combination of atomic orbitals*) method based on the use of numerical atomic orbitals (NAO) to expand the electron wavefunction. These orbitals are generated by solving, for each angular momentum, the radial Schrödinger equation of the isolated atom. They are given by the product of a spherical harmonic times a radial function. They are localised, i.e. defined to be zero beyond a specified radius. Hence, the expansion of the ψ_i electron wavefunction which satisfies the Bloch theorem is written as:

$$\psi_i(\mathbf{k},\mathbf{r}) = \frac{1}{\sqrt{N}} \sum_{\mu,\mathbf{R}} c_{i\mu}(\mathbf{k}) e^{i\mathbf{k}\cdot\mathbf{R}_\mu} \phi_\mu(\mathbf{r}) \tag{2.23}$$

where $c_{i\mu}(\mathbf{k})$ are the coefficients of the expansion of the wavefunction $i,\mathbf{k}$ in the basis set $\phi_\mu(\mathbf{r})$ centered at the atomic positions $\mathbf{R}_\mu$. The density matrix now takes the form:

$$\rho(\mathbf{r}) = \sum_{i\mathbf{k}} f_i(\mathbf{k}) \left|\psi_{i\mathbf{k}}(\mathbf{r})\right|^2 = \sum_{\mu\nu\mathbf{R}\mathbf{R}'} \phi^*_\mu(\mathbf{R}-\mathbf{R}_\mu)\phi_\nu(\mathbf{r}-\mathbf{R}_\nu)\rho_{\mu\nu}(\mathbf{R}-\mathbf{R}') \tag{2.24}$$

with

$$\rho_{\mu\nu}(\mathbf{R}-\mathbf{R}') = \frac{1}{N}\sum_{i\mathbf{k}} f_i(\mathbf{k}) c^*_{i\mu}(\mathbf{k}) \cdot c_{i\nu}(\mathbf{k}) e^{-i\mathbf{k}(\mathbf{R}_\mu - \mathbf{R}_\nu)} \tag{2.25}$$

where $f_i(\mathbf{k})$ is the Fermi-Dirac occupation factor.

Mulliken population analysis

An analysis tool that we have used in this work is the Mulliken population analysis method. This method allows the assignment of electronic contributions to individual atoms and bonds. However, due to the fundamental problem of deciding where atoms in solid or molecular systems actually start and where they end, there is no absolute way of partitioning the electronic density into atomic contributions. Nevertheless, this method is very useful for understanding the electronic structure of systems. Let's write the total number of electrons (electronic charge) N in the system as a sum of charges Q_μ (gross orbital population) associated to each of the orbitals in the basis[1]:

$$N = \sum_{i}^{occ} \langle \psi_i | \psi_i \rangle = \sum_{\mu} Q_\mu = \sum_{\mu} \sum_{\nu} P^{\mu\nu} S_{\nu\mu} \tag{2.26}$$

where $S_{\nu\mu}$ are the overlap matrix elements and $P^{\mu\nu}$ is the density matrix written in terms of the dual LCAO basis ($P^{\mu\nu} = \langle \phi^\mu | \hat{\rho} | \phi^\nu \rangle$). The gross orbital population Q_μ is the sum of two contributions: the *net orbital population* q_μ (expressed by the diagonal component in equation 2.26) and the *overlap orbital population* $O_{\mu\nu}$ which is the sum of the non-diagonal elements.

In this way, the total atomic charge for a given atom A is a matrix calculated as the sum of the orbital gross charges over all the orbitals belonging to that atom:

$$Q_A = \sum_{\mu \in A} Q_\mu \tag{2.27}$$

and Q_A is called Mulliken population of the atom A. By considering the overlap orbital population, the overlap charge between the atoms A and B is calculated as:

$$O_{AB} = \sum_{\mu \in A} \sum_{\nu \in B} O_{\mu\nu} \tag{2.28}$$

Projected density of states (PDOS)

The projected density of states (PDOS) is particularly helpful when trying to understand which is the contribution of the different atoms to the density of states. The density of states (DOS) is defined as:

$$DOS(E) = \sum_{i} \sum_{\mathbf{k}} \delta(E - \epsilon_i(\mathbf{k})) \approx \sum_{i} \sum_{\mathbf{k}} \frac{1}{\sigma\sqrt{\pi}} exp\left(-\frac{(\epsilon - \epsilon_i(\mathbf{k}))^2}{\sigma^2} \right) \tag{2.29}$$

[1] The dependence with $\mathbf{k}$ and $\mathbf{r}$ is now omitted for clarity.

where $\epsilon_i(\mathbf{k})$ is the energy of the one-electron states. The PDOS is then defined as follows:

$$PDOS = \sum_i \sum_{\mathbf{k}} \sum_{\mu} \delta(E - \epsilon_i(\mathbf{k}))c_{i\mu} \tag{2.30}$$

In this way PDOS represents the DOS projected on the ϕ_μ basis orbitals.

Vibrational spectra calculation

Raman vibrational spectra have also been calculated in this work. In the following we briefly describe the most general formulation for calculating the normal vibrational modes within the harmonic approximation.

If the displacements of the ions from their average positions are assumed to be small then the interaction potential can be expanded in a Taylor series so that, close to the equilibrium position, it is a quadratic function of the displacement. This is the harmonic approximation. The potential energy is :

$$U = U_0 + \sum_{\alpha m} \left[\frac{\partial U}{\partial \tau_{\alpha,m}}\right]_0 \tau_{\alpha,m} + \frac{1}{2} \sum_{\alpha m,\alpha' m'} \left[\frac{\partial^2 U}{\partial \tau_{\alpha,m} \partial \tau_{\alpha',m'}}\right]_0 \tau_{\alpha,m}\tau_{\alpha',m'} + \cdots \tag{2.31}$$

where $\tau_{\alpha,m}$ is the cartesian component ($m = x, y, z$) of the displacement of the α atom. The linear term of τ_α vanishes because at the equilibrium position forces are zero ($[\partial U/\partial \tau_{\alpha,m}]_0 = 0$). Hence, the hamiltonian of the system within the harmonic approximation becomes:

$$H = \frac{1}{2} \sum_{\alpha,m} M_\alpha \dot{\tau}^2_{\alpha,m} + U_0 + \frac{1}{2} \sum_{\alpha m,\alpha' m'} \frac{\partial^2 U}{\partial \tau_{\alpha,m} \partial \tau_{\alpha',m'}} \tau_{\alpha,m}\tau_{\alpha',m'} \tag{2.32}$$

and the classical equations of motion are:

$$M_\alpha \ddot{\tau}_{\alpha,m} = -\frac{\partial U}{\partial \tau_{\alpha,m}} = -\sum_{\alpha' m'} \left[\frac{\partial^2 U}{\partial \tau_{\alpha,m} \partial \tau_{\alpha',m'}}\right]_0 \tau_{\alpha',m'} \tag{2.33}$$

being M_α the mass of the α atom. We obtain the dynamical matrix using a finite differences approach, where the atoms were displaced by Δx=0.2Å. In particular, the second derivatives of the potential calculated with respect to the displacement at the equilibrium positions completely determine the lattice dynamics.

If the wavefunction in crystals has the form $\tau_\alpha = M_\alpha^{-1/2} \mathbf{u}_\alpha e^{i(\mathbf{q}\cdot\mathbf{R}_\alpha - \omega t)}$ equation 2.32 turns into an eigenvalues equation of $3N_\alpha$x$3N_\alpha$:

$$\omega^2 \mathbf{u}_\alpha = \mathbf{D}(\mathbf{q})\mathbf{u}_\alpha \tag{2.34}$$

where $\mathbf{D}(\mathbf{q})$ is the *dynamical matrix* and is defined as:

$$\mathbf{D}(\mathbf{q}) = D^{mm'}_{\alpha\alpha'}(\mathbf{q}) = (M_\alpha M_{\alpha'})^{-1/2} \sum_{\mathbf{R}_\alpha - \mathbf{R}_{\alpha'}} \frac{\partial^2 E}{\partial \tau_{\alpha,m} \partial \tau_{\alpha',m'}} e^{-i\mathbf{q}\cdot(\mathbf{R}_\alpha - \mathbf{R}_{\alpha'})} \tag{2.35}$$

where $\mathbf{R}_\alpha$ is $\mathbf{R}_\alpha = \mathbf{R}^0_\alpha + \tau_\alpha$. The eigenvalues and eigenvectors are the frequencies and the vibrational modes of the system.

The dynamical matrix can be calculated by considering a perturbative potential which allows to analytically obtain the second derivative of the energy or simply by considering the total energy of the system without having information about its analytical second derivatives. In this thesis we employed the second method.

Chapter 3

Experimental set-up

This chapter is devoted to the description of the experimental set-up employed during our measurements. We first give a brief overview of the technical devices used for achieving high temperature and high pressure conditions and then, we describe the experimental apparata where these devices have been installed and used in order to collect x-ray absorption, x-ray diffraction and Raman spectroscopy data.

3.1 High pressure experimental methods

The high pressure devices used in this thesis are the Paris-Edinburgh cells and the diamond anvil cells. The first apparatus allows to achieve a maximum pressure of 17 GPa on samples of ≈1-3 mm^3 while the second one can generate much higher pressure, up to around 500 GPa, on much smaller samples (few μm^3). The choice of the device depends on both the thermodynamic conditions (pressure and temperature) needed for the experiment and on the experimental apparatus available for the different techniques. In the following section more details about the Paris-Edinburgh cell and the diamond anvils cells are given.

3.1.1 Large volume Paris-Edinburgh press

The Paris-Edinburgh (PE) cell is one of the classical instruments to perform high pressure (HP) and high temperature (HT) *in situ* x-ray measurements on large crystalline, liquid or amorphous samples.

The PE was originally developed for neutron diffraction experiments on large volume samples [81] and then adapted to x-ray diffraction and absorption experiments [82]. Using this device it is possible to perform HP and HT measurements in different P-T ranges depending on the anvils type used within this press. In particular, we can reach pressures

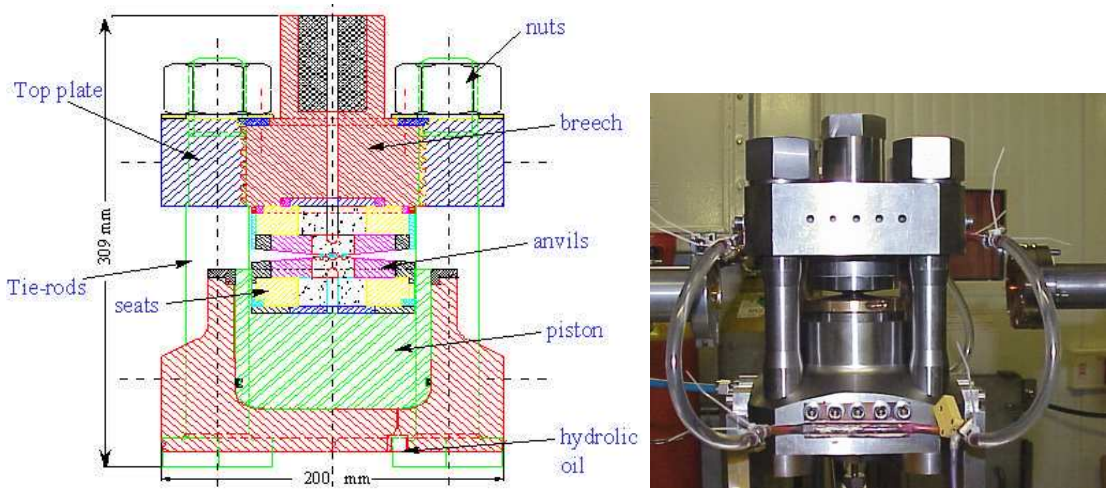

Figure 3.1: *Schematic drawing (left panel) and picture (right panel) of the Paris-Edinburgh large volume cell for x-ray measurements.*

of 9 GPa and, at the same time, temperatures of 1500 K or 17 GPa and 1200 K by using tungsten carbide (WC) or sintered diamond (SD) anvils, respectively. A detailed discussion about technical improvements allowed by these new SD anvils, coupled with a new cell assembly system, can be found in Ref. [83].

Because of the large dimension of the sample (volume ≈1-3 mm^3) compared to diamond anvil cells, the PE cell belongs to the large volume HP apparata "family". A schematic drawing of the large volume press is reported in Figure 3.1. The thrust on the seats of the anvils is generated by a piston-cylinder assembly pressurized by a suitable high pressure oil circuit. The idea is that two opposed anvils will concentrate the force onto a small area, of about 1/100 of the piston surface, hence providing a magnification of the pressure by a factor 100. For x-ray applications, the press is operated with special WC or SD truncated cone type anvils designed to obtain hydrostatic pressure conditions and to access with x-rays inside the HP cavity.

A sintered amorphous boron-epoxy gasket placed in the middle of the anvils transmits the pressure to the sample. Boron gaskets have low thermal conductivity and high mechanical strength to support high-pressure at high-temperatures. The gasket absorbance fixes low energy operation limit of this technique to about 10 keV. The gasket can have an external diameter of 5, 7 or 10 mm with an internal diameter of 1.5, 2 and 3.5 mm, respectively. Obviously, the bigger the gasket size the lower the maximum attained pressure. In this study, we always used 5 mm gaskets. An example of cell assembly is shown in Figure 3.2. The size of the different components of the HP and HT environment cell depends on the dimension of the gasket used.

In order to better achieve an isotropic pressure distribution, the sample must be embedded and confined in a pressure transmitting medium (PTM) consisting in an inert matrix softer than the sample.

For HT experiments, when sample reaction or contamination with the matrix is possible, the compound is directly inserted into an insulating capsule without any PTM. In any case, the assembly is placed inside a high resistivity graphite cylindrical furnace or rhenium strips furnace which acts as an heater.

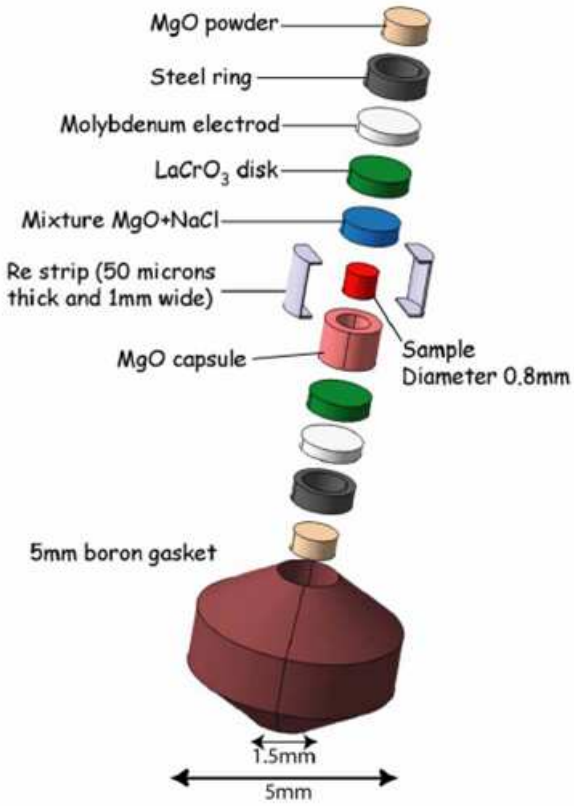

Figure 3.2: *Typical cell assembly used for in situ x-ray measurements.*

The heating power is generated by an electrical current through the graphite crucible, anvils and electrical contacts (Mo disks and steel rings). For higher gasket sizes, i.e. 7 and 10 mm diameter, the temperature can be measured by an insulated K-type thermocouple placed in the sample gasket. An additional estimate of the temperature ramp can, however, be obtained, by the power delivered to the sample (calculated as the product of the current by the voltage across the anvils), through previously calibrated power curves in P-T space.

The pressure is usually measured by *in situ* x-ray diffraction following the lattice contraction of internal pressure markers, added to the sample, whose equations of state are reasonably well known. In this work we employed different pressure marker systems de-

pending on the P-T range. In particular we used LiF, NaCl, MgO [84, 85] and h-BN [86]. The Vinet-type [84] equation of state used in this work is written as:

$$P = 3B_0 x^{-2}(1-x)\exp[\eta(1-x)] + \alpha_0 B_0 (T - T_R) \tag{3.1}$$

where $x = (V/V_0)^{1/3}$, B_0 is the equilibrium volume V_0 isothermal bulk modulus ($B_0 = (-V\,dP/dV)$) and η=(3/2)($\partial B_0/\partial P - 1$). The knowledge of zero-pressure properties, V_0, B_0 and the thermal expansion coefficient α_0, at the reference temperature T_R (room temperature) is required.

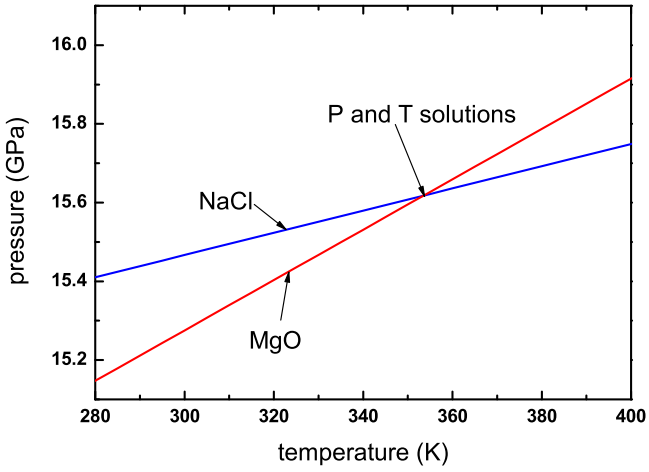

Figure 3.3: *Example of MgO and NaCl $P(T)$ cross-calibration curves. The intersection point gives the values of P and T: 15.6 GPa and 353 K.*

For HT measurements, both pressure and temperature can be cross-calibrated from the equations of state of two P-T markers [87], possibly having contrasting dependence on their thermoelastic properties (bulk modulus and thermal expansion) (i.e. MgO and NaCl, Re and NaCl). As two thermodynamic variables are unknown (P and T), two equations of state are required in order to obtain their values. HT and HP measurements performed in this thesis work have been calibrated by using this technique. In Figure 3.3 we report an example of a cross-calibration graph used to calibrate P and T.

In particular, this method is valuable in situations where the use of a thermocouple is not possible or advisable, for instance in 5 mm diameter gaskets or, for example, above 1200 K, i. e. near the melting points of the thermocouple materials.

When dealing with extremely air sensitive systems, such as in our case, the good sealing of the sample is a critical parameter that must be taken into consideration during

experiments. In particular, good airtightness conditions must be provided to the sample during the transport from the inert atmosphere glove box to the PE cell installed at the beamline. For this purpose a clamp system, shown in Figure 3.4, has been used during the present study. This system allows to hermetically enclose the sample in a glove box, within its high pressure cell assembly, between the two anvils in order to avoid air and/or humidity sample contamination before starting the high pressure experiment. Moreover, the clamps provide a water circulation system for the anvils cooling during high temperature measurements.

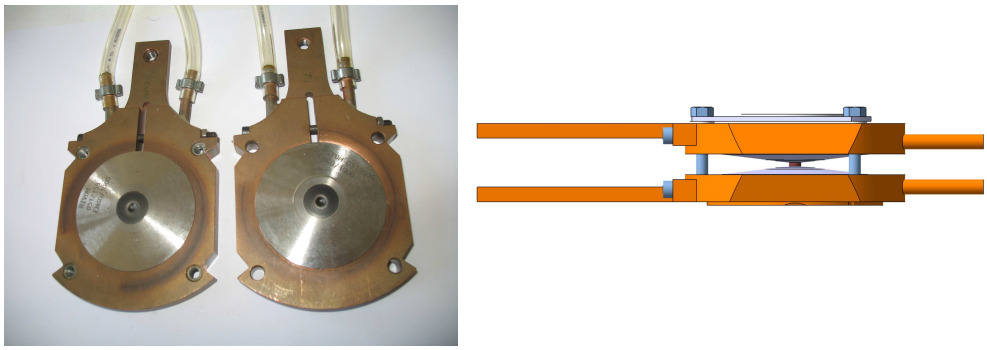

Figure 3.4: *Picture (left panel) and schematic drawing (right panel) of the anvils within the clamp system used both for preventing the sample reaction with air and humidity and for cooling the anvils.*

3.1.2 Diamond anvil cells

The diamond anvil cell (DAC) is the pressure device which allows to reach the highest static pressures.

The great number of results in the field of HP research is strictly related to the development of the DAC technique; see for example [88] for a review of early developments. This device, that can fit into the palm of the hand, can generate pressures up to about 500 GPa (5 millions times the atmospheric pressure) [89]. The DAC is very simple in principle. It consists of two gem-quality single crystal diamonds with flat surfaces to serve as anvil faces (Figure 3.5).

The diamonds are mounted so that a sample can be squeezed between the anvil faces shown in Figure 3.5. The smaller the area A of the anvil faces, the higher the pressure P reached by the DAC for an equivalent value of applied force F, according to the relationship $P = \frac{F}{A}$. Figure 3.6 shows the principle of DACs. In order to apply pressure to the sample, the anvil faces must have a high degree of parallelism. One of the diamond anvils is usually

mounted on the end of a sliding piston, while the other is stationary. A cylinder guides the piston so that the anvil faces meet very precisely. The piston is pushed by a mechanical device such as a screw or a small hydraulic ram, driving the two anvils together.

A rocker or a tilting plate directly under the diamond anvils allows orientation of the diamonds to be adjusted so that the faces are concentric and parallel.

A membrane DAC has been used for the experiments presented in this work. In particular, we employed a Chervin-type DAC and a picture of this cell is shown in Figure 3.7 [90]. In this type of cell the pressure on the sliding piston results from the deformation of a thin membrane by effect of a He pressure [91]. This allows a homogeneous distribution of the force applied on the membrane and a fine pressure control. This type of cell allows changing of pressure in small steps enabling, for example, careful observation of sample behaviour at a phase transition. Moreover, the possibility to change the pressure on-line without the need of moving the cell makes the Chervin-type DAC particularly suited for experiments using synchrotron radiation where the alignment of the sample is a delicate and sometimes long procedure.

For HT measurements, two heating techniques in the DACs nowadays exist to achieve simultaneous HP and HT conditions: resistive heating and laser heating. For the resistive heating two methods are possible: internal and external heating. In this work, HP and HT conditions have been achieved via external resistive heating. In this case the DAC is placed as a whole in a furnace, which can be typically a resistive heated metallic cylinder as the one shown in Figure 3.7. This method yields a very uniform temperature field and allows to reach temperatures up to 600 K. For higher temperatures, the whole system must be enclosed in a vacuum chamber to avoid graphitization of the diamonds.

When the sample is placed between the anvil faces, in contact with them, as the anvils are forced together, the sample is trapped and subject to an uniaxial pressure, whose distribution ranges from a maximum at the center to a much lower pressure at the edge of

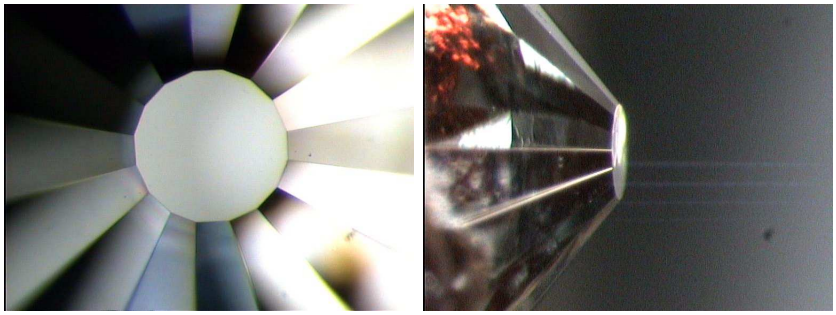

Figure 3.5: *Diamond anvil face from top and from side.*

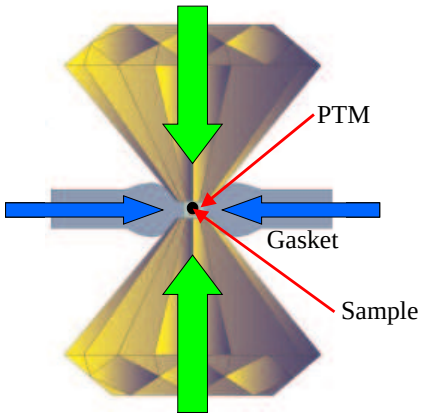

Figure 3.6: *The principle of the diamond anvil cell. The use of a PTM and of a gasket to encapsulate sample and PTM allows to overcome the uniaxial pressure generated by the diamonds and to have an isotropic pressure.*

Figure 3.7: *Chervin-type DAC (left panel) and external heater for Chervin-type cell (right panel).*

the sample area [92, 93]. In order to have an isotropic pressure distribution the sample must be embedded and confined in a PTM softer than the sample. A complete description of different PTM is given in [94]. In our experiments we have used different PTM depending on the type of measurements, on their reactivity with the systems and finally on the possibility of having the intercalation of the PTM into fullerene-based systems. In this thesis work, we used:

- **Silicon oil**: for some measurements performed at room temperature as this PTM has been observed to react at HT with our samples.

- **LiF** and **NaCl**: these salts were used for XRD and XAS measurements both at high and at room temperature. NaCl was used for all the Raman measurements.

Both the sample and the hydrostatic medium (PTM) are placed in a small hole drilled in a metallic gasket. (Figure 3.6). The gasket consists of a metallic foil of typically 200 μm of thickness. To increase the hardness of the metal, the foil is placed between the two diamonds and is pre-indented to about 30-60 μm. The diameter of the hole depends critically on the diameter of the diamonds, and it is typically one third the diameter of the flat of the diamond.

A second purpose of the gasket is to provide support at the edges and sides of the anvils thus preventing failure of the anvils at very HPs. In this work stainless steel and rhenium have been used as gasket materials for RT and HT measurements respectively.

Methods for measuring pressure

Several methods for measuring pressure have been developed. If the experimental technique is *in situ* XRD, then the diffraction pattern of an internal standard can be used as a pressure marker as discussed in the previous section.

Another means of measuring the pressure is the ruby fluorescence method which was used in the present work.

This method is particularly well adapted to DAC technology since it exploits the high transparency of diamonds to visible light. Forman *et al.* in 1972 [95] first showed that the luminescence doublet of peaks R_1 and R_2 of Cr^{3+}-doped Al_2O_3 (ruby) shift linearly with hydrostatic pressure in the range of 1–22 GPa, and that the two lines broaden if the ruby experiences nonhydrostatic stresses.

In this method [96] a tiny chip of ruby (5-10 μm in dimensions) is placed in the pressure medium along with the sample (Figure 3.8), and its luminescence is excited by a laser.

The shift in wavelength is followed as a function of pressure. An important question with regard to the ruby scale is how far it is linear [97, 98, 99]. According to [100], the relationship between the pressure P (in GPa) and the ruby R_1 line wavelength shift λ (in nm) can be described by the following relationship (at 20 °C),

$$P = \frac{1904}{B}\left(\left(\frac{\lambda}{\lambda_0}\right)^B - 1\right). \tag{3.2}$$

where the parameter B is equal to 7.665 and 5 for quasi-hydrostatic and non-hydrostatic conditions respectively. λ_0 correponds to the wavelength measured for a standard ruby chip at room temperature and ambient pressure and is equal to 694.24 nm.

It is important to clarify that the position of the ruby luminescence lines varies with temperature, with a slope of 0.068 Å K^{-1}, which means that a ΔT of $\sim$ 5 K produces the

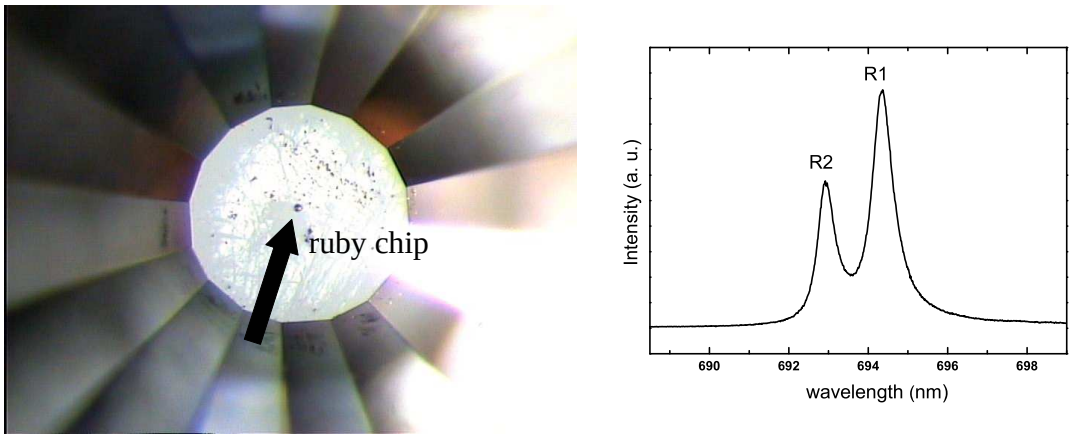

Figure 3.8: *Ruby on a face of a diamond anvil (left panel) and fluorescence spectrum of the ruby at 0.3 GPa and room temperature (right panel). The fluorescence doublet shifts towards higher wavelengths under pressure.*

same shift as the application of a pressure of 0.1 GPa. Therefore a variation of temperature from the standard 20 °C has to be taken into account for a precise determination of pressure. Temperature correction of the ruby pressure scale was systematically studied by Vos and Schouten [101].

The ruby gauge has some disadvantages: the luminescence spectrum exhibits a doublet instead of a single line that is desirable for exact pressure determination; rubies provide low accuracy in the low pressure region ($\sim$ 1 GPa) and their luminescence becomes weak at megabar pressures. These limits have motivated a search for other fluorescent compounds which would be more adequate for both very HP and HT studies in the DACs like SrB_4O_7:Sm^{2+}.

3.2 Experimental apparata

X-ray absorption and x-ray diffraction experiments performed in the framework of this thesis have been carried out at the European Synchrotron Radiation Facility (ESRF) in Grenoble. In this section, we do not describe the details of synchrotron radiation which are treated extensively in specific textbooks (e.g. in [102]). We concentrate instead on the experimental set-up for performing measurements under high pressure and/or high temperature conditions developed at the BM29, ID24 and ID27 beamlines. In particular, x-ray absorption experiments have been performed at the BM29 and ID24 beamlines by using the Paris-Edinburgh cell and the diamond anvil cell respectively, while x-ray diffraction experiments have been perfomed at the ID27 beamline with both devices.

Finally, we briefly describe the apparatus used to collect Raman spectroscopy spectra at the ENS-Lyon (Univ. Lyon 1).

3.2.1 Beamline BM29 - ESRF

X-ray absorption measurements have been performed in transmission geometry at the BM29 beamline.

BM29 is the general purpose x-ray absorption spectroscopy beamline [103] of the ESRF, built tangentially to a bending magnet of this 3rd generation synchrotron radiation source.

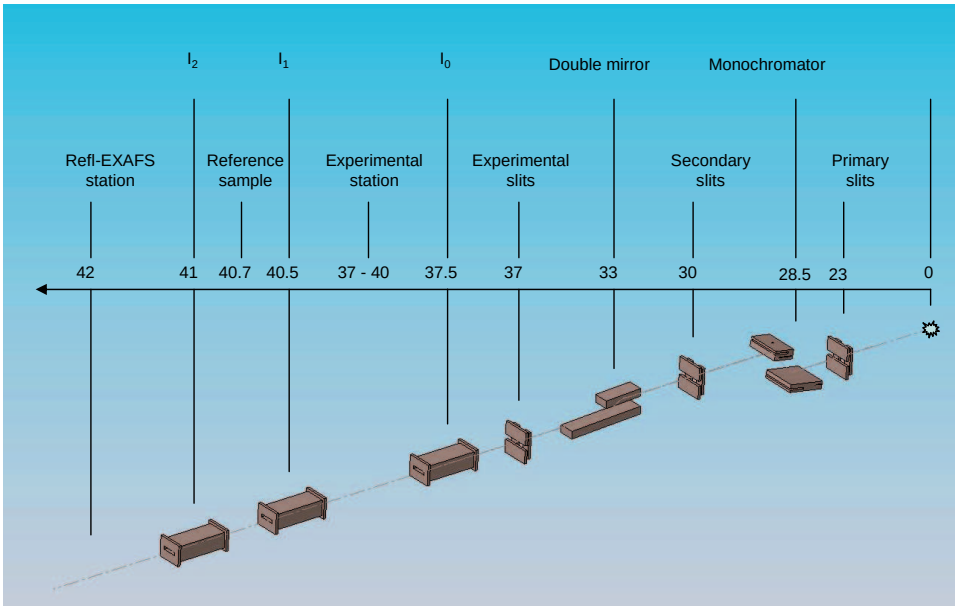

Figure 3.9: *Pictorial representation of the experimental setup for combined XAS and XRD experiments installed at the beamline BM29-ESRF.*

The beamline optics includes a double flat crystal monochromator and a pair of harmonic rejection mirrors. The lower mirror can be used as well for focusing the beam down to 20-30 μm.

A simple scheme of BM29 is shown in Figure 3.9. XRD patterns can be collected by means of a MAR345 image plate detector mounted off-axis with respect to the beam in analogy to the setup described in Ref. [104]. The image plate position and the selected energy for XRD measurements are chosen in order to optimize the detection of the most intense Debye-Scherrer rings of the pressure markers.

Four different Si crystal pairs can be installed, depending upon the requirements for energy and photons flux. For the experiments related to this work, Si(311) crystals having operational energy between 5 and 50 KeV, have been used. The energy resolution when using a Si(311) monochromator is $\Delta E/E$=4 $\times$ 10^{-5} at 15 KeV. This is well below the natural broadening of the spectra given by the core hole widths ($\approx 2 \times 10^{-4}$).

Beam intensity is measured by sealed ionization chambers filled with optimal He/Ar or He/Kr mixtures at a total pressure of 2 bars and normally operated at a field of about 300-800 V cm^{-1}. The gas noble species, gas pressure and applied voltage control the detector efficiency.

3.2.2 Beamline ID24 - ESRF

We have collected x-ray absorption spectra under high pressure (up to 45 GPa) at the ID24 beamline in transmission geometry.

This beamline satisfies the main requirements for performing HP XAS studies:

- small focal spot: for a 300 μm diamond-anvil flat (required for P of the order of 50 GPa) and gasket hole diameter of 100 μm, the sample size is around 80 μm;
- position stability of focal spot in whole energy range;
- high flux: for measurements in transmission geometry the x-ray beam traverses the two diamonds. The thickness of a single diamond is between 2 and 2.5 mm. This poses real problems for low energy XAS (E<8 keV).

ID24 is the ESRF XAS beamline with parallel detection of the whole spectrum made possible by energy dispersive highly focusing x-ray optics [105, 106].

The geometrical arrangement of the energy dispersive optics is given in Figure 3.10.

A quasi-parallel and polychromatic beam, supplied by a an undulator source, is energy-dispersed and focused by an elliptically curved crystal. Because the incident x-rays strike the crystal at slightly different angles along its length, the bent crystal acts as a polychromator diffracting a different energy at each point. This energy-dispersed beam converges to a focus at the sample position. The beam, transmitted through the sample position, then diverges towards a PSD. The position of the beam, incident in the detector, can be directly correlated to energy. By measuring the spatial X-ray intensity distribution in the presence (I_1) and absence (I_0) of the sample, a transmition geometry x-ray absorption spectrum can consequently be obtained. Figure 3.10 shows the present optical scheme.

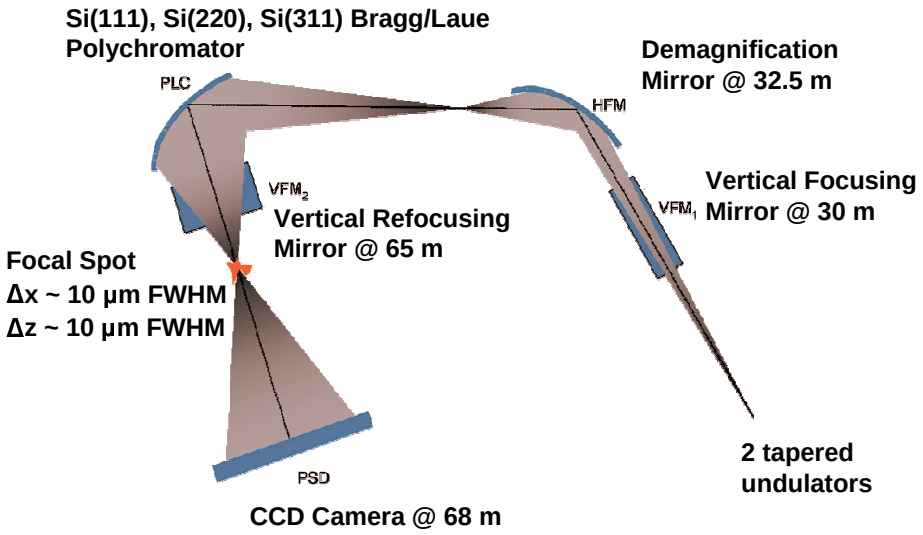

Figure 3.10: *Present optical layout of beamline ID24. The polychromator is coupled to two undulators through a Kirkpatrick-Baez optical system. The third refocusing mirror was added to the original configuration in 2000.*

The two Kirkpatrick-Baez mirrors reflect the beam at a fixed grazing angle of 3 mrad and ensure efficient harmonic rejection in the whole energy range of operation, between 5 and 27 keV. The first mirror, placed at 30 m from the source, is in a quasi 1:1 configuration and vertically focuses the beam on the detector through a pneumatic bender mechanism. For experiments requiring a small focal spot, such as HP experiments using DACs, a third mirror to refocus the beam in the vertical direction at the sample position is added to the optical configuration. The horizontal divergence necessary to obtain the requested energy bandwidth (ΔE) after diffraction from the polychromator is produced by the second mirror. Placed at 32.5 m from the source, this strongly focusing mirror creates a horizontally-demagnified image of the source that becomes the effective source for the polychromator crystal. The polychromator consists in a curved Si crystal in a Bragg [107] or Laue [108] geometry. Si(111) and Si(311) crystals are used to match the energy resolution/energy bandwidth requirements for the specific applications.

The ΔE necessary for acquiring all data points in parallel is directly proportional to the footprint of the beam on the polychromator crystal and to the cotangent of the Bragg angle [109]. The latter factor severely limits ΔE at low energies. Typical values for ΔE/E range between 5% to 15% at low and high energies respectively.

The spectrometer consists of a Θ - 2Θ goniometer with the monochromator on the Θ axis and an optical bench oriented at 2Θ with the sample and the position sensitive detector on it. Typical focal spot dimensions for HP measurements are at the order of

10x10 μm FWHM (full width at half maximum).

3.2.3 Beamline ID27 - ESRF

X-ray powder diffraction has been performed at the ID27 beamline (ESRF) optimized for the study of materials under extreme conditions [110]. It is composed of an optical hutch, two specialized experimentals hutches, two control-cabins and two high pressure laboratories. The first experimental hutch, EH1, is fully dedicated to large volume cell experiments using a Paris-Edinburgh (PE) cell while the second hutch, EH2, is fully optimized for diamond anvil cell (DAC) experiments. The centres of the experimental hutches EH1 and EH2 are respectively located at 41 and 48 m from x-ray source. The x-ray source is composed of two small-gap in-vacuum undulators of period 23 mm that can be used simultaneously at a minimum magnetic gap of 6 mm. The monochromatic beam is selected using a nitrogen-cooled Si(111) monochromator and focused on the sample using multilayer mirrors in the Kirkpatrick-Baez (KB) geometry. The multilayer mirrors are 300 mm-long and are made of iridium-allumina multilayers deposited on silicon wafers. These mirrors possess a very broad energy band pass from 6 keV to 80 keV with a maximum of 80% reflectivity at 30 keV. Large focal distances of 800 and 1200 mm are used for the horizontal and the vertical mirrors, respectively, in order to avoid serious loss of spatial resolution. When using the KB focusing mirrors the obtained focal spot diameter is 7 μm at around 33 keV.

The PE cell diffractometer set-up includes a Soller slits system in order to eliminate most of the background signal coming from the sample environment (i. e. furnace, B-epoxy gasket, etc.) and a large area detector-Bruker CCD or MAR345 image plate easly interchanged using motorized translations. The sample to detector distance and the image plate tilt angles were precisly calibrated using a standard located at the sample position. For DAC experiments a two-circle goniometer is installed in the EH2 hutch.The criteria for the choice of the optimal detector for high pressure experiments are mostly dictated by the cell goniometer (limited 2θ angle), composition (diamonds for the DACs, a-B gasket for the PE press) and by working x-ray energies.

3.2.4 Raman spectrometer - ENS-Lyon (Univ. Lyon 1)

The Raman measurements were recorded on a Jobin-Yvon HR-800 Labram spectrometer with double-notch filtering and air cooled CCD detector at the Ecole Normale Superieure (ENS, Lyon). The spectrometer was used in backscattering geometry as shown in Fig. 3.11. The laser beam (514.5 nm exciting lines of an Ar^+ laser) is focused down to a 2 μm spot

on the sample and the backscattered light is collected through the same objective. In our experiments high resolution spectra (~ 0.5 cm^{-1}) have been collected at room temperature as a function of pressure. During high pressure experiments, due to the unavoidable backward scattering through the diamond of the high pressure cell, we didn't collect data in the frequency shift region around 1332 cm^{-1} because it was masked by the very strong diamond peak. For our measurements the optimum laser power was found to be 5 mW, measured directly before the high pressure cell in order to avoid laser-induced heating of the sample. A picture of the set-up used for collecting Raman scattering data is shown in Fig. 3.11.

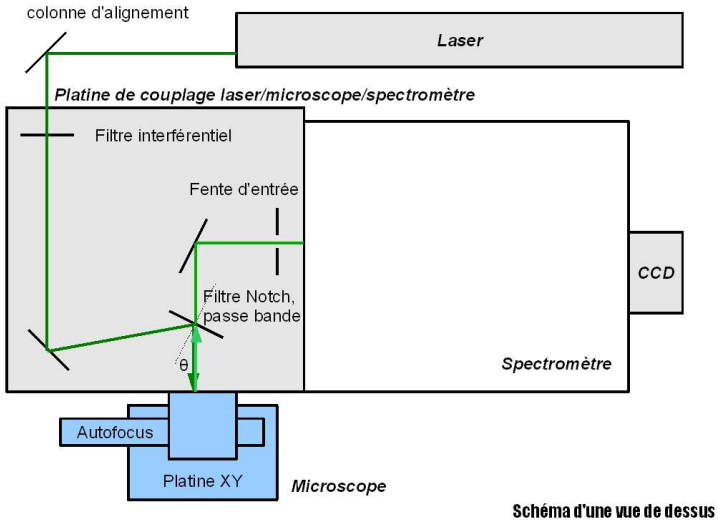

Figure 3.11: *Scheme of the geometry used in our Raman experiments.*

Chapter 4

Pressure induced distortion of the C_{60} molecule in Rb_6C_{60} and Cs_6C_{60}

In this chapter, we report a detailed experimental and theoretical study of the Rb_6C_{60} and Cs_6C_{60} systems under pressure. X-ray diffraction and x-ray absorption experiments have been performed up to around 15 GPa at room temperature. We have coupled the experimental results with *ab initio* calculations in order to understand the mechanisms taking place during the compression of these intercalated systems. The results presented in this chapter are consistent with a pressure induced modification of the shape of the C_{60} molecule. This deformation constitutes an enhancement of the calculated distortion of the molecule in these intercalated compounds at ambient conditions [69] discussed in section 1.4.

4.1 Introduction

In chapter 1 we mentioned that the C_{60} fullerene and its compounds have attracted much attention due to some of their extraordinary properties, related to the high symmetry and simplicity of the molecule. Among these, the compressibility of a single buckminsterfullerene molecule is calculated to have values between 700 and 900 GPa [43, 44], exceeding significantly that of diamond (around 440 GPa). Subsequently, most studies of the high pressure behavior of fullerene-based crystals have considered the molecule as not deformable up to the formation of intermolecular bonds. In fact, under high pressure and high temperature conditions, crystals of pristine C_{60}'s follow a series of phase transformations including the formation of 1D, 2D or 3D polymers as explained in chapter 1 [53, 111, 28, 18, 20, 48, 57]. Polymerization can lead to the deformation of the molecule

[5, 57], nevertheless, a possible deformation of the non-covalently bonded C_{60} molecules under compression has not been detected yet. On the other side, the ionic interaction due to alkali intercalation has been predicted to give rise to a distortion of the C_{60} [69] compared to the isolated molecule. No experimental evidence of such deformation has been provided up to now. The application of pressure constitutes a possible means to enhance such distortion and its exploration is the object of this chapter. In addition, recent studies [71] have shown that for high Rb content, i.e. in Rb_6C_{60}, there is no phase transformation up to 22 GPa and this makes of such system a very favorable case for the study of the evolution of the C_{60} molecule up to high pressures. Consequently, Rb_6C_{60} and Cs_6C_{60} constitute good candidate systems for the study of the pressure evolution of the geometry of the C_{60} molecule.

4.2 Experimental details

The method employed for the synthesis of the Rb_6C_{60} and Cs_6C_{60} compounds is reported in appendix A. The quality of the obtained sample was verified by XRD and it is reported in the next section for the Cs_6C_{60} system and in appendix A (Figure 8.13, panel (c)), for the Rb_6C_{60}.

High pressure experiments were performed at the European Synchrotron Radiation Facility (ESRF, Grenoble, France) using a "Paris-Edinburgh" (PE) pressure device [81] with 5 mm sintered diamond anvils [83].

Angular dispersive XRD experiments were performed at the high-pressure insertion device ID27 beamline [110] by angle-resolved measurements. The monochromatic beam with wavelength λ=0.3738 Å was focused on the sample using mirrors in the Kirkpatrick-Baez geometry. The diffraction patterns were recorded on a large area scanning MAR345 image plate and were analyzed using the FIT2D [112] software package. XAS measurements were performed at the bending magnet BM29 beamline [103] in transmission geometry. For pressure calibration, XRD patterns were collected by means of a MAR345 image plate detector mounted off-axis with respect to the beam in analogy to the setup described in Ref. [104]. The image plate position and the selected energy for XRD measurements have been chosen for each experimental run (Cs_6C_{60} and Rb_6C_{60}) in order to optimize the detection of the most intense Debye-Scherrer rings of the pressure markers.

In both XRD and XAS experiments samples were inserted in CuBe alloy (2% wt of Be) capsules, which were themselves embedded in a MgO cylinder and inserted in graphite (for Cs_6C_{60}) or rhenium [83] (for Rb_6C_{60}) resistive furnaces for the high pressure-high

temperature measurements. The whole setup was prepared in an argon atmosphere glove-box in order to avoid sample deterioration. For each system the final sample environment was introduced in a 5 mm (external diameter) boron-epoxy gasket that was loaded between the anvils and pre-compressed in the glove-box before insertion in the Paris-Edinburgh cell. The diameter of the CuBe capsule containing the sample was equal to 1.5 mm (internal hole diameter of the gasket). Pressure calibration was done using the Vinet equations of state of NaCl and MgO [84, 85].

NaCl powder pellets were introduced on top and at the bottom of the CuBe capsule. In the particular case of XAS ambient temperature measurements on Rb_6C_{60} the experimental setup for the high pressure cell was different. In this case we mixed small quantities of sample with the pressure marker (hBN) in the proportion Rb_6C_{60}:BN=1:13 (in wt) and inserted the mixture directly into the gasket without using the CuBe crucible. In this case only the hBN compound was used as pressure marker and the Birch-Murnaghan equation of state [86] was used to calibrate the pressure on the sample. The reason why we used a different sample environment for these measurements is because no high temperature conditions were planned for the study of this sample.

The high temperature part of the experiments will be reported elsewhere. As Cs_6C_{60} and Rb_6C_{60} are extremely sensitive to oxygen and humidity, the pressure transmitting medium was previously oven-dried and degassed in order to prevent contamination of the sample.

4.3 XRD measurements

The data quality is illustrated by the Le Bail fitting of the Cs_6C_{60} sample at ambient pressure and room temperature inside the high pressure environment cell presented in Figure 4.1. The obtained fit allows to guarantee the absence of sample contamination within our experimental protocol.

At room temperature and ambient pressure the values of lattice parameter of Cs_6C_{60} (a=11.790(1) Å) and Rb_6C_{60} (a=11.540(2) Å) obtained from our XRD analysis are in agreement with those reported in literature [113, 71].

The pressure evolution of the XRD patterns from ambient pressure up to 14.8 GPa and 16.5 GPa respectively for Cs_6C_{60} and Rb_6C_{60} is shown in Figure 4.2. No sign of phase transformation is observed up to the highest measured pressure.

Data were analyzed using the FULLPROF package [114] in the Le Bail configuration: unit-cell parameters and profile shape parameters were fitted independently. The lattice

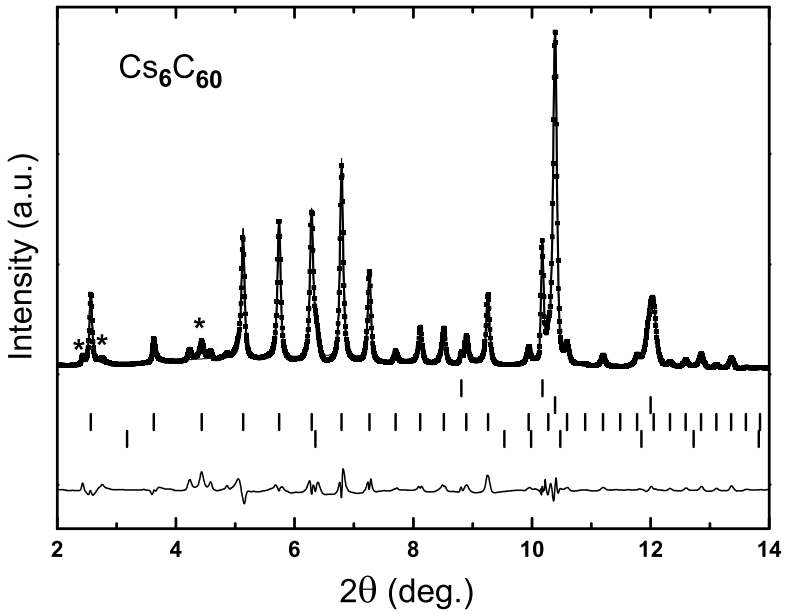

Figure 4.1: *Le Bail fit of the Cs_6C_{60} XRD pattern obtained in the high pressure setup described in the text at room temperature and ambient pressure (R_{wp}=18.0% and χ^2=3.9). The ticks correspond from top to bottom to MgO, CuBe alloy, Cs_6C_{60} and graphite. The star labels point to peaks due to the B-epoxy gasket. The lower line corresponds to the residual pattern.*

parameter of Rb_6C_{60} and Cs_6C_{60} for the different values of pressure obtained from the Le Bail fit of x-ray diffraction data are reported in Table 4.1.

Figure 4.3 shows the relative volume variation as a function of pressure obtained from the lattice parameters. The experimental value of the bulk modulus, B_0, and its pressure derivative, $B_0^{'}$, were obtained by fitting the experimental volume vs pressure (V vs P) points with the Murnaghan equation [115] of state whose expression is:

$$P = \frac{B_0}{B_0^{'}}\left[\left(\frac{1}{x}\right)^{3B_0^{'}} - 1\right] \tag{4.1}$$

where V_0 is the equilibrium volume at room temperature, $x = (V/V_0)^{1/3}$, B_0 is isothermal bulk modulus ($B_0 = (-V\,dP/dV)$) calculated at the V_0 and $B_0^{'}$ is $\partial B_0/\partial P$.

The obtained values are shown in Table 4.3. We obtain bulk modulus values of 30 ($/pm3$) and 33 ($/pm3$) GPa for Rb_6C_{60} and Cs_6C_{60}, respectively and they coincide within the experimental error (Table 4.3). This can be appreciated also in Figure 4.3 where no

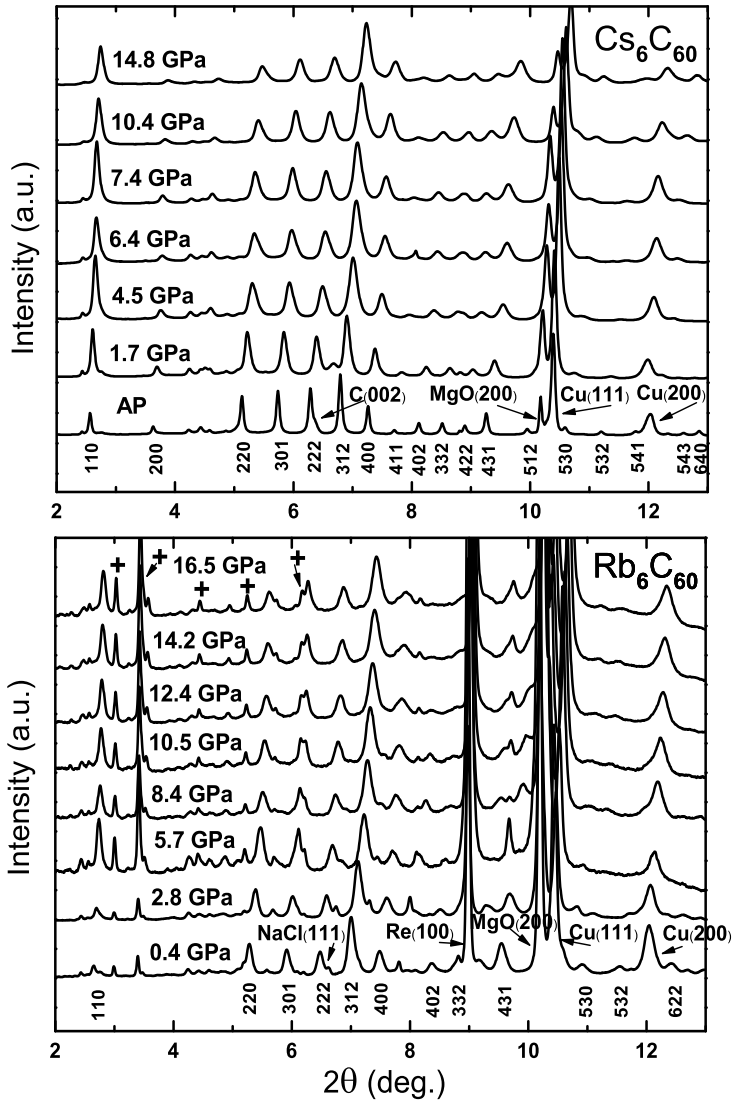

Figure 4.2: *Pressure evolution of the XRD pattern of Cs_6C_{60} (upper panel) and Rb_6C_{60} (lower panel) from ambient pressure (AP) up to 14.8 GPa and from 0.4 up to 16.5 GPa, respectively. Data have been normalized to the intensity of the (312) Bragg reflection. Labels denote the main Bragg peaks as well as reflections originating from the sample environment. 'Cu' stands for the CuBe alloy capsule. In the lower panel some new Bragg reflections appearing at 5.7 GPa arise from the boron-epoxy gasket. They are indicated with the '+' symbol.*

straightforward conclusion about the relative compressibility of the two systems can be established due to the experimental uncertainties.

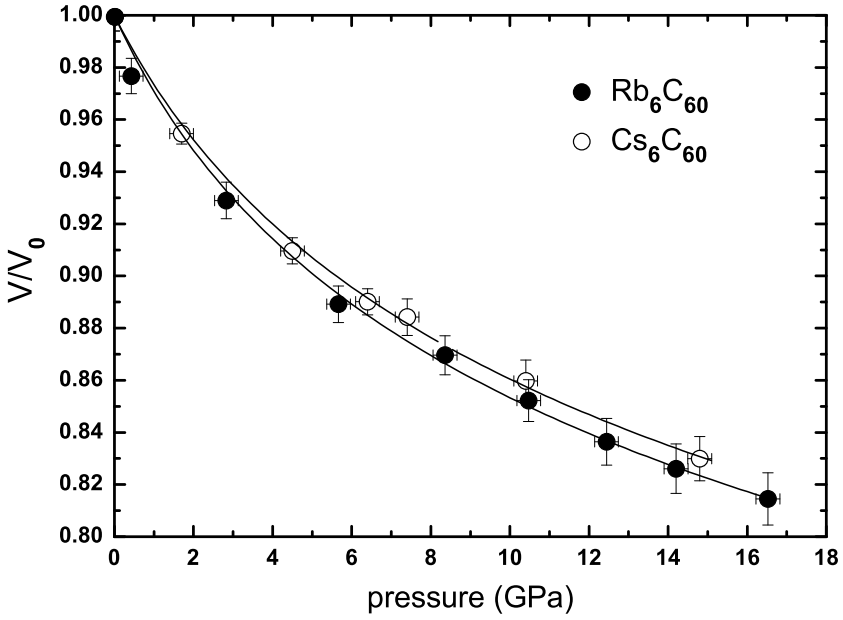

Figure 4.3: *Experimental pressure dependence of the volume of Cs_6C_{60} and Rb_6C_{60} relative to their ambient pressure values as obtained by XRD. We report the best fit curves of the Murnaghan equation of state function for the two systems.*

Our obtained B_0 value for Rb_6C_{60}, 30 GPa, is considerably smaller than the one experimentally found by Sabouri-Dodoran *et al.* [71] by studying the evolution of the lattice parameter on three Bragg reflections with no pressure transmitting medium. They obtained 55.4 and 54 GPa by using the Murnaghan and the Vinet equation of state, respectively. Due to the high correlation (0.98+) between B_0 and its pressure derivative, it is important to consider that in our case B_0', which is 8.5, is significantly higher that those obtained by Sabouri-Dodoran et al. (5.13 and 6.0 for the Murnaghan and Vinet respectively). Nevertheless, the B_0 value that we obtain is smaller compared to their values even if such correlation is taken into account.

In addition, we have also used the Vinet [116, 117] and the Birch-Murnaghan [118] equation of state with results lying within our experimental uncertainty.

system	pressure (GPa)	lattice parameter (Å)
Rb_6C_{60}	AP	11.540(2)
	0.4	11.450(2)
	2.8	11.260(2)
	5.7	11.097(2)
	8.4	11.015(2)
	10.5	10.941(3)
	12.4	10.872(3)
	14.2	10.828(4)
	16.5	10.777(5))
Cs_6C_{60}	AP	11.790(1)
	1.7	11.609(1)
	4.5	11.4236(4)
	6.4	11.3414(4)
	7.4	11.3163(5)
	10.4	11.2109(4)
	14.8	11.0796(5)

Table 4.1: *We report the values of the lattice parameter of Rb_6C_{60} and Cs_6C_{60} for the different values of pressure obtained from the Le Bail fit of x-ray diffraction data. The uncertainty on the values of the pressure are 0.3 GPa while the values of the lattice parameter are reported with the statistical noise obtained from the fit.*

4.4 XAS measurements

The XAS data were measured at the Cs K-edge (35.89 keV) and Rb K-edge (15.20 keV) for Cs_6C_{60} and Rb_6C_{60} from ambient pressure up to 15.7 GPa and 8.2 GPa, respectively. The XANES (X-ray Absorption Near Edge Structure) part of the spectra evolved smoothly in correspondence with the lack of phase transformation as confirmed by the XRD data. The EXAFS data analysis of Cs_6C_{60} and Rb_6C_{60} was performed using the GNXAS package [72, 73]. The extracted signals are shown in Figure 4.4.

The evolution of the structural parameters of the first coordination shell as a function of pressure was obtained by fitting directly the absorption data without any noise filtering or preliminary background substraction.

In the case of Rb_6C_{60}, the Rb K-edge double-electronic excitations [119] have been considered and kept fixed during the fitting procedure to the values obtained from the analysis of data at ambient pressure and room temperature where non-structural components are more clearly observable. In particular the *1s3d* and *1s3p* double excitations

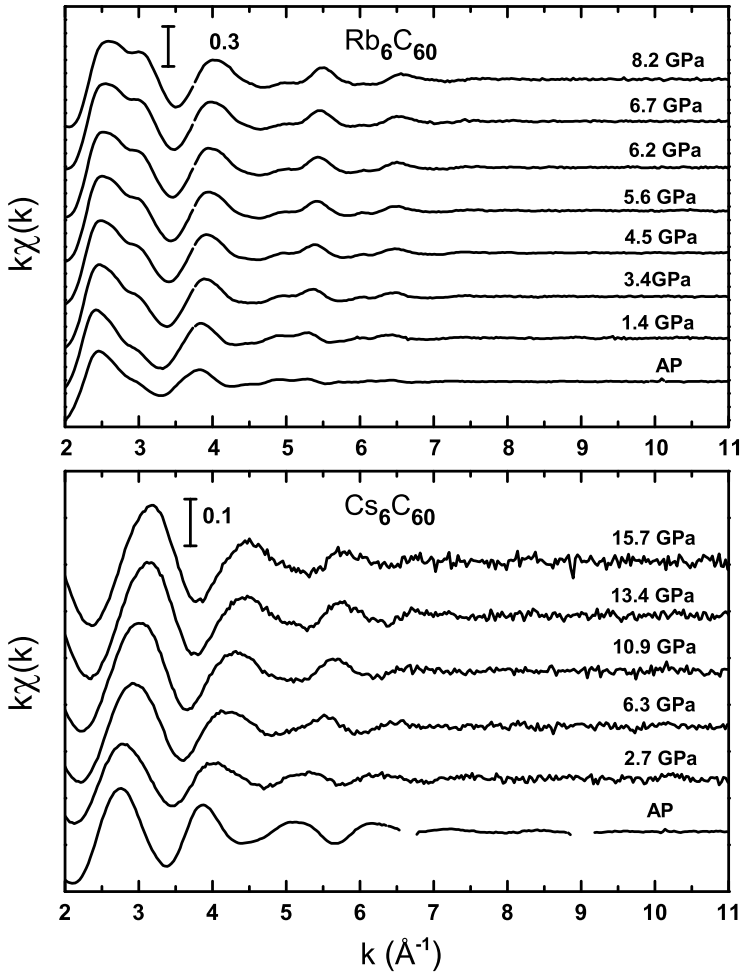

Figure 4.4: *kχ(k) EXAFS signal as a function of pressure for Rb_6C_{60} at the Rb K-edge (upper panel) and Cs_6C_{60} at the Cs K-edge (lower panel). The missing points in the ambient pressure spectrum of Cs_6C_{60} correspond to glitches coming from the monochromator.*

corresponding to shake-off channels have been recognized in our data at $\Delta E = E - E_0$ equal to 122.9 and 142 eV, respectively.

For both systems, the first coordination shell of each alkali atom consists of 22 C atoms, arranged in 2 hexagons and 2 pentagons facing the alkali metal and coming from 4 different molecules: two from the center and two from the vertices sites in the bcc structure with respect to any tetrahedral site of alkali metal atom. In Figure 4.5 we display the local environment, around each alkali atom considered, consisting of the 22 C atoms. The second coordination shell consisting of 4 alkali metal atoms at a distance of 4.114 and

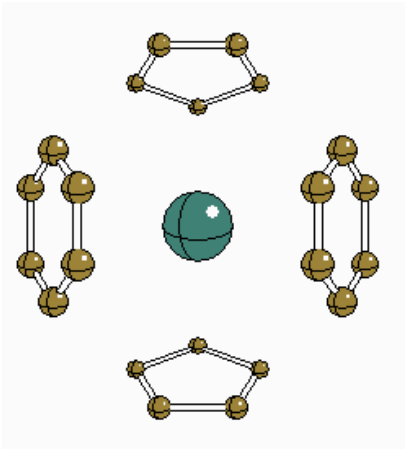

Figure 4.5: *View of the first coordination shell of each alkali metal atom in the studied M_6C_{60} systems. It consists of 22 C atoms, arranged in 2 hexagons and 2 pentagons and the <M-C> distance obtained from our EXAFS analysis (at ambient pressure) is 3.440(1) and 3.550(1) Å, in Rb_6C_{60} and Cs_6C_{60}, respectively.*

4.194 Å[1] (at ambient conditions) in Rb_6C_{60} and Cs_6C_{60}, respectively, was not considered in the fitting procedure for data under pressure because the data quality is not sufficient to include such contribution.

The EXAFS signal of Cs_6C_{60} at ambient pressure and room temperature and the best fit are reported in Figure 4.6. The calculated total signal takes into account the first 22 carbon neighbors and the first 4 Cs neighbors contributions, labelled $k\gamma_1^{(2)}$ and $k\gamma_2^{(2)}$, respectively.

For both systems, Rb_6C_{60} and Cs_6C_{60}, the pressure evolution of the first coordination shell has been studied considering an asymmetric distribution of these C atoms around each alkali metal photo-absorber Rb and Cs atom.

Phases and amplitudes of the EXAFS signals were generated by considering a cluster of 22 carbon atoms and 4 alkali metal atoms around the photo-absorber. Different clusters derived from the compressed structure obtained by our *ab initio* calculations were used as initial inputs for the analysis of the spectra at different pressures. In Table 4.2 we report the structural parameters obtained from the EXAFS analysis: the first coordination shell distance (<M-C>, with M=Rb,Cs), σ^2 which is the variance of the distribution function of the carbon atoms around each alkali metal, and β which is a parameter related to the asymmetry of the distribution (see section 2.1).

In Figure 4.7 we report the relative evolution of the "interstitial" volume (between

[1] These distances of the M-M (M=Rb and Cs) coordination shell in the two systems correspond to those calculated from XRD data and not they have not been obtained from the EXAFS data analysis.

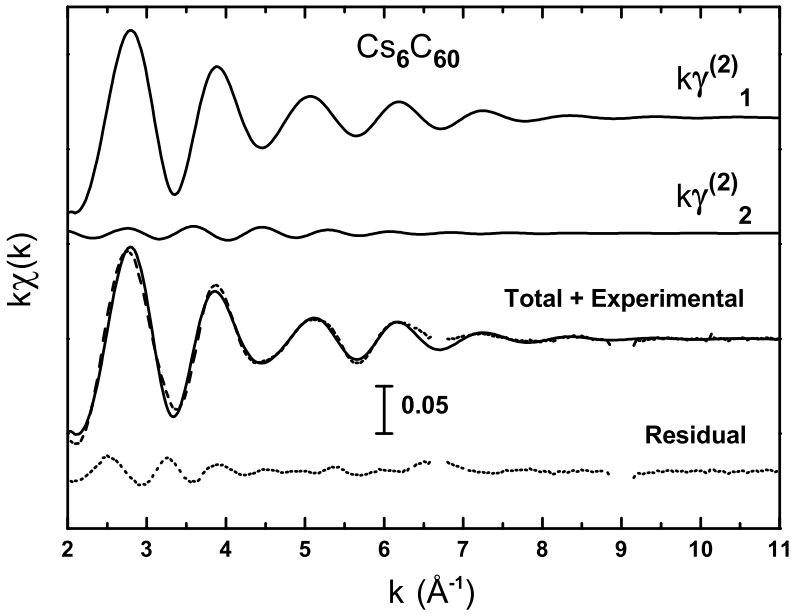

Figure 4.6: *EXAFS signal and fit of the Cs K-edge spectrum of Cs_6C_{60} at ambient conditions. The dashed line corresponds to the experimental signal with the continuous line overlapped corresponding to best fit. $k\gamma_1^{(2)}$ and $k\gamma_2^{(2)}$ are the contributions of the first 22 carbon neighbors and of the 4 first Cs neighbors, respectively. The missing experimental points around 6.7 and 9 $Å^{-1}$ have been neglected because of the presence of glitches.*

the fullerenes) in the bcc structures of Rb_6C_{60} and Cs_6C_{60}. Such volume is obtained by considering a sphere having a radius equal to the EXAFS average distance between the alkali metal and its first neighbor shell of 22 carbon atoms.

We calculated the bulk modulus coefficients of such "interstitial" volume for the two compounds by fitting the experimental values V vs P obtained by the EXAFS analysis with the Murnaghan equation of state and the obtained values are reported in Table 4.3.

We can observe that the "interstitial" volume in the Rb_6C_{60} system is more compressible than in Cs_6C_{60}. They have B_0 values of 13 and 18 GPa, respectively. The $B_0^{'}$ coefficient has been fixed to 5 which is the average value between those obtained for the two systems which were 4 and 6 for Rb_6C_{60} and Cs_6C_{60}, respectively. The choice of a common value of $B_0^{'}$ for both systems allows for a congruent comparison of the compressibility values due to the high correlation between B_0 and its pressure derivative as discussed in the previous section.

system	pressure (GPa)	<M-C> (Å)	σ^2 (Å ^{2})	β
Rb_6C_{60}	AP	3.440(1)	0.051(1)	0.514(1)
	1.4	3.348(2)	0.036(1)	0.460(1)
	1.9	3.3436(2)	0.035(1)	0.361(2)
	3.4	3.249(2)	0.029(1)	0.095(2)
	4.5	3.218(4)	0.027(3)	0.020(5)
	5.6	3.193(4)	0.026(3)	0.000(8)
	6.2	3.170(5)	0.025(4)	0.000(8)
	6.7	3.165(5)	0.024(5)	0.000(8)
	8.2	3.139(6)	0.023(7)	0.000(8)
Cs_6C_{60}	AP	3.550(1)	0.024(1)	0.400(1)
	2.7	3.434(2)	0.038(1)	0.002(1)
	6.3	3.313(2)	0.035(1)	0.000(2)
	10.9	3.218(3)	0.031(3)	0.000(4)
	13.4	3.167(4)	0.029(5)	0.000(5)
	15.7	3.147(5)	0.029(6)	0.000(7)

Table 4.2: Structural parameters <M-C> (first coordination shell distance), σ^2 (variance of the distribution) and β (asymmetry of the distribution) obtained from the EXAFS analysis of Rb_6C_{60} and Cs_6C_{60}.

4.5 *Ab initio* DFT results

We have performed density functional *ab initio* simulations of the two systems under high pressure. In particular, we have used the SIESTA [120] method mentioned in chapter 2. We have used variationally optimized [121, 122] double-ζ polarized basis sets. Real space integrals were performed on a mesh with a 310 Ry cutoff.

Core electrons are replaced by nonlocal, norm-conserving fully separable Trouiller-Martins pseudopotentials. In the calculations *2s* and *2p* orbitals of C atoms were explicitly included in the valence. For the Rb and Cs atoms, we included both semicore and valence orbitals, the *5s* and *4p* and the *6s* and *5p*, respectively. For Cs atoms in particular, the inclusion of both semicore and valence orbitals was found to be critical in order to correctly predict the structural properties of this compound.

The bcc unit cell contains a total of 66 atoms and sampling of the reciprocal space was

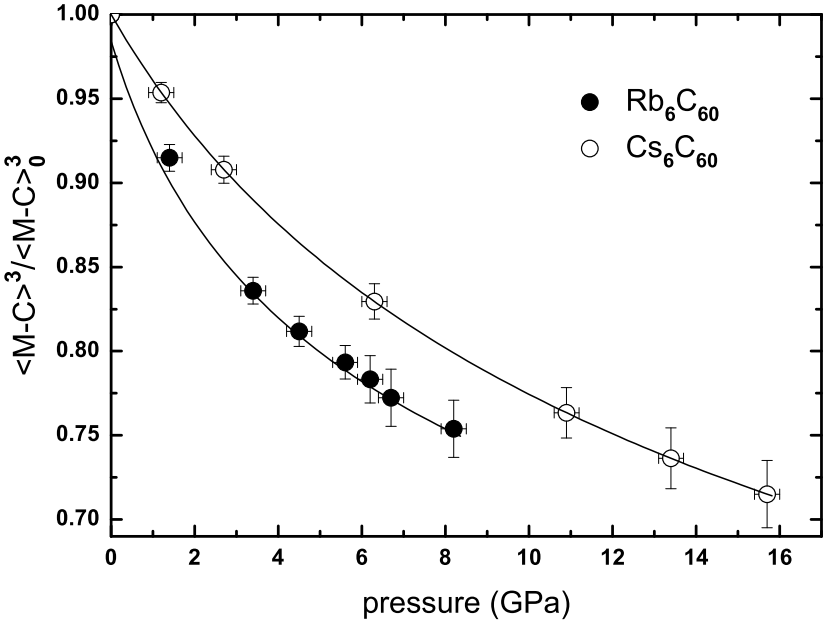

Figure 4.7: *Evolution of the "interstitial" volume of Rb_6C_{60} and Cs_6C_{60} relative to their ambient pressure values as obtained by the EXAFS analysis. We report the best fit curve of the Murnaghan equation of state function for the two systems.*

performed using a $2 \times 2 \times 2$ Monkhorost-Pack mesh.

We studied the structural and electronic evolution of Rb_6C_{60} and Cs_6C_{60} as a function of pressure by decreasing the lattice parameter from the experimental value found at ambient pressure and room temperature (a=11.54 Å and a=11.79 Å) [71] down to 10.70 Å and 11.00 Å, respectively. This corresponds to the following pressure range [-1.8; 15.7] GPa for Rb_6C_{60} and [-1.2; 14.3] GPa for Cs_6C_{60}. The negative values of pressure corresponding to the experimental lattice parameters found at ambient conditions come from the fact that the DFT calculations apply to systems at zero Kelvin temperature. In addition, it must be reminded here, that the use of the LDA approximation is known to give too short distances.

For the different values of the volume we have minimized the total energy until the forces on atoms were smaller than 0.04 eV/Å.

Both the structural and electronic evolution of the two systems confirm the phase stability observed experimentally up to 8.2 and 15.7 GPa for the Rb_6C_{60} and Cs_6C_{60} compounds, respectively.

Both systems are insulators at low pressure with the t_{1u} 3-fold degenerate state completely occupied and a gap between the highest occupied and the lowest unoccupied band gap of 0.66 and 0.63 eV for Cs_6C_{60} and Rb_6C_{60}, respectively. The electronic structure shows a progressive closure of the gap as a function of pressure resulting from the bandwidth broadening consistent with the increase in density. In Figure 4.8 we report the evolution of the gap and the evolution of the bandwidth of the t_{1u} (highest occupied band) and t_{1g} (lowest occupied band) for both systems as a function of pressure. These data show evidence of a pressure induced metallization which should apply in the absence of structural phase transformations.

In Figure 4.9 we show the two E(V) calculated curves. They have been fitted by using the Murnaghan equation of state. The obtained coefficients are reported in Table 4.3. We observe that even if the compressibility values of Rb_6C_{60} (23 GPa) and Cs_6C_{60} (22 GPa) are different from those obtained experimentally, they coincide for the two systems within the error and this result is in close agreement with our experimental observations.

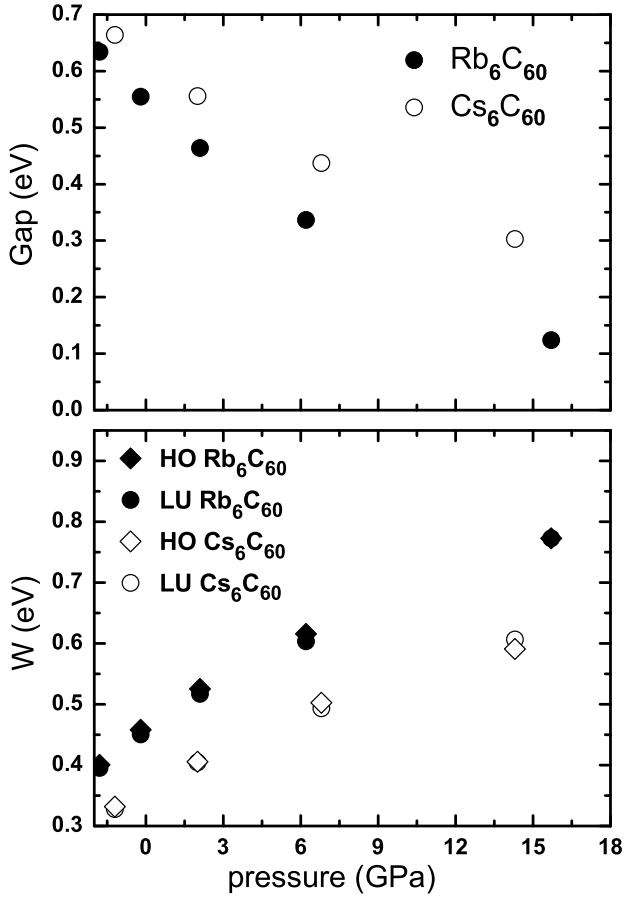

Figure 4.8: *Electronic structure evolution of the two systems as a function of pressure. The evolution of the calculated gap (upper panel) between the highest occupied (HO) and the lowest unoccupied (LU) bands and the bandwidth W (lower panel) as a function of pressure is shown in the picture for both systems. The rhombus symbol in the lower panel corresponds to the highest occupied (HO) bands values.*

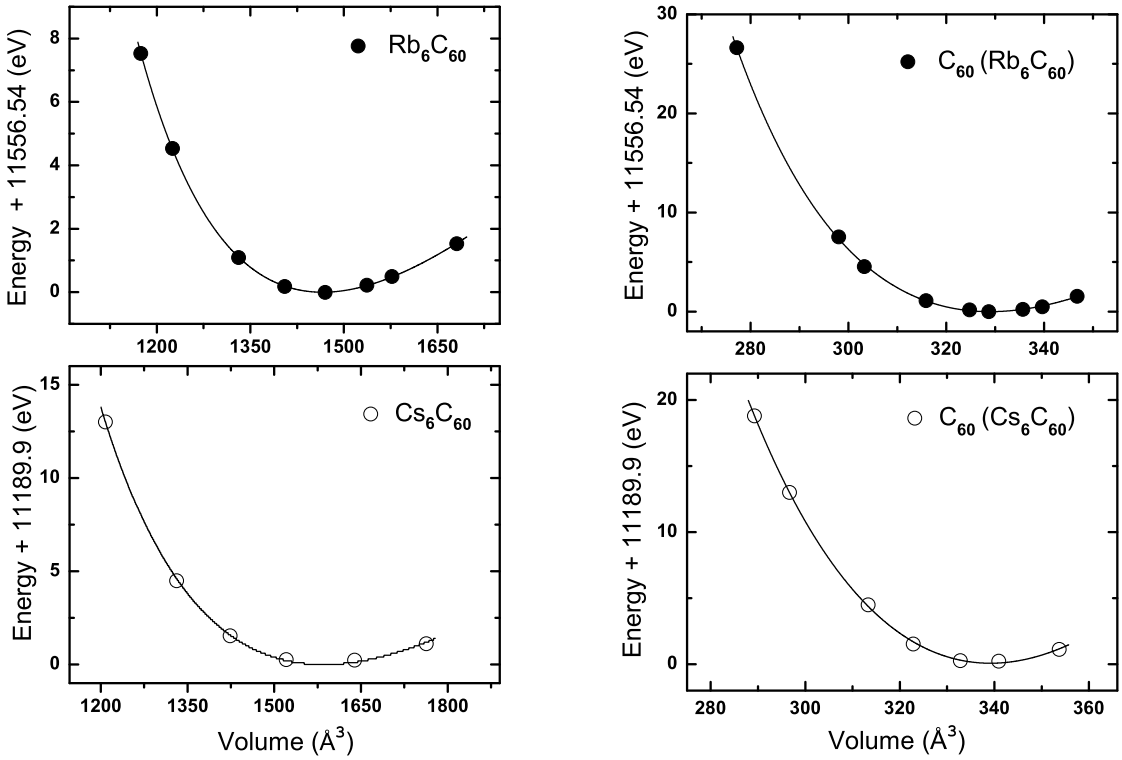

Figure 4.9: *Calculated total energy versus volume for Rb_6C_{60} (upper left panel), Cs_6C_{60} (lower left panel), C_{60} molecule in the Rb_6C_{60} (upper right panel) and Cs_6C_{60} (lower right panel) structure. The continuous line is a fit of the calculated E(V) points by the Murnaghan equation of state.*

However, this is in contradiction with the theoretical work of Ranjan *et al.* [123] where they found bulk moduli of 52.5 GPa and 38.2 GPa for Rb_6C_{60} and Cs_6C_{60}, respectively.

The C_{60} molecule compressibility has been studied in the two different systems. While we cannot partition the total energy of the system into two separated C_{60} and alkaline contributions, we can estimate the C_{60} compressibility by considering the variations of the total energy of the Rb_6C_{60} and Cs_6C_{60} structures as a function of the molecule volume. The volumen of the C_{60} molecule is calculated numerically as a discrete integral of the space enclosed by the 60 C atoms. This is computed in the real grid built in the SIESTA calculation. The E(V) curves are shown in Figure 4.9. The compressibility coefficients have been obtained by fitting the E vs V points with the Murnaghan equation of state and the result is reported in Table 4.3. The C_{60} molecule belonging to Rb_6C_{60} shows a bulk modulus (680 GPa) coefficient higher than for Cs_6C_{60} (530 GPa). Even though these values are smaller than those previously reported for the isolated molecule [43, 44],

	techniques	Rb_6C_{60} B_0 (GPa)	Rb_6C_{60} $B_0^{'}$	Cs_6C_{60} B_0 (GPa)	Cs_6C_{60} $B_0^{'}$
Total volume	XRD	30 ($\pm$3)	8.5 ($\pm$0.5)	33 ($\pm$3)	8.4 ($\pm$0.5)
Total volume	Calculations	23 ($\pm$1)	6.6 ($\pm$0.2)	22 ($\pm$3)	6.6 ($\pm$0.2)
C_{60} volume	Calculations	680 ($\pm$20)	6.4	530 ($\pm$18)	6.4
"Interstitial" volume	EXAFS	13 ($\pm$3)	5	18 ($\pm$3)	5

Table 4.3: *Bulk modulus B_0 coefficients and its derivative $B_0^{'}$ of the two systems obtained from XRD data and ab initio calculations, of the C_{60} molecule in the two different systems as obtained from ab initio calculations and of the "interstitial" volume (<M-C>)^3 obtained from EXAFS data analysis. The errors of the quantities obtained from ab initio calculations correspond to the standard error of the best fit values while for the quantities obtained experimentally also the error propagation has been considered.*

a meaningful comparison cannot be carried out due to our method used for the estimation of the bulk modulus. Nevertheless, the comparison of the compressibility between the two systems, calculated within the same approximation, can be, in principle, fairly made.

4.6 Discussion

Important considerations arise by considering the different experimental and theoretical bulk moduli given in Table 4.3. We should be aware that some of the compressibilities defined here do not correspond to the thermodynamic ones, as they have a local character. Nevertheless, their use has already been found to be extremely useful in the study of isotropic [124] as well as in anisotropic systems [125].

By considering the geometric volume of the fullerene, V_F, the total volume of the bcc fulleride cell, V_T, of the two M_6C_{60} systems can be decomposed as:

$$V_T = 2V_F + nV_i \tag{4.2}$$

nV_i represents the total "interstitial" volume in the bcc unit cell.

We have defined then a volume corresponding to the average distance between the alkali metal atom and the first 22 carbon atoms neighbors as we did in EXAFS, that corresponds to nV_i. The evaluation from *ab initio* calculations of all the variables in eq. 4.2, i.e. V_T, V_F and V_i leads to a value of n equal to 22. By deriving and opportunely reorganizing eq. 4.2 we can then conclude that with a 1% uncertainty, coming from the fact that we

neglect the term associated to the fullerene molecule due to its low compressibility:

$$\frac{B_{0T}}{B_{0i}} = \frac{V_{0T}}{V_{0T} - 2V_{0F}} \tag{4.3}$$

where the T and F labels apply again to total and fullerene respectively.

By using the right side term of eq. 4.3, we obtain a value of approximately 1.3 for both systems. This value differs from the ones that can be obtained by evaluation of the left side of eq. 4.3 using the experimental data in (Table 4.3) which give 2.3 for Rb_6Cs_{60} and 1.8 for Cs_6C_{60}. This represents a difference of 78 and 41 % respectively with respect to the result from the other part of the equation. Consequently we need to conclude that the "interstitial" volume given by EXAFS decreases too rapidly to be considered as representing the real interstitial volume. In addition, such volume reduction appears to be more important in the Rb than in the Cs intercalation case.

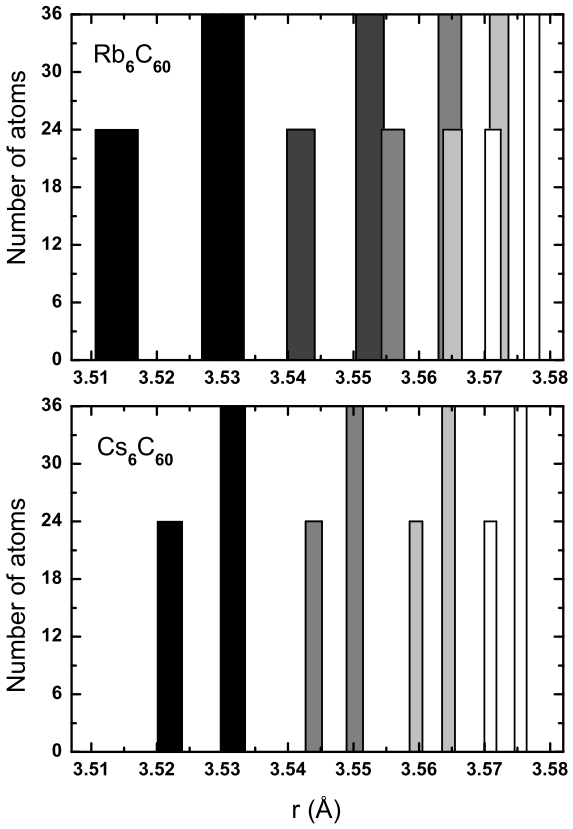

Figure 4.10: Histograms of the ρ distribution for the molecule in the Rb_6C_{60} (upper panel) and Cs_6C_{60} systems (lower panel), for the different pressure values, respectively. We report histograms for -1.8, -0.2, 2, 6.2 and 15.7 GPa and -1.2, 2, 6.8 and 14.3 GPa, for Rb_6C_{60} and Cs_6C_{60}, respectively, starting from the right side of the graphs. The histograms are reported within a spacing between bars equal to 60% meaning that more dispersed distribution are represented with wider columns.

In order to explain such disagreement, we consider the evolution of the geometry of the molecule with pressure as given by our *ab initio* calculations. In Figure 4.10 we show the histogram plot of the evolution with pressure of the distance of the carbon atoms from

the geometric center of the molecule in Rb_6C_{60} and Cs_6C_{60}.

While in the isolated C_{60} molecule with I_h symmetry all C atoms are equidistant from the center, in the studied fullerides the fullerene molecule exhibits a bimodal distribution of distances. This dispersion encountered in the case of the alkali intercalated fullerenes, which characterizes a deformation with respect to the icosahedral symmetry, is further enhanced under pressure. It corresponds to an elongation of the C_{60} cage along the three Cartesian axes and confirms previous studies carried out on Rb_6C_{60} and K_6C_{60} [69] mentioned in section 1.4.1 (Figure 1.13). The origin of the important distortion of the C_{60} molecule in these alkali intercalated compounds can be probably found in the ionic interaction between the fullerene and the intercalated ions.

Let us call ρ the distance of the C atoms from the center of the molecule. We consider then the difference between ρ of each atom and the $\rho_{average}$ quantity obtained as the average between the 60 ρ values. With pressure, the distance of the 60 C atoms from the center decreases and the C_{60} molecule preserves the same distribution of ρ, namely, 36 atoms at $\rho_p > \rho_{average}$ and 24 with $\rho_n < \rho_{average}$. Nevertheless, the shape of such distribution evolves differently for Rb_6C_{60} and for Cs_6C_{60} as shown in Figure 4.10.

We can then define a distortion parameter d as follows:

$$d = \frac{1}{36}\sum_{i=1}^{36}\rho_p(i) - \frac{1}{24}\sum_{i=1}^{24}\rho_n(i) \tag{4.4}$$

In Figure 4.11 we plotted the fullerene distortion parameter d as a function of pressure for both Rb_6C_{60} and for Cs_6C_{60}. It increases with pressure in both cases and for all pressures the distortion induced by Rb intercalation is higher of than for the Cs case.

At the higher pressure studied, i.e. around 15 GPa, d becomes 37 and 24 times higher (for Rb_6C_{60} and Cs_6C_{60}, respectively) than in the isolated molecule. This corresponds to a 54% higher distortion of the C_{60} molecule in Rb_6C_{60} compared to Cs_6C_{60}.

The nature of the pressure induced distortion can be understood by looking at the upper panel of Figure 4.12 where we represent the C_{60} molecule in the bcc Rb_6C_{60} structure surrounded by 24 Rb atoms placed at the tetrahedral sites at the 6 faces. In this picture, the d parameter has been amplified by a factor 27 in order to better appreciate the pressure induced deformation. The pressure induced distortion constitutes basically an amplification of the one already observed at ambient conditions. In conclusion, the shape modification of the C_{60} fullerene can be better interpreted as an elongation of the molecule due to a traction force, in which the molecule is pulled along the 3 cartesian axis through the Coulombic interaction between the negatively charged fullerene and the alkali cations. The observed distortion is considerably smaller than that observed for the

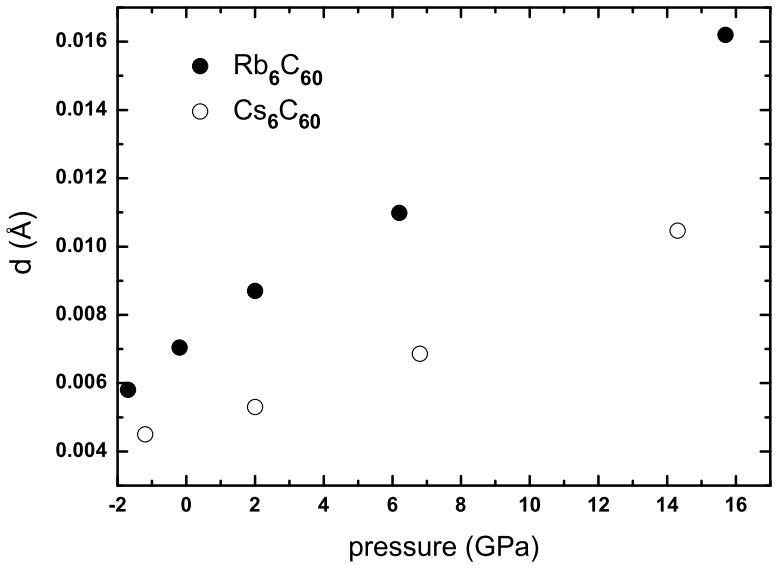

Figure 4.11: *Evolution of the difference between the average value of ρ_p and the average value of ρ_n for different pressure conditions for Rb_6C_{60} and Cs_6C_{60}.*

buckminster-fullerene in single crystal of three-dimensional (3D) polymers of undoped C_{60} by Yamanaka et al. [57]. They observe a cuboidal molecule at ambient pressure with the distortion parameter, according to eq. 4.4, equal to 0.6, i.e. 37 and 57 times higher that the distorion of the fullerene in Rb_6C_{60} and Cs_6C_{60}, respectively, calculated by us at around 15 GPa. This is essentially due to the formation of strong covalent bonds between the molecules in the 3D polymerized structure.

We can now understand the apparent inconsistency that we found when comparing the two terms of eq. 4.3. The pressure induced deformation of the C_{60} molecule leads to an additional reduction of the alkali-carbon distances that needs to be added to simple homogenous compressive effects.

In addition, our calculations show that the deformation of the fullerene in the case of Rb intercalation is stronger than for Cs, consistent with the local compressibilities obtained by EXAFS, where a higher "interstitial" volume compressibility is obtained for Rb_6C_{60} (B_0=13 GPa) with respect to Cs_6C_{60} (B_0=18 GPa). Moreover, although the C_{60} molecule in Rb_6C_{60} appears to suffer a stronger deformation than in Cs_6C_{60}, it is interesting that its stiffness (B_0=680 GPa) is higher than in the case of Cs intercalation (B_0=530 GPa) as obtained by *ab initio* calculations.

In conclusion, this chapter reports a detailed study of the Rb_6C_{60} and Cs_6C_{60} systems under pressure. In particular we coupled the complementary information obtained by XRD and EXAFS with the result obtained by *ab initio* calculations in order to understand the mechanisms taking place during the compression of such systems.

We have calculated and measured the compressibility of both systems and compared this to that obtained by EXAFS for the "interstitial" volumes between molecules. Both for Rb_6C_{60} and Cs_6C_{60} the EXAFS compressibilities appear to be too small to correspond to an isotropic compression of the system. The analysis of the pressure induced deformation of the C_{60} molecule via *ab initio* calculations allows us to understand such differences.

We infer that compression of the C_{60} molecule is accompanied by a shape-changing deformation under pressure. This deformation is analogous to pulling the molecule through the three orthogonal axis pointing towards the bcc faces containing the alkali metals.

Both experiments and calculations agree with a deformation of the fullerene molecule

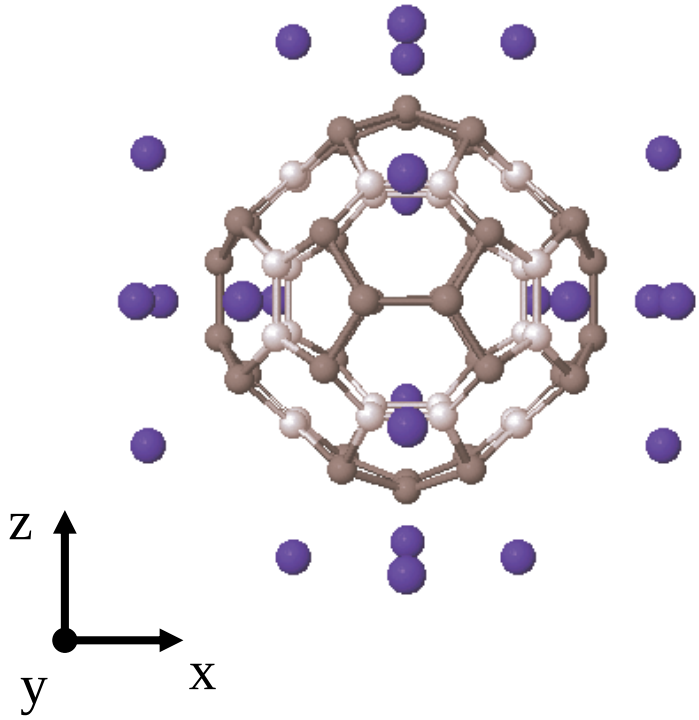

Figure 4.12: *Pressure induced distortion of C_{60}. The distorted C_{60} molecule is represented together with the 24 Rb atoms at the tetrahedral sites (upper panel). We report the molecule at 15.7 GPa with an enhanced distortion such that d has been increased by a factor 27. The 32 C atoms having a greater than average distance from the center, are depicted in dark-grey color while the 24 C atoms having a smaller than average distance from the center, are depicted in light-grey.*

which is more important for Rb than for Cs intercalation. The defined distortion parameter of the fullerene, d, obtained by analysing the evolution of both structures under pressure, is 54% higher in Rb_6C_{60} than in Cs_6C_{60} at around 15 GPa.

Chapter 5

High pressure stability of C_{60} molecules by alkali metal doping in Cs_6C_{60}

In this chapter we study the Cs_6C_{60} molecular crystal by Raman spectroscopy measurements and by *ab initio* calculations, under high pressure. The Raman scattering data have been collected from ambient pressure up to 45.5 GPa, at room temperature. We show that the intercalation of Cesium atoms in the C_{60} crystalline structure allows preserving the C_{60} molecules up to the maximum studied pressure, i.e. more than twice the amorphization pressure of solid C_{60}. In addition, we observe that high resolution measurements allow the detection of six new Raman modes and several partners in doublets in addition to the Raman lines previously observed for the same system. The symmetry of the new observed modes has been identified through our calculations.

5.1 Introduction

The high bulk modulus values calculated for the C_{60} molecule (700 and 900 GPa) [43, 44] make the C_{60} fullerene a good candidate for the constitution of a molecular solid able to sustain very high pressures, a domain which is usually reserved to simple molecular systems, with a very limited number of atoms as diatomic molecular solids. In the pristine fcc structure, i.e. the natural association of the C_{60} fullerenes, such expectations are frustrated by the interaction between molecules, which leads to the amorphization of the structure observed at 22 GPa at room temperature [47, 46]. From that pressure, the signature of the molecular integrity, corresponding to Raman molecular modes, is lost,

implying the destruction of the molecule.

In the present work, we show that the intercalation of solid C_{60} with Cs alkali atoms, leading to the formation of the Cs_6C_{60} compound, allows the molecules to bypass such a limitation, warranting the stability of the C_{60} molecules at pressures of at least 45 GPa.

5.2 Experimental details

The method employed for the synthesis of the Cs_6C_{60} compound is reported in appendix A. The quality of the obtained sample was verified by XRD and is reported in chapter 4.

The sample was loaded into a gasketed diamond anvil cell in a glove box using solid NaCl as pressure transmitting medium. The pressure was calibrated by the R1 fluorescence line of a ruby chip placed in the vicinity of the sample. High resolution Raman spectra ($\sim$ 0.5 cm^{-1}) have been collected at room temperature. The laser beam (514.5 nm exciting line of an Ar^+ laser) was focused down to a 2 micrometer spot on the sample. The optimum laser power was found to be 5 mW, measured directly before the high pressure cell in order to avoid laser heating.

5.3 Raman measurements

For the isolated C_{60} molecule with I_h symmetry, only ten of the 46 calculated vibrational modes are Raman active ($2A_g$+$8H_g$). For the solid fcc C_{60} system, the symmetry-lowering perturbation due to the crystal field associated with the condensed phase gives rise to a very large number of allowed Raman modes. Group-theoretical analysis performed by Dresselhaus *et al.* [126] showed that the solid C_{60} with T_h^6 symmetry, displays 29 one-dimensional A_g modes, 29 two dimensional E_g modes and 87 three-dimensional T_g modes. Nevertheless, several experiments [127, 128, 46] suggested that most of these modes are very weak or give rise to small unresolved splittings of the ten main Raman-allowed modes of the isolated molecule.

For the fully doped Cs_6C_{60} compound with T_h^5 symmetry, calculations [126] show that each of the five-dimensional H_g modes appearing in the isolated C_{60} molecule splits into a two dimensional E_g and a three dimensional T_g modes. Moreover, the $3T_{1g}$, $4T_{2g}$ and $6G_g$ modes in the I_h symmetry should become weakly Raman active changing their symmetry into $3T_g$, $4T_g$ and $6(A_g+T_g)$, respectively.

Low-resolution (6 cm^{-1}) Raman measurements performed at ambient conditions for the fully doped systems M_6C_{60} (with M=K, Rb and Cs) have been previously reported [128, 129, 126]. In that work, ten Raman modes corresponding to the Raman active

modes of the isolated molecule were observed. Hence, they labelled these vibrations for convenience with the names of the irreducible representation of the Raman active modes of the isolated C_{60} molecule with I_h symmetry, i.e. $2A_g$+$8H_g$. In addition, the authors also observed five new lines, corresponding to partners in doublets. In particular, for the Cs_6C_{60} system, four of the H_g modes ($H_g(2)$, $H_g(3)$, $H_g(5)$ and $H_g(7)$) were split into doublets by a measurable amount. For K_6C_{60} and Rb_6C_{60} they also observed a splitting of the $H_g(1)$ mode into a doublet. A more detailed discussion about theoretical predictions compared to experimental observation of new lines in M_6C_{60} solids due to the symmetry lowering from I_h to T_h^5 can be found in Ref. [126].

In the present work, we observe six new Raman modes and eight partners in doublets in addition to the ten Raman active modes of the isolated molecule. The behavior of all the observed lines is followed with pressure.

In Figure 5.1 we display the Raman scattering spectra in the frequency regions 220-900 cm^{-1} and 1050-1680 cm^{-1} respectively, at various pressures at room temperature. The behavior of all the observed lines is followed with pressure. In the following we refer to the previously ten observed intramolecular Raman vibrations as the $2A_g$ and $8H_g$ symmetry modes of the free molecule in order to keep the same nomenclature as used in the past. On the other hand, we label the new observed lines according to the symmetry of the irreducible representation of the Raman active modes of the Cs_6C_{60} system with T_h^5 space group.

The Raman spectra of Cs_6C_{60} were measured from ambient pressure up to 45.5 GPa, at room temperature. Only part of all collected spectra are represented in Figure 5.1 for clarity.

The six new modes are labelled in Figure 5.1 as $T_g(\alpha)$, $T_g(\beta)$, $T_g(\gamma)$, $T_g(\delta)$, $T_g(\epsilon)$ and $A_g(\alpha)$ and their symmetry has been identified through our *ab initio* calculations. Many other low-frequency Raman active modes of solid Cs_6C_{60} associated with intermolecular and molecule-alkali metal motions have been anticipated but they have not yet been observed as they are too weak to be experimentally detected.

Let us first discuss our Raman spectrum at ambient pressure. The ambient pressure frequency of all the observed Raman modes is reported in Table 5.1. The ambient pressure data have been collected on a sample in a closed glass capillary and they show lower quality compared to the high pressure spectra. It is then less evident to distinguish the $T_g(\alpha)$ and $T_g(\beta)$ modes whose evolution as a function of pressure has been clearly followed. For these two modes, the ambient pressure Raman frequency has been extrapolated by using the curbes fitted to the pressure evolution.

Mode	Mode	ω_0	$\partial\omega/\partial P$	$\partial\omega/\partial P$
		cm^{-1}	cm^{-1}/GPa	cm^{-1}/GPa
C_{60}	Cs_6C_{60}	Cs_6C_{60}	C_{60}	Cs_6C_{60}
			up to 22 GPa	up to 22.3 GPa
I_h	T_h	exp. (this work)	Ref. [130], Ref. [46]	this work
$H_g(1)$	$E_g(1)+T_g(1)$	269.9	1.1	2.0
		†	/	2.2
$H_g(2)$	$E_g(2)+T_g(2)$	422.3	2.4, 0.16	0.3
		427.6	/	0.3
T_{2g}	$T_g(\alpha)$	460.3	/	0.5
T_{1g}	$T_g(\beta)$	476.0	/	1.1
$A_g(1)$	$A_g(1)$	494.9	0.75, 0.94	3.0
$H_g(3)$	$E_g(3)+T_g(3)$	657.5	-0.92, -0.55	-0.4
		658.9	/	-0.2
T_{2g}	$T_g(\gamma)$	677.1	/	0.1
$H_g(4)$	$E_g(4)+T_g(4)$	755.9	-0.71, -0.50	2.3
		759.0	/	2.6
T_{2g}	$T_g(\delta)$	730.6	/	-0.1
$H_g(5)$	$E_g(5)+T_g(5)$	1081.9	/	2.6
		1090.0	/	2.4
G_g	$A_g(\alpha)+T_g(\epsilon)$	1116.0	/	3.4
		1122.1	/	3.3
$H_g(6)$	$E_g(6)+T_g(6)$	1229.3	/	4.3
		1235.6	/	4.8
$H_g(7)$	$E_g(7)+T_g(7)$	1382.0	4.12, 2.4	4.4
		N.O.	/	†
$A_g(2)$	$A_g(2)$	1429.0	3.11, 1.7	4.5
$H_g(8)$	$E_g(8)+T_g(8)$	1476.8	2.73, 3.7	3.4
		1491.6	/	3.5

Table 5.1: *Ambient pressure experimental Raman frequencies and first derivative of the least-square fit curves of the linear pressure dependence of all the observed Raman modes of Cs_6C_{60}. The linear fit has been considered up to 22.3 GPa. The pressure dependence of the pristine solid C_{60} Raman lines (up to 22 GPa) are also reported for a comparison. The '†' symbol indicates that the fit was not possible due to the scarcity of the observed Raman lines under pressure.*

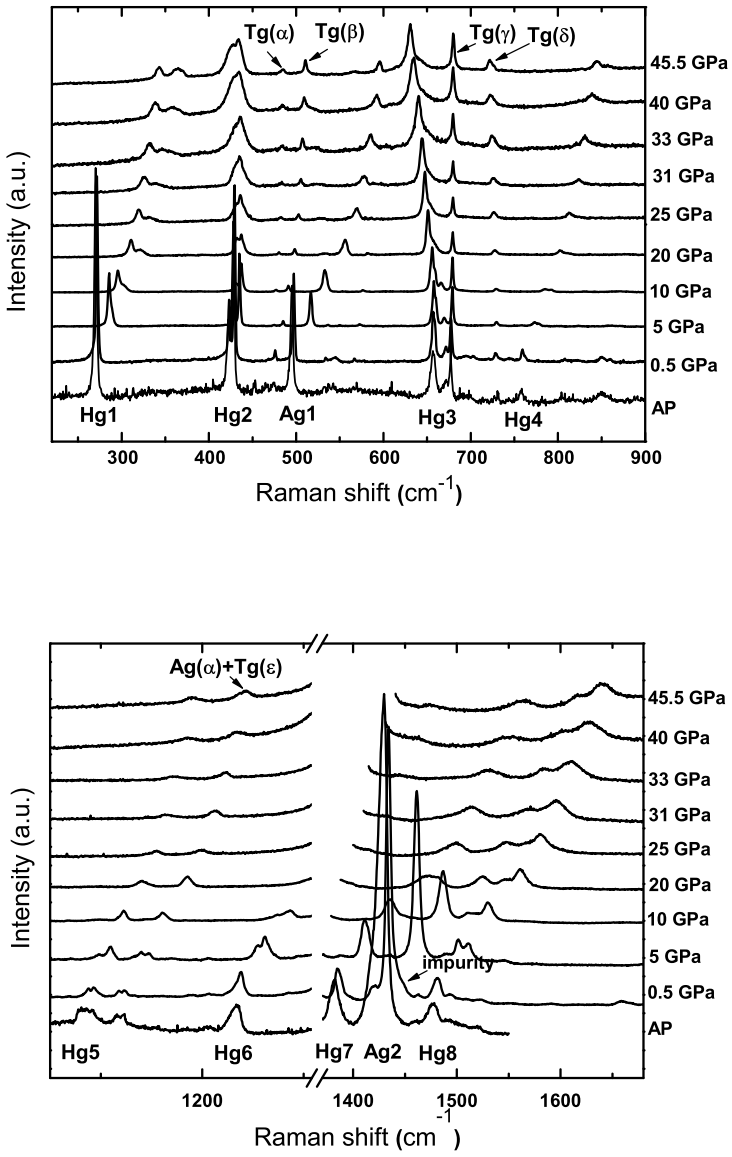

Figure 5.1: *Low-frequency (upper panel) and high-frequency (lower panel) Raman spectra of* Cs_6C_{60} *at room temperature as a function of pressure. The modes are labelled with the names of the irreducible representation of the Raman active modes of the free* C_{60} *molecule, for convenience. A continuous evolution of the intramolecular Raman modes under pressure is observed up to 45.5 GPa. The Raman mode intensity has been normalized to the* $H_g(3)$ *(1st line) intensity mode in the upper panel and to the* $H_g(7)$ *intensity mode in the lower panel. The Raman spectrum at 0.5 GPa shows the presence of a shoulder in the* $A_g(2)$ *mode coming from an impurity also found on the gasket.*

The Raman shifts measured for the previously observed Cs_6C_{60} modes, are in good agreement with those reported in the published works [128, 126, 129].

In Table 5.1 we list the symmetry of the experimentally observed Raman modes in the alkali-metal doped C_{60} system and the corresponding mode symmetry of the isolated fullerene.

In the following, the Cs_6C_{60} Raman spectra evolution under pressure is discussed. In Figure 5.1 we show the evolution of the Raman spectra as a function of pressure from ambient pressure up to 45.5 GPa and in Figure 5.2 the pressure evolution of the Raman frequencies. The continuous evolution of all the Cs_6C_{60} Raman modes as a function of pressure up to 45.5 GPa proves that the presence of heavy alkali metals in solid C_{60} contributes to increase the pressure stability region of the C_{60} molecules of more than 100% in comparison to pristine fcc C_{60} where previous studies have shown an irreversible transition at 22 GPa accompanied by the loss of the intramolecular C_{60} modes [130, 46]. In Figure 5.1 we observe that most lines show an increase of their frequency with pressure with the exception of $H_g(2)$, $H_g(3)$ and $T_g(\delta)$ which slightly soften linearly with pressure and the $T_g(\alpha)$ and $T_g(\gamma)$ modes which essentially do not show any change in frequency. A Raman spectrum collected at a pressure of 5 GPa after pressure release from the highest measured pressure, shows that the Raman mode evolution is reversible.

The evolution of the Raman spectra with pressure has been firstly considered in a reduced range of pressure (up to 22.3 GPa) in order to compare our results with those previously obtained for the non intercalated solid C_{60} (see Table 5.1) up to 22 GPa. In this limited range of pressure the frequency evolution of the observed Raman modes can be considered with good approximation a linear function of pressure. The pressure dependence of the eight H_g lines associated to intramolecular vibrations is similar to that of solid fcc C_{60} while the Raman frequency of the two A_g modes show a stronger dependence on pressure than for pristine C_{60} [130, 46]. In fact, the Raman shift of the $A_g(1)$ mode increases as a function of pressure and its slope (3.0 cm^{-1} GPa^{-1}) is approximatively four times larger than in pristine C_{60} (0.75 cm^{-1} GPa^{-1} in Ref. [130] and 0.94 cm^{-1} GPa^{-1} in Ref. [46]). As $A_g(1)$ is a nearly 100% radial mode [131], in the case of alkali metal intercalated C_{60}, namely Cs_6C_{60}, the presence of Coulomb interactions contributes to rapidly increase the "breathing" mode frequency with pressure, more than in the non-intercalated solid C_{60}. The compression of the C_{60} molecules with pressure [132] coupled to the presence of ionic interactions in the system are probably responsible for such high value of the pressure derivative of the $A_g(1)$ mode, in Cs_6C_{60}. The frequency increase of the $A_g(1)$ radial mode upon doping, was previously explained by Jishi and Dresselhaus

[133] by considering the variation in the electric field at the sites of the negatively charged carbon during a vibration. This variation produces an extra radial force on these atoms responsible for the increase in the bond-stretching force constant. In addition, the effect of pressure is to decrease the separation between the centers of the ions and the C_{60} sphere causing an increase of the electrostatic interaction and finally an increase of the Raman shift frequency of the $A_g(1)$ vibration. This is very similar to the case of alkali-metal intercalated systems with small dopant ions whose increase in the $A_g(1)$ mode frequency with respect to solid C_{60} has been observed to be bigger than for larger alkali metals [129].

For the pentagonal-pinch (PP) $A_g(2)$ mode we have found a value of 4.5 cm^{-1} GPa^{-1} which is much larger than the values obtained for solid C_{60} [46, 130]. On the other hand, this value is very close to that found for Cs_3C_{60} by Fujiki *et al.* [134] which is 4.0 cm^{-1} GPa^{-1}. We want to remind here that the $A_g(2)$ mode, which is a nearly 100% tangential mode, has been observed to soften after the intercalation of Cs atoms (6 cm^{-1} per alkali metal) into the C_{60} lattice at ambient pressure [128, 129] due to an elongation of the average C-C bond length caused by the charge transfer to the antibonding LUMO states of the C_{60} molecule [4]. Then, we observe that in Cs_6C_{60} compounds, (as also in the case of Cs_3C_{60}) the application of pressure increases the intraball force constant of the C_{60} molecule, more than in the case of pristine C_{60}.

Finally, the two $T_g(3)$ and $E_g(3)$ soft modes (deriving from the $H_g(3)$ mode) in Cs_6C_{60} are harder than in the pristine C_{60} system. The most intense line at 657.5 cm^{-1} at ambient pressure has a pressure coefficient of -0.4 cm^{-1} GPa^{-1} which is 30 % and 57 % smaller than the values observed for the $H_g(3)$ mode in solid C_{60} [46, 130]. This could be considered a signature of the higher stability of the fullerene molecule in Cs_6C_{60} with respect to the non intercalated C_{60}.

When considering the pressure evolution of the Raman modes up to 45.5 GPa, it turns out that their dependence as a function of pressure is no more linear for the majority of the Raman lines (Figure 5.2). A parabolic function, which constitutes a first approximation of an exponential-decay function, is able to reproduce the behavior of the Raman modes with pressure. This can be considered as an indication of anharmonic effects [135]. In Table 5.2 we report the linear and quadratic terms corresponding to the parabolic fit of the pressure dependence of the observed Raman modes up to 45.5 GPa.

5.4 Raman spectra calculation

In parallel to experiments we performed density functional *ab initio* simulations to calculate the zone center vibrational modes of Cs_6C_{60} under pressure.

We have used the SIESTA [120] method discussed in chapter 2. More details about the calculations are reported in section 4.5.

We studied the frequency evolution of the Raman modes of Cs_6C_{60} as a function of pressure by decreasing the lattice parameter from the experimental value found at ambient pressure and room temperature (a=11.79 Å) down to 10.00 Å. This corresponds to the pressure range [-1.2; 98] GPa.

For the different volume values, we have minimized the total energy until the forces on atoms were smaller than 0.04 eV/Å [132].

The bcc unit cell contains a total of 66 atoms and sampling of the reciprocal space was performed using a $2 \times 2 \times 2$ Monkhorst-Pack mesh. We obtain the dynamical matrix using a finite differences approach, where the atoms were displaced by Δx=0.2Å. The Hellmann-Feynman forces were calculated for all the atoms in the system, fully building the dynamical matrix.

We used a bond polarizability model, reported in Ref. [136] and described in appendix B, in order to calculate the intensity of the first-order off-resonance Raman scattering. The Raman polarizability parameters of single and double bonds in C_{60}, used in this work are also reported in appendix B. They have been obtained in Ref. [136] by fitting experimental off-resonance Raman spectra of solid C_{60} with such model.

The predicted intensity is somewhat different from that experimentally observed. This is due to the fact that the polarizability parameters for C atoms in Cs_6C_{60} should radically differ from those in the isolated C_{60} because of the charge transfer and also because the single and double bond lengths change with pressure. Indeed the higher the pressure the worse is the prediction of the Raman intensities, an indication of the degradation of the original polarizability parameters. However, the model is a practical tool to easily identify the Raman activity of the modes, allowing us to tightly discriminate between all the 192 modes in the spectrum.

We studied the frequency evolution of Raman active modes as obtained by *ab initio* calculations together with the polarizability model. The results are reported in Figure 5.2 and Table 5.1. We report only the theoretical results obtained up to 43 GPa for a more clear comparison with experiments.

Nevertheless, the calculations show that all Raman modes observed at low pressures

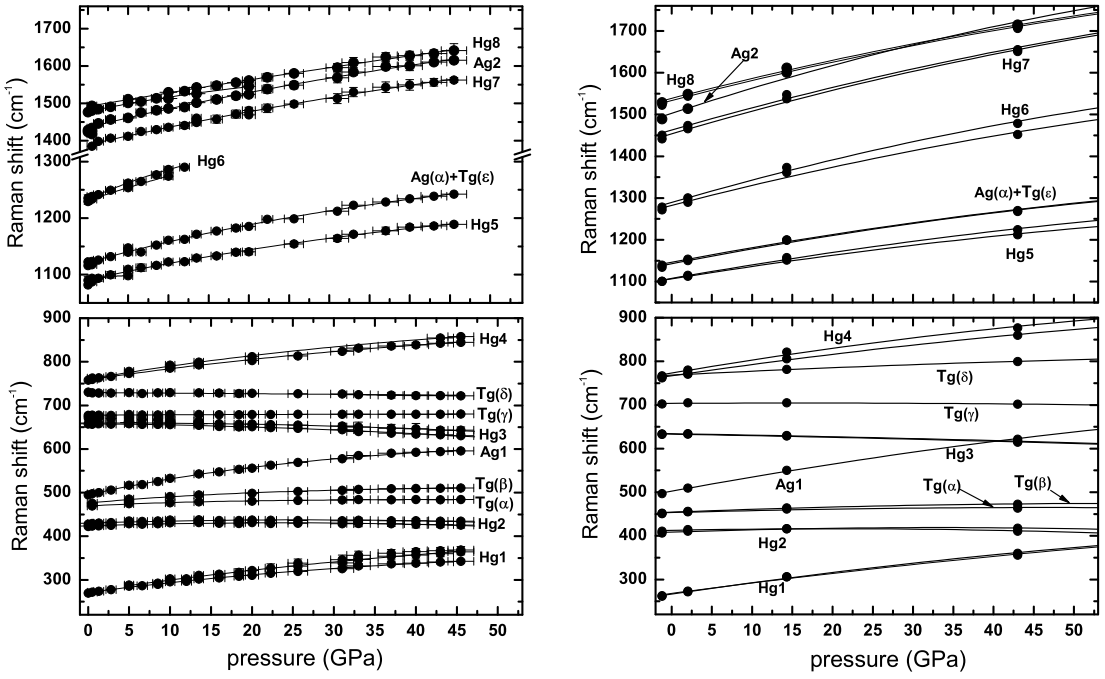

Figure 5.2: *Pressure dependence of the low-frequency and high-frequency Raman modes of Cs_6C_{60} from ambient pressure up to 45.5 GPa and 43 GPa as obtained from experiments (left panels) and calculations (right panels), respectively. The solid lines correspond to least-square fits to a parabolic pressure dependence for most modes. The horizontal error bar represents the pressure uncertainty estimated from the Lorentzian width of the ruby R1 line; the vertical error bar are the half width at half maximum (HWHM) of each Raman mode.*

remain active even at very high pressure (98 GPa). The ten Raman modes ($2A_g$+$8H_g$) observed experimentally and previously labelled for convenience with the names of the irreducible representation of the Raman active modes of the isolated C_{60} molecule, have been well identified in our calculations.

We observed a splitting of each H_g mode into a two-dimensional E_g mode and a three-dimensional T_g mode, as predicted by group theory [126] and observed from our experiments. Moreover, the six new observed lines, labelled as $T_g(\alpha)$, $T_g(\beta)$, $T_g(\gamma)$, $T_g(\delta)$, $T_g(\epsilon)$ and $A_g(\alpha)$, have been well identified in this study and they all have been found to have three-dimensional T_g symmetry except for the $A_g(\alpha)$ mode. The calculated first and second derivatives of the pressure dependence of the frequencies of all the Raman modes are reported in Table 5.2 for a comparison with the experimentally obtained values. The fitted curves of the calculated pressure evolution frequencies reported in Table 5.2 have

been considered only up to 43 GPa in order to better compare experiments and theory. We observe a good agreement between experiments and calculations.

In conclusion, both experiments and calculations show that the molecular character of the C_{60} fullerene can be maintained through alkali intercalation up to pressures at least two times higher (around 45 GPa) than for the previously reported pure solid C_{60} (around 22 GPa). At the same time, as shown in chapter 3 and also in Ref. [132] a progressive pressure-induced deformation of the molecule takes place due to the pressure enhanced Coulombic interaction between the fullerene and the alkali metal atoms. Our study shows that, in spite of such -slight- deformation, the molecular character of the 60-atom fullerene is maintained. This will allow to envisage fullerene exohedral intercalation as a path to preserve the properties of encapsulated atoms or molecules in these or larger fullerenes, at very high pressures.

Mode Cs_6C_{60} T_h	ω_0 cm^{-1} Cs_6C_{60} exp.	ω_0 cm^{-1} Cs_6C_{60} cal.	$\partial\omega/\partial P, \partial^2\omega/\partial P^2$ $cm^{-1}/GPa, cm^{-2}/GPa^2$ Cs_6C_{60} up to 45.5 GPa exp.	$\partial\omega/\partial P, \partial^2\omega/\partial P^2$ $cm^{-1}/GPa, cm^{-2}/GPa^2$ Cs_6C_{60} up to 43 GPa cal.
$E_g(1)+T_g(1)$	269.9	261.5 *	2.4/-0.02	3.2/-0.02
	†	262.6	2.6/-0.01	3.1/-0.02
$E_g(2)+T_g(2)$	422.3	406.7 *	0.6/-0.01	0.7/ -0.01
	427.6	410.8	0.6/-0.01	0.5/-0.01
$T_g(\alpha)$	460.3	450.8	0.7/-0.01	0.8/-0.01
$T_g(\beta)$	476.0	452.2	1.4/-0.02	1.7/-0.02
$A_g(1)$	494.9	496.7	3.8/-0.04	3.7/-0.02
$E_g(3)+T_g(3)$	657.5	632.4	-0.2/-0.01	-0.2/-0.01
	658.9	633.6 *	0.1/ -0.01	-0.2/-0.01
$T_g(\gamma)$	677.1	702.4	0.1/-0.001	0.2/-0.01
$E_g(4)+T_g(4)$	755.9	762.0	2.7/-0.02	3.1/-0.02
	759.0	765.0 *	3.1/-0.02	4.1/-0.04
$T_g(\delta)$	730.6	766.7	-0.02/-0.003	1.0/-0.01
$E_g(5)+T_g(5)$	1081.9	1100.6*	2.9/-0.02	3.6/-0.03
	1090.0	1100.7	3.8/ -0.03	4.1/-0.03
$A_g(\alpha)+T_g(\epsilon)$	1116.0	1134.3	†	4.7/-0.04
	1122.1	1139.2 *	3.8/-0.03	4.4/ -0.03
$E_g(6)+T_g(6)$	1229.3	1271.7*	5.2/-0.08	6.6/-0.06
	1235.6	1278.2	5.2/-0.04	6.9/-0.06
$E_g(7)+T_g(7)$	1382.0	1441.7	4.9/ -0.02	6.8/-0.05
	N.O.	1450.4*	/	7.0/-0.06
$A_g(2)$	1429.0	1489.0	5.2/-0.03	8.2/-0.07
$E_g(8)+T_g(8)$	1476.8	1522.1	4.2/-0.05	6.3/-0.05
	1491.6	1528.9*	3.7/-0.01	5.9/-0.04

Table 5.2: *Ambient pressure Raman frequencies and first and second derivatives of the least-square fit to a parabolic pressure dependence for all modes for both experiments and calculations. In the latter case a fit up to 43 GPa, instead of 98 GPa, has been considerend in order to better compare the results with the experiment. The '*' symbols refer to the T_g symmetry modes. The '†' symbol indicates that the fit was not possible due to the scarcity of lines, observed under pressure.*

Chapter 6

High pressure phase transition in Rb_6C_{60}

In this chapter we present high pressure (HP) and high temperature (HT) studies, carried out on Rb_6C_{60}, by performing x-ray diffraction (XRD), x-ray absorption (XAS) and Raman spectroscopy measurements. In particular, the occurrence of a reversible transition has been clearly identified at around 35 GPa both at 600 K and at room temperature, by XRD and Raman measurements, respectively. The XRD data show that the new phase is compatible with a hexagonal unit cell structure with a=8.360(2) Å and c=14.830(7) Å at 43 GPa and 600 K. At the Raman transition, Raman spectra exhibit an abrupt change in the frequency of the normal vibrations. We speculate that the observed first order bcc → hexagonal structure transition is accompanied by a 2D polymerization of the C_{60} molecules along the (001) plane.

6.1 Introduction

As discussed in more detail in chapter 1, the initial motivation of this work was the synthesis under high temperature and high pressure conditions of three dimensional C_{60} polymers in the presence of alkali metals. In fact, these new materials are expected to exhibit both high hardness and superconducting properties.

In this chapter, we present an accurate study on the evolution of the Rb_6C_{60} system, under high pressure and high temperature conditions, in order to check for the occurrence of phase transitions leading to the formation of such high-dimensional polymers.

On the other hand, in the previous chapter we reported a Raman spectroscopy study showing that the Cs_6C_{60} compound displays an exceptional structural stability under

high pressure [137] (up to 45 GPa). In the present chapter, the Raman scattering study of Rb_6C_{60} as a function of pressure allows to compare the high pressure evolution of the intramolecular vibrations to the case of Cs_6C_{60}.

6.2 Experimental details

The method employed for the synthesis of the Rb_6C_{60} compound is reported in appendix A. The XRD data reported in the next section evidence the quality of the obtained sample.

HP and HT XRD and XAS experiments were performed using diamond anvil cells (DACs) with the x-ray beam traversing the two 2.5 mm diamonds.

The energy dispersive XAS measurements were performed at the insertion device ID24 beamline [138, 139] in transmission geometry. The beam was focused down to $10\mu m \times 10\mu m$ FWHM (full width at half maximum).

Angular dispersive XRD experiments were performed at the insertion device ID27 beamline [110] by angle-resolved measurements. The monochromatic beam was selected to have wavelength λ=0.3738 Å and λ=0.2647 Å for high temperature and room temperature measurements, respectively. The focal spot size was $7\mu m \times 7\mu m$ (FWHM). The diffraction patterns were recorded on a fast large area scanning MAR345 image plate and ona detector-Bruker CCD for the high temperature and room temperature experiments, respectively.

High pressure (HP) room temperature (RT) Raman spectra were recorded on a Jobin-Yvon HR-800 Labram spectrometer with double-notch filtering and air cooled CCD detector (ENS, Lyon). More experimantal details concerning the Raman experiment can be found in section 5.2.

For all the experiments, the pressure was measured *in situ* before and after each measurement using the R1 fluorescence emission of a ruby chip placed into the gasket hole. We used LiF as pressure transmitting medium for HP-HT XRD measurements and NaCl for the HP-RT XRD and Raman spectroscopy measurements. No pressure transmitting medium was used during the XAS measurements in order to provide a more suitable sample thickness for a good signal-to-noise ratio.

The HT conditions for XAS and XRD experiments were achieved by external resistive heating and the temperature was measured using a thermocouple placed on the back of one diamond.

For HP-HT XAS and XRD experiments we used a Re gasket with a 100 μm diameter hole while for the HP-RT temperature Raman measurements we used a stainless steel

gasket with a 100 μm diameter hole.

6.3 XRD measurements

We performed XRD measurements in the P-T range of [AP:49.5 GPa] and [RT:600 K]. We studied the evolution of the solid structure of Rb_6C_{60} as a function of pressure both at HT (600 K) and at RT. XRD patterns were collected after each pressure increase by $\sim$ 1.5 GPa. In Figure 6.1 we report only part of the collected patterns from 7 up to 43 GPa at HT (lower panel) and from 6.5 up to 49.5 GPa at RT.

The data set collected at 600 K displays a clear phase transition of Rb_6C_{60} towards a lower-symmetry structure corresponding to the appearence of additional Bragg reflections starting from 36.5 GPa. At 43 GPa, which is the highest measured pressure, the phase transition was observed to be complete.

Two different experiments were performed in order to check the transition reversibility dependence on the thermodynamic path. Firstly, we performed the pressure release at high temperature and once we reached ambient pressure we cooled the sample down to room temperature. The second experiment consisted in cooling the sample down to room temperature at high pressure and then we performed the pressure release.

In both experiments the transition was observed to be reversible but with different hysteresis ranges. The body-centered cubic phase was back at 32 GPa and at 11 GPa in the first and the latter case, respectively. In Figure 6.2 we display the XRD data collected at 600 K during the pressure release showing the reversibility of the transition.

For data collected at RT as a function of pressure (upper panel of Figure 6.1) it is difficult to establish which structural modification is taking place above 45.6 GPa, due to the broadening of the Bragg reflections at such pressure. Nevertheless, we can observe that such increase in the Bragg peaks width is discontinuous, suggesting the occurrence of a structural change in correspondance of such discontinuity.

All data were analyzed using the FULLPROF package [114] before and after the phase transition within the Le Bail configuration.

The new structural phase of Rb_6C_{60} was found to be compatible with a hexagonal unit-cell structure by indexing the powder diffraction patterns with a dichotomy method. In particular we used the DICVOL program [141]. Among the different solutions only the lattice parameters of the hexagonal cell were found to be compatible with a network built of C_{60} molecules. The resulting lattice parameters at 43 GPa and 600 K are a=8.360(2) Å and c=14.830(7) Å. The corresponding c/a ratio is 1.774, only 8% bigger than the ideal

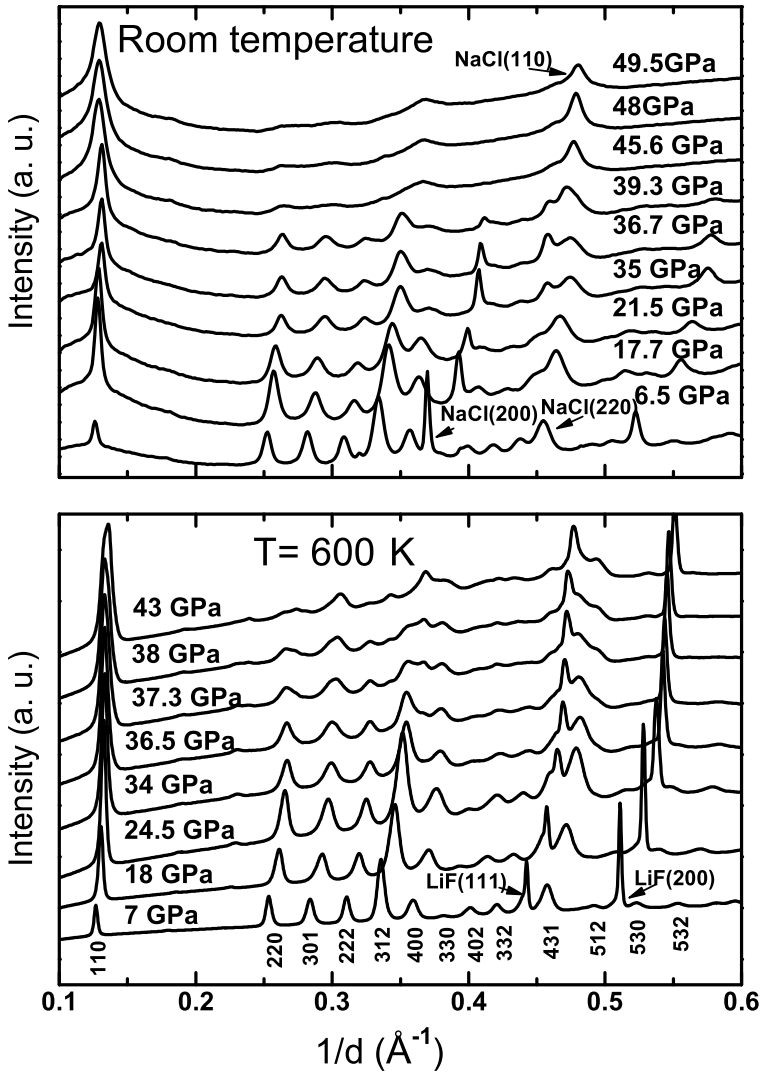

Figure 6.1: *Upper panel: room temperature and high pressure XRD patterns of Rb_6C_{60} and NaCl (used as pressure transmitting medium), normalized for acquisition time and collected at λ=0.2647 Å. The B1→B2 NaCl is also observed at around 39 GPa [140]. Lower panel: high temperature (600 K) and high pressure XRD patterns of Rb_6C_{60} and LiF (used as pressure transmitting medium), normalized to LiF (111) Bragg reflection intensity and collected at λ=0.3738 Å. All data are reported without any background subtraction.*

axial ratio c/a for a hexagonal close-packed crystal structure (1.633). The corresponding Le Bail fit performed by imposing the $P6/mmm$ space group is shown in Figure 6.3 and

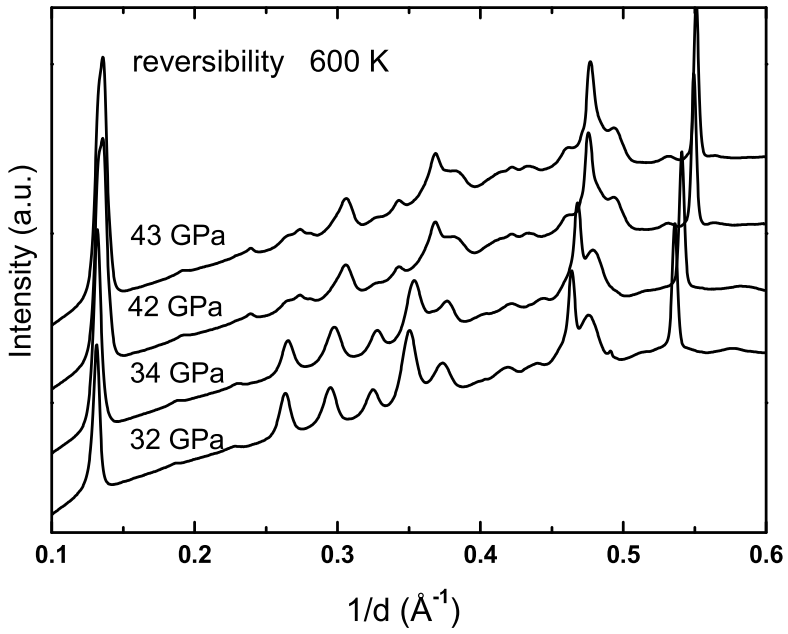

Figure 6.2: *XRD data collected on Rb_6C_{60} at 600 K, from the highest measured pressure (43 GPa) down to 32 GPa during the pressure release. The observed XRD transition is reversible and the cubic phase is back at 32 GPa. Data are normalized to the LiF (111) Bragg reflection intensity.*

the weighted profile R-factor which gauges the quality of the fit is R_{wp}=6.5% (χ^2=0.29). Unfortunately, due to the quality of the data at high pressure, a Rietveld-type refinement was not possible, preventing us from obtaining information about the atomic positions in the unit cell.

6.4 XAS measurements

XAS spectra of Rb_6C_{60} were collected at the Rb K-edge (15.2 keV) as a function of pressure both at room temperature and at 600 K. The XANES (x-ray absorption near edge structure) signals of some of the collected spectra are shown in Figure 6.4. Due to the unavoidable Bragg reflections from the diamond anvils, data were collected up to 200 eV above the edge, preventing EXAFS (extended x-ray absorption fine structure) analysis.

Since a detailed XANES analysis was not possible due to the difficulty in reproducing the signal at ambient conditions, in the following we only report qualitative considerations

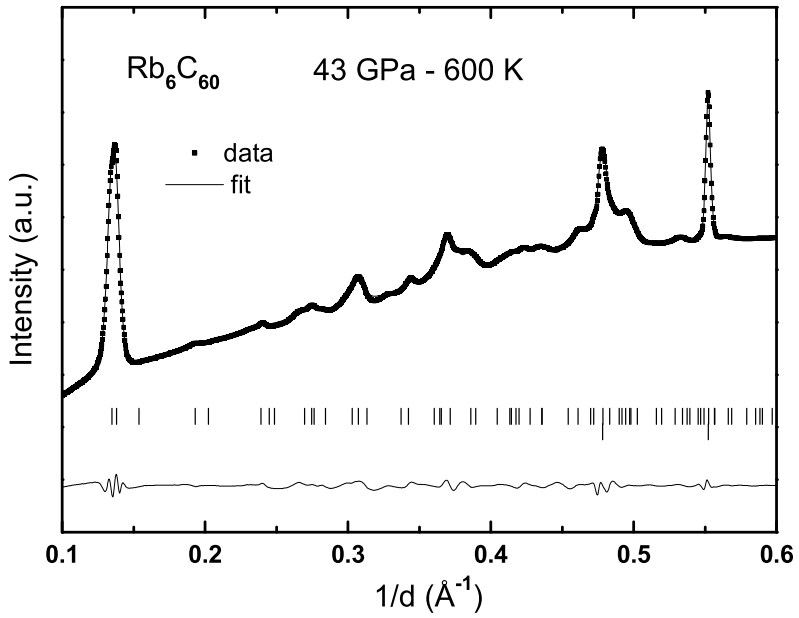

Figure 6.3: *Le Bail fit of the XRD pattern collected on Rb_6C_{60} at 43 GPa and 600 K (R_{wp}=6.5 % and χ^2=0.29). The ticks correspond from bottom to top to LiF and Rb_6C_{60}. The data and the fit curve are reported in dotted and solid line, respectively. The lower line corresponds to the residual pattern.*

on the pressure evolution of the spectra. For this reason, in Figure 6.4 we report two different views of the evolution of the XANES spectra as a function of pressure, in order to better appreciate their change with the structural compression.

In both RT and HT experiments, we do not observe any clear modification with pressure of the edge position within the precision of our measurements (± 0.4 eV) indicating that no clear change in the electronic charge transfer from the alkali metals to molecules can be established.

A continuous and progressive evolution of the XANES signal as a function of pressure is observed both at room and at high temperature. This evolution is characterized by: i) a progressive enlargement of the white line with a slight fall in intensity; ii) a modification of the shape of the following XANES oscillation: this, initially exhibiting a doublet resonance, gradually shows an intensity decrease of the first peak and globally shifts towards higher energies; iii) the progressive disappearence of the second oscillation located at around 15.27 keV (at lower pressure).

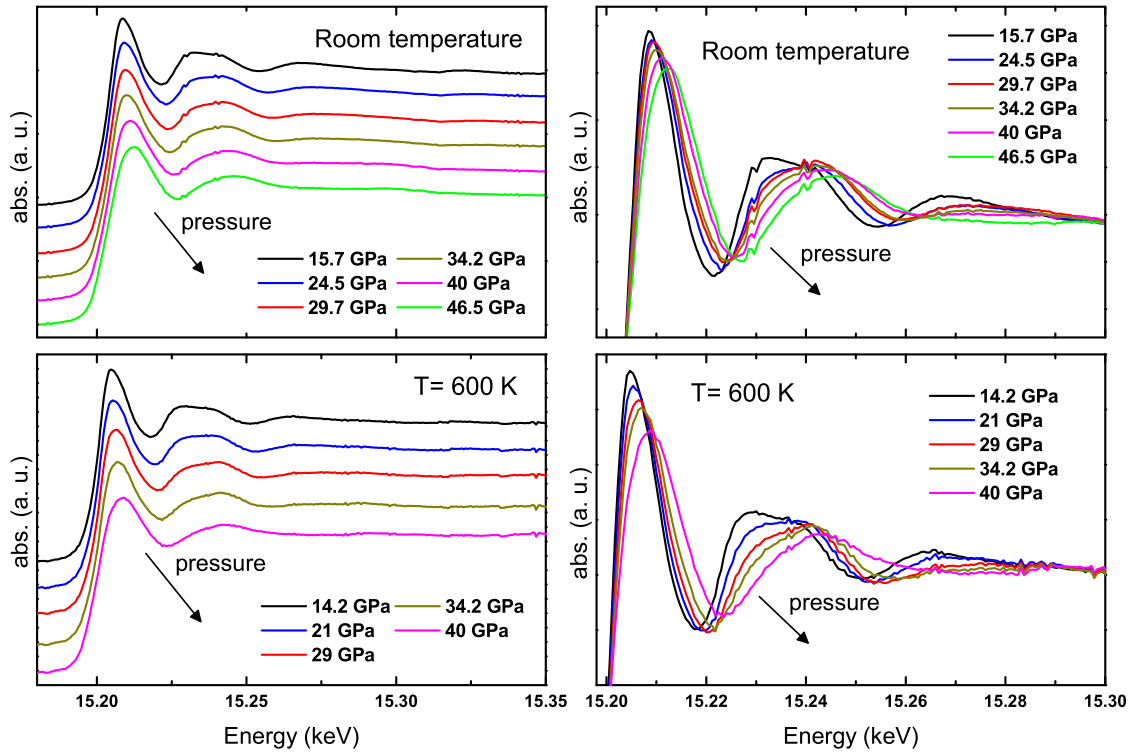

Figure 6.4: *Two different views of the Rb K-edge XANES spectra of* Rb_6C_{60} *as a function of pressure at room temperature (upper panels) and at 600 K (lower panels).*

For both experiments the release of pressure was performed at RT. For the experiment performed at 600 K, during the pressure release we collected data down to 22 GPa while for the experiment performed at RT, we collected data down to 15 GPa. In both cases we observe a similar progressive reversibility of the signal. Figure 6.5 displays the XANES spectra collected on Rb_6C_{60}, by decreasing pressure from 40 down to 22 GPa, after cooling the sample down to RT. The pressure release was performed in this way in order to try to metastabilize the HT-HP phase.

6.5 Raman measurements

Raman spectra of Rb_6C_{60} were collected at ambient temperature as a function of pressure from 0.3 GPa up to 40.3 GPa. Only a few spectra collected are reported in Figure 6.6 for clarity.

For the fully doped Rb_6C_{60} compound with T_h^5 symmetry, calculations [126] show that each of the five-dimensional Raman active H_g modes appearing in the isolated C_{60}

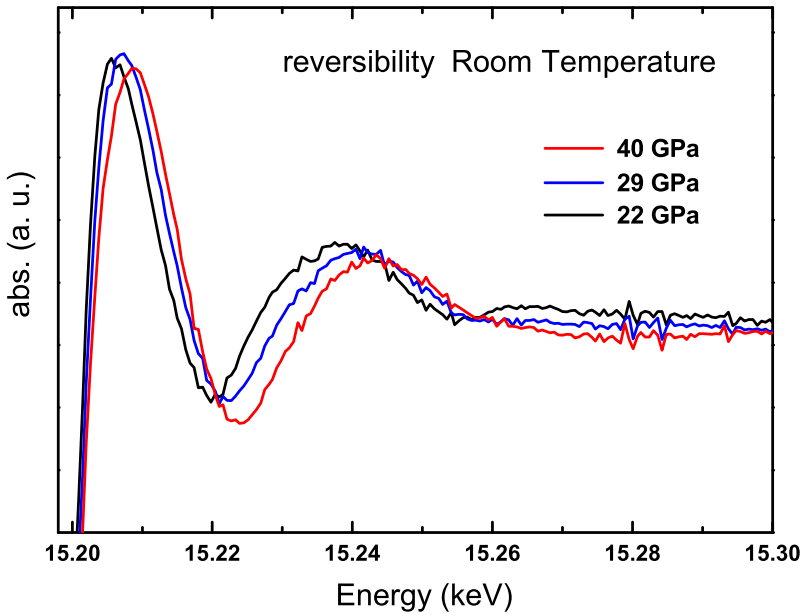

Figure 6.5: *XANES spectra collected at RT during the pressure release of the sample studied at 600 K. Before releasing the pressure we cooled the sample down to RT.*

molecule split into a two dimensional E_g and a three dimensional T_g modes. Moreover, the $3T_{1g}$, $4T_{2g}$ and $6G_g$ modes in the I_h symmetry should become weakly Raman active changing their symmetry into $3T_g$, $4T_g$ and $6(A_g+T_g)$, respectively.

Nevertheless, the Raman spectrum of Rb_6C_{60} measured at ambient pressure and room temperature and previously reported by Zhou *et al.* [129], showed that only ten main modes were Raman active, corresponding to the ten Raman active modes of the isolated molecule with I_h symmetry, i.e. 2 A_g and 8 H_g modes. In addition, they observed that five of the eight H_g modes were split into doublets by a measurable amount, in particular the $H_g(1)$, $H_g(2)$, $H_g(3)$, $H_g(5)$ and $H_g(7)$ modes.

In the present work, the Raman spectrum collected at 0.5 GPa also shows that five of the H_g modes are split into doublets by a measurable amount, in particular $H_g(1)$, $H_g(2)$, $H_g(3)$, $H_g(5)$ and $H_g(7)$ modes, in good agreement with Ref. [129]. In addition, in the present high pressure study, we observe six completely new Raman lines and three additional partners in doublets, corresponding to the $H_g(4)$, $H_g(6)$ and $H_g(8)$ modes, as also observed in our recent Raman study on Cs_6C_{60}. Many other low-frequency Raman active modes of solid Cs_6C_{60} associatedwith ball-ball and ball-alkali metal motions have

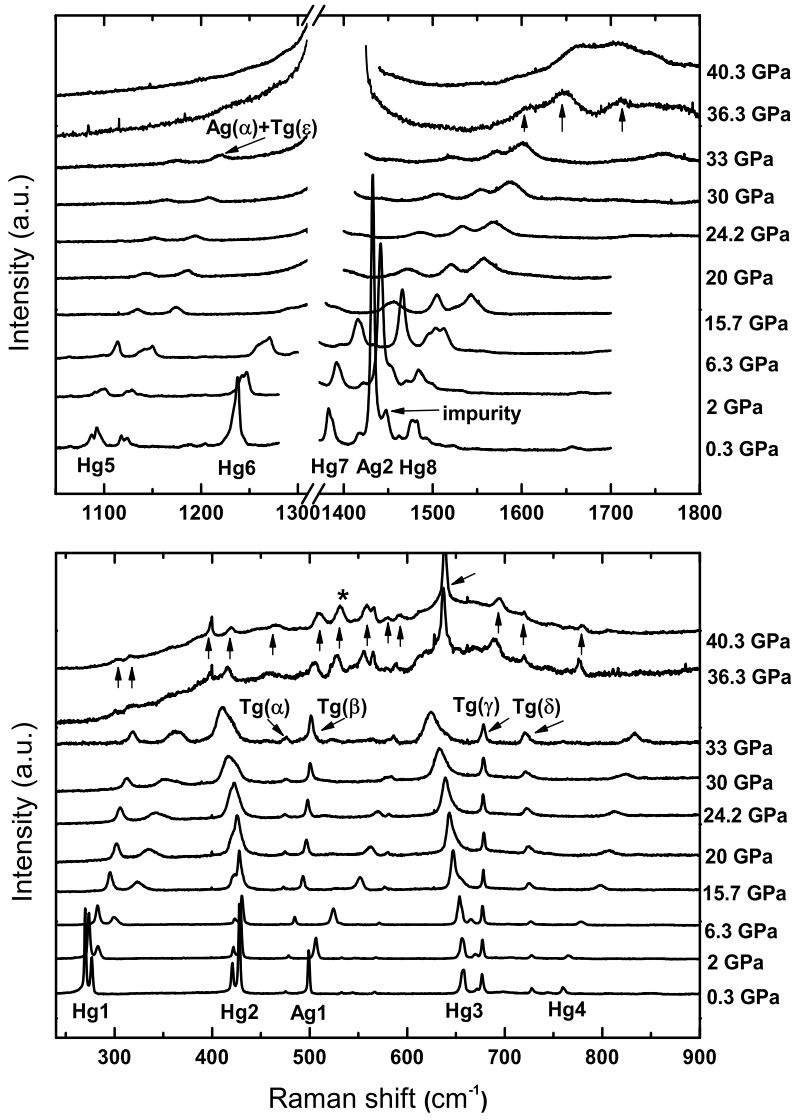

Figure 6.6: *Low-frequency (lower panel) and high-frequency (upper panel) Raman spectra of Rb_6C_{60} at room temperature as functions of pressure. All data are reported without background subtraction. An abrupt change of the Raman spectrum is observed before 36.3 GPa. The mode intensity has been normalized to the $T_g(\gamma)$ intensity for the low-frequency spectra and to the $H_g(8)$ intensity for the high-frequency spectra. After the transition, both the low-frequency and the high-frequency data have been normalized to the intensity of the mode labeled with the '*' symbol.*

been anticipated but they have not yet been observed.

The pressure evolution of the frequencies of all the observed Raman lines is followed with pressure and is shown in Figure 6.6 and Figure 6.7.

In Figure 6.6 we label the previously ten observed intramolecular Raman vibrations as the $2A_g$ and $8H_g$ symmetry modes of the free molecule in order to keep the same nomenclature as used in the past as we did for Cs_6C_{60}. On the other hand, we label the new observed lines with the names of the irreducible representation of the Raman active modes in the Rb_6C_{60} system with T_h^5 symmetry. The symmetry of the six new observed Raman modes has been identified with the help of *ab initio* DFT calculations performed in a way analogous to those reported in section 5.4. They are labelled in Figure 6.6 $T_g(\alpha)$, $T_g(\beta)$, $T_g(\gamma)$, $T_g(\delta)$, $T_g(\epsilon)$ and $A_g(\alpha)$ consistent with their calculated symmetry.

The pressure evolution of the low-frequency and high-frequency Raman modes, up to the highest measured pressure, is shown in Figure 6.7.

The continuous evolution of the observed Raman modes is interrupted by an abrupt change in the modes frequency occurring between 33 and 36.3 GPa. We observe the disappearence of the well known Raman intramolecular modes and the appearence of completely new modes both in the low-frequency and the high-frequency range. This can be reasonably related to an important change in the nature of the intramolecular covalent bondings between carbon atoms. The observed transition is also accompanied by a change of the background displaying an intensity increase having a broadened continuum shape in the frequency range $300< \omega <800$ cm^{-1}. We also collected Raman spectra during the pressure release at 20 and 7 GPa and they are shown in Figure 6.8. These spectra evidenced the reversibility of the observed transition. Also the background was observed to revert to that measured before the transition.

6.6 Discussion

The occurrence of a reversible transition, at around 35 GPa, is observed by XRD and Raman data, at 600 K and room temperature, respectively. The XAS data show that both the local structure and the electronic configuration around each Rb atom, exhibit a progressive and similar change with pressure at both high and room temperature.

A clear reversible first order phase transition has been observed by XRD, at around 35 GPa at 600 K. In correspondance of the transition the unit cell volume has been observed to discontinuously decrease. In particular, from 37.3 43 GPa we found a discontinuity of 24%. Our analysis shows that the new phase is compatible with a hexagonal unit-cell

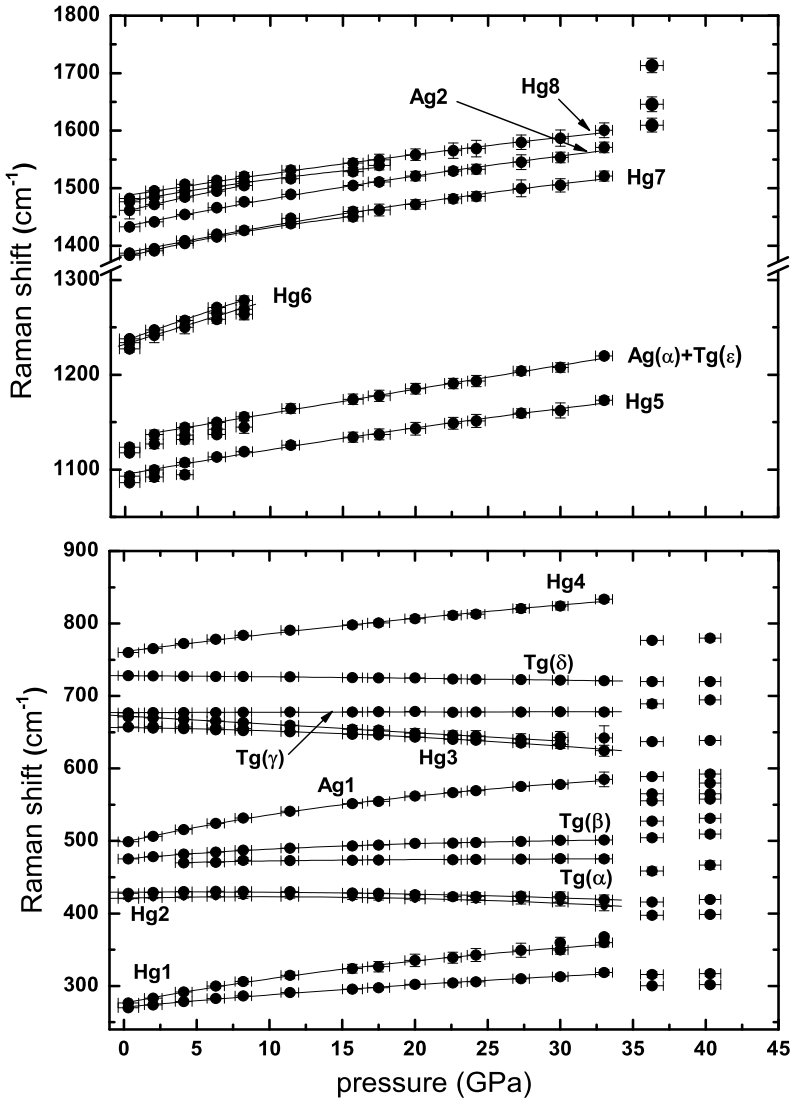

Figure 6.7: *Pressure evolution of the low-frequency (lower panel) and high-frequency (upper panel) Raman modes . The solid lines correspond to least-square fits to a parabolic-type pressure dependence for all modes before the transition at 36.3 GPa. The horizontal bar errors represent the pressure uncertainty estimated from the Lorentzian width of the R1 ruby line; the vertical error bars correspond to the half width at half maximum (HWHM) of each Raman mode.*

structure, with a=8.360(2) Å and c=14.830(7) Å lattice parameters, at 43 GPa and 600 K.

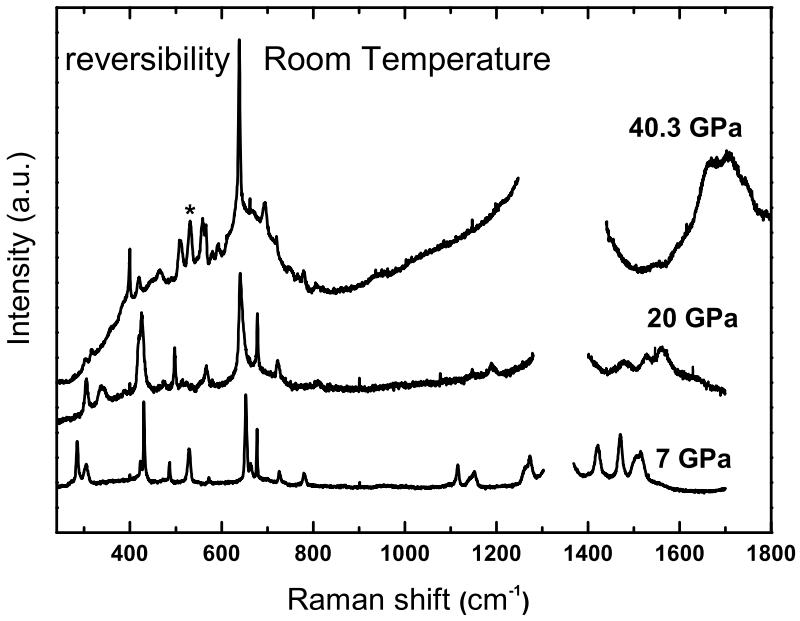

Figure 6.8: *Raman spectra collected at the highest measured pressure, 40.3 GPa, and during the pressure release, at 20 and 7 GPa showing the reversibility of the transition. The data at 20 and 7 GPa reported without background subtraction have been normalized to the intensity of the $T_g(\gamma)$ mode while the spectrum at 40.3 GPa is normalized to the intensity of the '*' mode.*

Since the C_{60} molecules normally occupy the vertices of the unit cell in all the fullerene-based structures, the intermolecular distance in the plane containing the $\overrightarrow{a}$ $\overrightarrow{b}$ unit cell vectors, is compatible with the presence of covalent bonding between these molecules. The C_{60} polymerization has been observed in both solid C_{60} and fullerides with resulting intermolecular distances between the polymerized molecules in the range of [9.09–9.30] Å at ambient conditions [63, 65, 67]. Hence, a possible interpretation of the observed structural change is that the bcc → hexagonal unit-cell symmetry transition, is accompanied by the formation of 2D polymerized C_{60} molecules in the (001) plane of the hexagonal structure. Consequently, in each C_{60}-polymerized plane each molecule could be covalently linked to its six neighbouring molecules, as previously observed by Marques *et al.* [65] for the 2D polymerization of pristine C_{60} encountered in the rhombohedral structure.

The Raman spectroscopy measurements performed at room temperature show the existence of an important and discontinuous change, at around 35 GPa, in the frequency

of the intramolecular normal vibrations.

A possible reason could be the formation of C_{60} polymers, i.e. the formation of covalent bonds between neighbouring molecules as a consequence of their pressure-induced vicinity. In addition, the formation of covalent intermolecular bonds and the concomitant change in the intramolecular C-C bonds, have been previously observed to be responsible for the breaking of icosahedral symmetry of C_{60} molecules in the orthorhombic, tetragonal and rhombohedral structures of polymerized C_{60} [111] leading to a strong change in the Raman spectrum. This explanation is compatible with our XRD experiments suggesting that the origin of the new hexagonal structure is linked to a polymerization process. Also the formation of covalent bonds between the Rb atoms and the C_{60} fullerenes can be envisaged, as recently observed in the Sm_3C_{70} [142] and Eu_3C_{70} [143] fullerides. In these structures, the rare earth metals are observed to bridge two C_{70} molecules, producing C_{70}-Sm-C_{70} dimer structures.

Both XRD and Raman data exhibit an increase of the background intensity after the observed transition probably indicating the presence of disorder in the high pressure structure.

The XRD patterns collected at room temperature show an abrupt width increase of the Bragg reflections above 39.3 GPa preventing us from establishing the nature of the structural changes occurring in that pressure range. Such an increase in the Bragg peaks width, which is more important compared to the high temperature XRD data, could be attributed to the presence of structural strains that build up and cannot relax in absence of high temperature conditions. In addition, a better sample crystallization at 600 K, compared to RT, could be also responsible for the observed difference in the width of the Bragg reflections. The small size of the coherent domains of the high pressure phase formed at RT, could actually cause such huge broadening of the corresponding Bragg reflections. This observation is compatible with the complexity of the polymerization process in fullerenes already observed in pristine C_{60} [20] reinforcing the idea that the observed high pressure hexagonal phase is associated with the formation of C_{60} polymers.

Moreover, the limitation in long-range order crystallization of the high pressure phase in the RT experiment could not affect the changes of local symmetry of the system. This is consistent with the results obtained by Raman spectroscopy and by XAS which are local probes. In addition, since in the Rb_6C_{60} system, the rotation of molecules is hampered by the presence of strong ionic interaction between the alkali atoms and the C_{60} fullerene, a different scenario where different structural phases exist at RT and 600 K appears to be less probable.

The evolution of the XANES spectra between ambient and the highest studied pressure shows the occurrence of a continuous and important evolution of the local structure around each alkali-metal atom. Moreover, the comparison between the progressive modification of the XAS data observed at 600 K and at RT, indicates that the phase transition and the pressure-induced increase of the Bragg reflections width, are accompanied by the same pressure evolution of the local structure and the electronic configuration around each Rb atom. This reinforces our hypothesis of observing the same phase transition at both RT and HT. Nevertheless, the only study performed on the pressure evolution of the XANES signal is not sufficient to understand whether the observed change in the local structure could be associated to a phase transformation.

An important observation concerning the high pressure stability of the Rb_6C_{60} system must be done. The Raman spectroscopy and XRD data, showing the existence of a transition at around 35 GPa, prove the lower pressure stability of the body-centered cubic structure of Rb_6C_{60} compared to the isostructural Cs_6C_{60} compound, where a continuous evolution of the Raman active modes has been observed up to at least 45 GPa [137]. Nevertheless, both fullerides show a much higher pressure stability of the molecular character of the system, compared to the solid C_{60}, which was observed to amorphize at 22 GPa. Subsequently, the fundamental role of the Coulomb interactions on the pressure evolution of the M_6C_{60} systems, can be reasonably assumed. We therefore infer that the presence of such ionic interactions could be responsible for the high pressure stabilization of the C_{60} molecules.

Chapter 7

Structural and electronic evolution with pressure of Rb_6C_{60} and Cs_6C_{60} from first principles

Both the structural and electronic evolution of Rb_6C_{60} and Cs_6C_{60} has been studied by *ab initio* DFT calculations, as a function of pressure, up to around 100 GPa. We observe that while the bcc structure of the Cs_6C_{60} system is stable up to highest calculated pressure, the Rb_6C_{60} system displays an instability of the bcc structure between 75 and 100 GPa.

7.1 Introduction

In chapter 5, by reporting Raman spectroscopy measurements and Raman spectra calculations, we showed the extremely high stability under pressure of the Cs_6C_{60} (around 45 GPa) [137] system compared to pristine C_{60} (around 22 GPa) [46, 47]. This result suggested that the intercalation of Cesium atoms in the C_{60} crystalline structure, allows the preservation the C_{60} molecule up to the maximum studied pressure. On the other hand, in chapter 6, by reporting an experimental pressure study on the Rb_6C_{60} compound under pressure, we showed the occurrence of a phase transition at about 35 GPa, proving that the structural evolution with pressure of the two systems is different.

Nevertheless, since both Rb_6C_{60} and Cs_6C_{60} display a higher pressure stability range compared to solid C_{60} and exhibiting the first fulleride, a higher pressure stability compared to the second one, the importance of the presence of ionic interactions existing in such systems can be deduced.

For these reasons, in the present chapter we explore both the structural and electronic

evolution of Rb_6C_{60} and Cs_6C_{60} under pressure, up to around 100 GPa in order to understand the mechanism taking place during the compression of these structures paying particular attention to the role of the charge transfer from the alkali metal to the C_{60} fullerenes.

7.2 *Ab initio* DFT results

We have performed density functional *ab initio* simulations on Rb_6C_{60} and Cs_6C_{60} under high pressure. More details about the calculation method and the parameters employed can be found in section 4.5.

We studied the structural and electronic evolution of Rb_6C_{60} and Cs_6C_{60} as a function of pressure by decreasing the lattice parameter from the experimental value found at ambient pressure and room temperature (a=11.54 Å and a=11.79 Å) [68] down to 9.55 Å and 10.00 Å, respectively. This corresponds to the pressure ranges [-1.8; 101] GPa for Rb_6C_{60} and [-1.2; 98] GPa for Cs_6C_{60}.

7.2.1 Structural evolution under pressure

In Figure 7.1 we report the pressure evolution of the structural parameters of Rb_6C_{60} and Cs_6C_{60}, as a function of pressure up to around 100 GPa. The study of the pressure evolution of Rb_6C_{60} shows the occurrence of a structural modification between 75 and 100 GPa, implying an abrupt increase of the volume of the C_{60} molecule and a shape-change of the fullerene. On the other hand, a continuous structural evolution of the C_{60} molecule under pressure is obtained in Cs_6C_{60} up to about 100 GPa.

The upper panel of Figure 7.1 reports the calculated volume evolution with pressure of the C_{60} molecule for the two studied systems. In Cs_6C_{60} we observe a continuous decrease with pressure of the fullerene volume up to the highest calculated pressure of 100 GPa. On the onther hand, in the Rb_6C_{60} system, the continuous pressure decrease of the C_{60} volume is interrupted by an abrupt increase of this, between 75 and 100 GPa. This volume increase, indicating the presence of an instability of the bcc phase ("transition"), is accompanied by an abrupt change in the intramolecular C-C bond lengths described in the following.

The pressure evolution of the intramolecular C-C bond lengths for the two calculated systems is shown in the lower panel of Figure 7.1. First of all, we observe that our result at ambient conditions are in good agreement with the previous study of Andreoni *et al.* [69] where they reported that in the doping-induced distorted fullerene in Rb_6C_{60}, the double

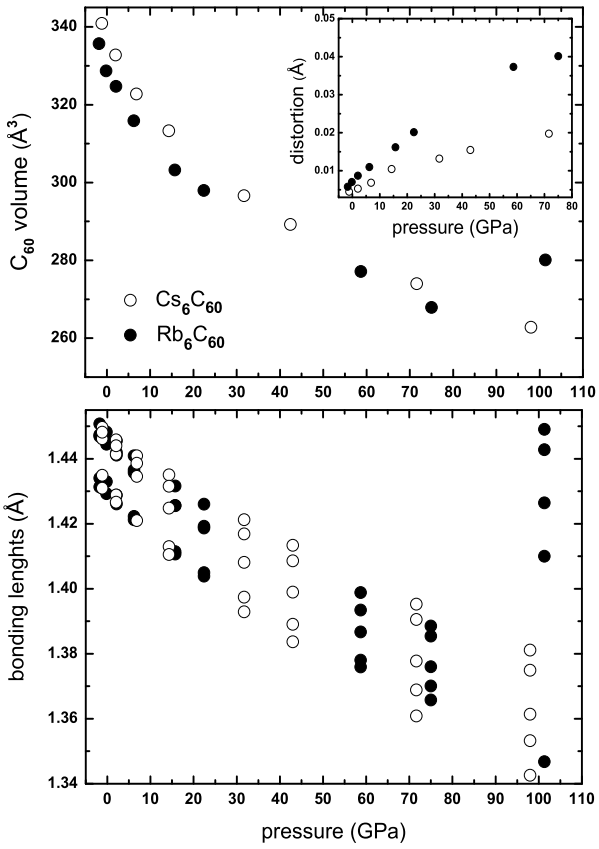

Figure 7.1: *Pressure evolution of the C_{60} molecule in the Rb_6C_{60} system compared to Cs_6C_{60}. The upper panel shows the evolution of the fullerene volume with pressure while the lower panel shows the pressure modification of the single and double bonds. The C_{60} molecule in the Rb_6C_{60} system clearly shows an abrupt structural change before around 100 GPa. The inset in the upper panel displays the pressure evolution of the distortion parameter of C_{60} in the two different systems up to 75 GPa, i.e. before the Rb_6C_{60} transition, where such parameter is no longer well defined.*

and single bonds split into two and three groups respectively, of slightly different lengths. We observe (lower panel of Figure 7.1) that, with increasing pressure, the intramolecular C-C bond lengths decrease while their dispersion increases for both Rb_6C_{60} and Cs_6C_{60}. The only exception is the last pressure point at 100 GPa for Rb_6C_{60} where an abrupt increase of the majority of the C-C bond lengths leads to a volume expansion of the C_{60} molecule. We also observe that the volume increase obtained above 75 GPa in Rb_6C_{60}, concomitant with the abrupt change in the intramolecular C-C bond lengths, is associated with an abrupt shape change of the fullerene described below.

In chapter 4 we reported that the volume of the C_{60} molecule in Rb_6C_{60} and Cs_6C_{60} decreases with pressure up to 15 GPa. We also observed that the volume reduction is accompanied by the increase of the molecular distortion earlier observed at ambient pressure [69] for the molecule in doped Rb_6C_{60} and K_6C_{60} systems compared to the isolated fullerene. In chapter 4 we described this distortion, in terms of a distortion

parameter, d, defined in equation 4.4 and we also calculated it up to 15 GPa.

Here we extend the calculation of the distortion parameter up to around 75 GPa. Its evolution is reported in the upper panel inset of Figure 7.1. The pressure induced distortion is more important in Rb_6C_{60} than in Cs_6C_{60} and it is about 100% higher for Rb than for Cs case, just before the transition, i.e. at around 75 GPa.

We do not report the distortion parameter at 100 GPa, because between 75 and 100 GPa, the observed transition in Rb_6C_{60} is accompanied by a shape change of the C_{60} molecule different from the isolated molecule shape and also from the distorted fullerene found in alkali metal intercalated fullerenes [69, 132] and previosuly discussed (chapters 1 and 4).

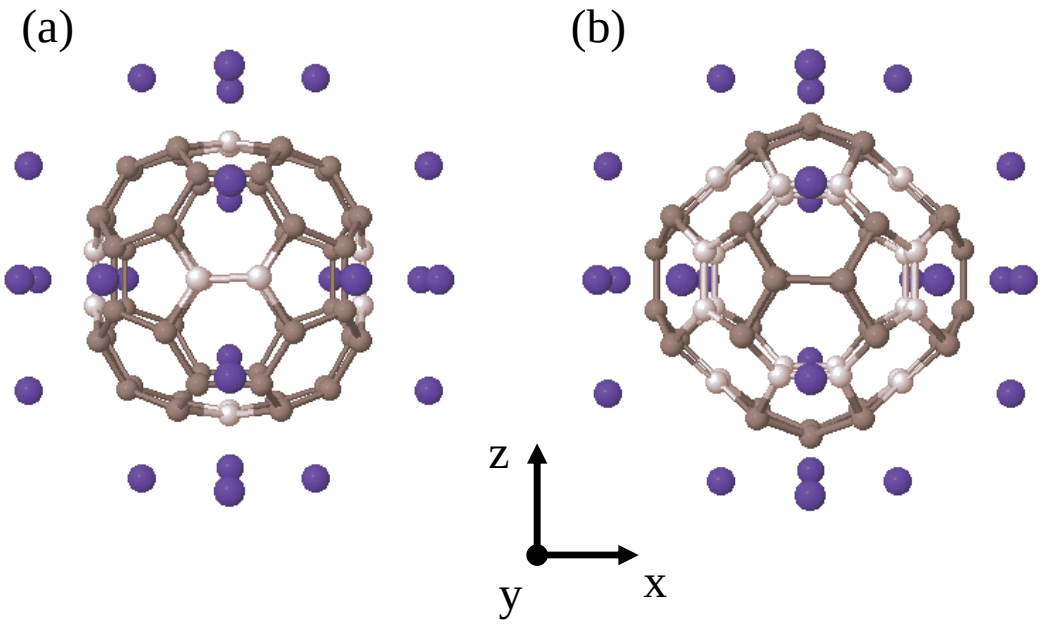

Figure 7.2: *Distortion of the C_{60} molecule. Shape of the fullerene at 100 GPa, after the transition (panel (a)) and at 75 GPa, before the transition (panel (b)). The C atoms placed at ρ_n are depicted in light-grey. In panel (b) the distortion parameter has been amplified by a factor 11 in order to better appreciate it.*

This C_{60} shape, observed in Rb_6C_{60} at 100 GPa, probably does not preserve the cubic T_h symmetry. The Raman calculations performed on the system after the transition display a completely different Raman spectrum compared to that calculated before the transition. Since the Raman spectrum of Rb_6C_{60} is mainly associated with the intremolecular vibrations, this allows us to conclude that the observed transition is accompanied by a change of C_{60} molecule symmetry. Hence the C_{60} shape at 100 GPa cannot be described by the d distortion parameter. In addition, in this case, 12 and 48 carbon atoms in the C_{60}

are at smaller (ρ_n) and larger (ρ_p) distances from the center of the molecule, compared to the 60 atoms average distance ($\rho_{average}$). On the other hand, before the transition they are 36 and 24, respectively, as reported in chapter 4. Moreover, while in this last case, the C atoms of the molecule facing the alkali atoms are placed at ρ_p, after the transition they are found at ρ_n. This difference can be better appreciated by looking at Figure 7.2, where we report the fullerene, after and before the transition, surrounded by the 24 alkali metal atoms placed at the tetrahedral sites on the 6 bcc cell faces. The C atoms placed at ρ_n are depicted in light-grey color and they are 12 and 36, after and before the transition, respectively. Those placed at ρ_p are depicted in dark-grey color.

7.2.2 Electronic evolution under pressure

We have studied the electronic structure evolution with pressure of Rb_6C_{60} compared to Cs_6C_{60}. The calculated electronic band structure for both systems, shown in Figure 7.3, is in good agreement with that previously reported for the isostructural K_6C_{60} [70]. Both Rb_6C_{60} and Cs_6C_{60} are insulators at low pressure with the t_{1u} three-fold degenerate state completely occupied and the gap between the highest occupied and lowest unoccupied band is of 0.63 eV and 0.66 eV, respectively.

We obtain a progressive closure of the gap as a function of pressure for both systems resulting from the bandwidth broadening consistent with the increase in density (Figure 7.4). Metallization is observed at about $\sim$ 20 GPa for Rb_6C_{60} and $\sim$ 40 GPa for Cs_6C_{60}. The metallic phase is interrupted in Rb_6C_{60} by a clear opening of the gap between 75 and 100 GPa, contrary to the case of Cs_6C_{60}. At 100 GPa the gap is 1.41 eV, much higher that the initial value (0.63 eV). This pressure-induced metal-insulator transition together with the discontinuity in the structural evolution with pressure observed in Rb_6C_{60} reflects the *occurrence of an instability of the bcc structure under pressure*. Since our calculations are done under restriction on the unit cell symmetry, such a transition cannot be accompanied by a symmetry change of the unit cell, leading therefore to fictitious results concerning the new phase observed at 100 GPa, such as the fullerene shape. On the other hand, the different pressure behavior of the electronic band structure in Cs_6C_{60} reflects a higher pressure range of stability for this system compared to Rb_6C_{60}.

In order to study the pressure evolution of the charge transfer from the alkali Cs atom to the fullerene, we analyzed the data in two differents ways. We firstly studied the evolution of the Mulliken-population of the molecule as a function of pressure which directly gives information about the transfer of charge from the alkali metal atoms to the molecule. Nevertheless, this method shows different inconveniences, related not only to the strong

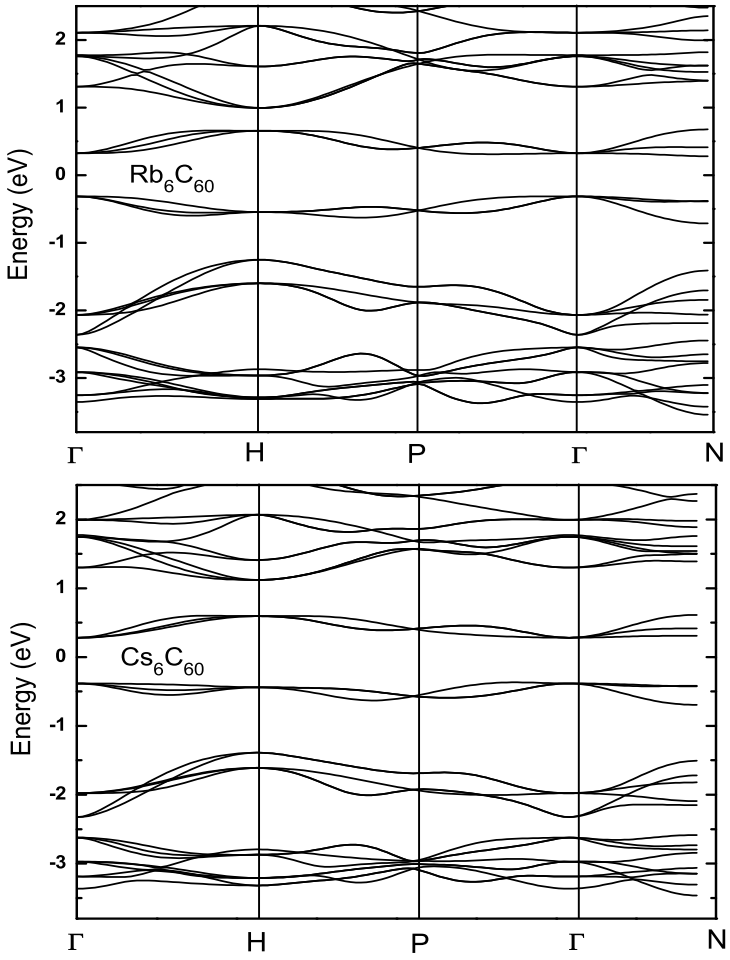

Figure 7.3: *Calculated electronic band structure of Rb_6C_{60} (upper panel) (a=11.54 Å) and Cs_6C_{60} (a=11.79 Å) (lower panel). The energy of the Fermi level is set to zero eV.*

dependence of the results on the calculation parameters, (basis set, pseudopotentials, etc.) but also on the arbitrary way of establishing which electrons belong to each atom. In particular, within this method, the attribution of electrons to the different atoms becomes complicated when the overlap of orbitals belonging to different atoms occurs. In the present study, the pressure induced vicinity of the alkali atoms to the molecules could worsen such inconvenience. For this reason, we also studied the evolution of the charge transfer from the alkali Cs atom to the fullerene, by studying the evolution of the electronic density inside the C_{60} molecules.

The Mulliken-population analysis shows that in the Rb_6C_{60} system with lattice pa-

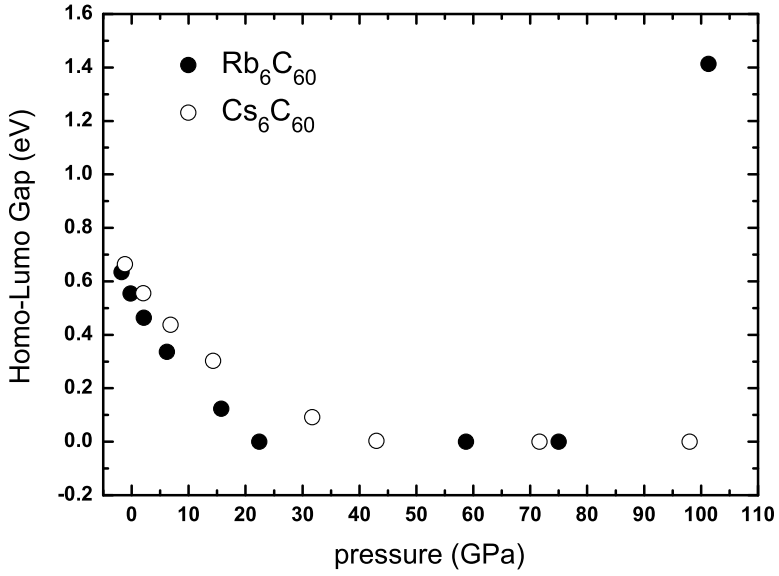

Figure 7.4: *Pressure evolution of the gap, between the highest occupied and lowest unoccupied band, as a function of pressure for both system up to 100 GPa. An abrupt gap opening is observed in Rb_6C_{60} between 75 and 100 GPa.*

rameter equal to 11.54 Å (i.e. corresponding to the ambient cell parameter obtained experimentally at room temperature) the interactions between each molecule and the alkali metal atoms are ionic. As there are six Rb atoms per molecule, their complete ionization and equipartitioning of this charge would correspond to a total charge on each inequivalent C atoms equal to 4.1 (each C atoms has 4 valence electrons). We instead obtain Q=4.052 and 4.013, for the 12 equivalent C atoms in the 24*g* site and for the remaining 48 C atoms in the two non equivalent 48h sites, respectively[1], meaning that an incomplete transfer of the Rb 5*s* electron is taking place. For the Cs_6C_{60} system studied at 11.79 Å (lattice parameter corresponding to the ambient conditions phase) we obtain Q=4.053 and 4.018, respectively.

Nevertheless, as mentioned above, the value of charge obtained for each atom through this method could be misleading. For this reason, we focus on the variation of the Mulliken-population, $\Delta Q_{mulliken}$, of C_{60} as a function of pressure with respect to the value obtained at low pressure (i.e. -1.2 and -1.8 GPa, for Cs_6C_{60} and Rb_6C_{60}, respectively). The results, reported in Figure 7.5, show a progressive decrease of the electronic charge transfer from

[1] We remind here that in the unit cell, there are three non equivalent sites for the C atoms and they are 24g, 48*h* and 48*h*.

the alkali metals to the molecule with pressure in both Rb_6C_{60} and Cs_6C_{60}, and a faster decrease in the Rb case with respect to Cs is also observed. In particular, the $\Delta Q_{mulliken}$ between the Mulliken-population calculated around 75 GPa and the initial one is -3.6 and -3.0 e^- for Rb_6C_{60} and Cs_6C_{60}, respectively. When considering 100 GPa, these values become -5.8 and -3.5 e^-, respectively. In addition, a discontinuity in the Mulliken-population of the C_{60} is observed in Rb_6C_{60} between 75 and 100 GPa. Hence, from our population analysis, in correspondance of the phase transition, the transfer of charge from the Rb atoms to the molecule abruptly decreases.

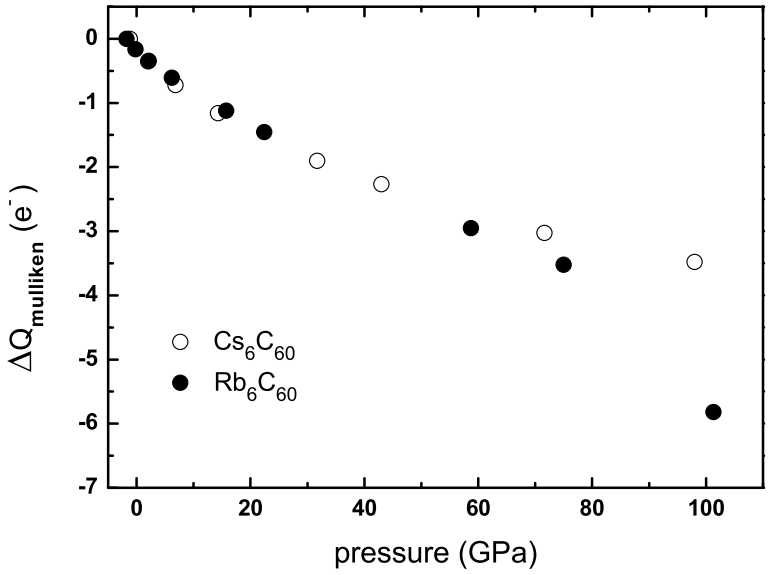

Figure 7.5: *Pressure variation of the Mulliken-population of each C_{60} molecule, $\Delta Q_{mulliken}$, as a function of pressure for both systems. A discontinuity is observed for the Rb_6C_{60} system between 75 and 100 GPa.*

The second analysis method is an indirect way of studying the electronic charge transfer to fullerenes. It consists in calculating the electronic density inside the C_{60} molecules. Being the fullerene a closed molecule we can say, in principle, that the electronic density into the molecule actually belongs to the molecule, differently to the population analysis method, as discussed above. In addition, the variation of such quantity is proportional to variations of the transferred charge from the alkali metals to the fullerenes. We define now the electronic density, ρ, as the difference between the electronic density inside each molecule ρ_m of the two M_6C_{60} systems and the total homogeneous electronic density ρ_t

in the M_6C_{60} systems, in particular:

$$\rho = \left[\left(\frac{Q}{V}\right)_m - \left(\frac{Q}{V}\right)_t\right] = \rho_m - \rho_t \tag{7.1}$$

In this way, by subtracting the total homogeneous electronic density ρ_t, from the molecule-enclosed electronic density ρ_m, we indirectly consider the contribution of the charge tranfer from to alkali metal to the molecule since the number of electrons of the C atoms in principle does not vary, a part from those transferred by the alkali atoms. Hence, the evolution of this difference is proportional to the evolution of the electronic charge transferred to each fullerene.

In Figure 7.6 we report the pressure evolution of the following electronic quantities: i) the number of electrons Q_m inside the C_{60} molecule (upper-left panel), ii) the electronic density ρ_m inside the molecule (upper-right panel), iii) the total homogeneus electronic density ρ_t obtained by considering the valence electrons inside the unit cell (lower-left panel) and iv) the difference between ρ_m and ρ_t (lower-right panel). The Q_m quantity shows a pressure increase in both systems, exhibiting an abrupt increase in correpondance of the Rb_6C_{60} transition, between 75 and 100 GPa. The ρ_t density clearly increases as a function of pressure in the two compounds since the number of valence electrons remains constant during the compression (564=120 C atoms × 4 (2s+2p) + 12 alkali atoms × 7 (6p+1s)) while the unit cell volume decreases. The ρ_m density exhibits a similar continuous increase as a function of pressure for the two systems up to 100 GPa and no discontinuities are observed in Rb_6C_{60}. Nevertheless, as discussed above, in order to have information about the evolution of the charge transfer from the alkali metals to the C_{60} we consider the evolution of the ρ density defined in eq. 7.1.

We observe that ρ decreases with pressure for both systems and the slope of the linear fit performed up to around 75 GPa is 170% higher for Rb_6C_{60} compared to Cs_6C_{60}. As a consequence, the charge transfer from the alkali metal decreases as a function of pressure for both systems and more rapidly in Rb_6C_{60} than in Cs_6C_{60} as also obtained from the Mulliken-population analysis. In addition, above 75 GPa, a discontinuity leading to an abrupt decrease of the ρ density is observed consistent with the result obtained by the Mulliken-population analysis.

In order to better understand the electronic evolution of both systems under pressure we studied the density of states (PDOS) projected onto the electronic states of the alkali metal and of carbon atoms. This allows us to understand which is the contribution of the different atoms to the DOS. In Figures 7.7 and 7.8 we display the electronic band structure and the corresponding PDOS (on both C and alkali atom orbitals) calculated for Rb_6C_{60}

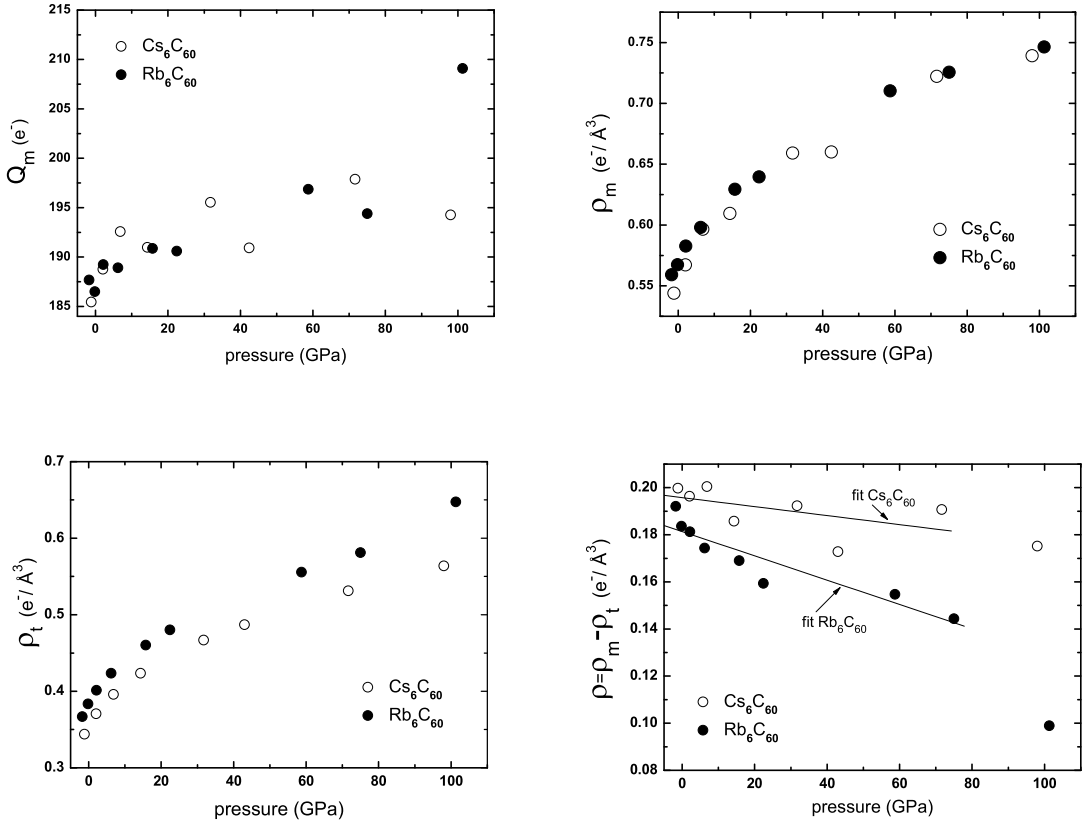

Figure 7.6: *Electronic evolution as a function of pressure in Rb_6C_{60} and Cs_6C_{60}. It displays the pressure evolution of: number of electrons Q_m inside the C_{60} molecule (upper-left panel); the electronic charge density ρ_m contained in each C_{60} molecule (upper-right panel); the electronic homogeneous charge density ρ_t within the bcc unit cell (lower-left panel) and the ρ density (lower-right panel) giving information about the evolution of the charge transfer from the alkali atoms to the molecule. In the last panel we report the curves resulting from the linear fit to the pressure evolution of ρ, performed up to 75 GPa for both systems. The lower slope of the linear fit curve obtained for Rb_6C_{60} indicates that the electronic charge transferred to the molecule decreases faster with pressure in Rb_6C_{60} compared to Cs_6C_{60}.*

and Cs_6C_{60} respectively, in the energy range [-3.5:2.5] eV at three different pressure values. The Fermi energy has been set to zero for clarity. In both pictures we report the electronic band structure and the corresponding PDOS calculated at similar pressure values in order to better compare the results obtained for the two different systems.

The study of the PDOS clearly shows that, at all pressure values, the contribution of the C states to the DOS around the Fermi level is predominant compared to the alkali

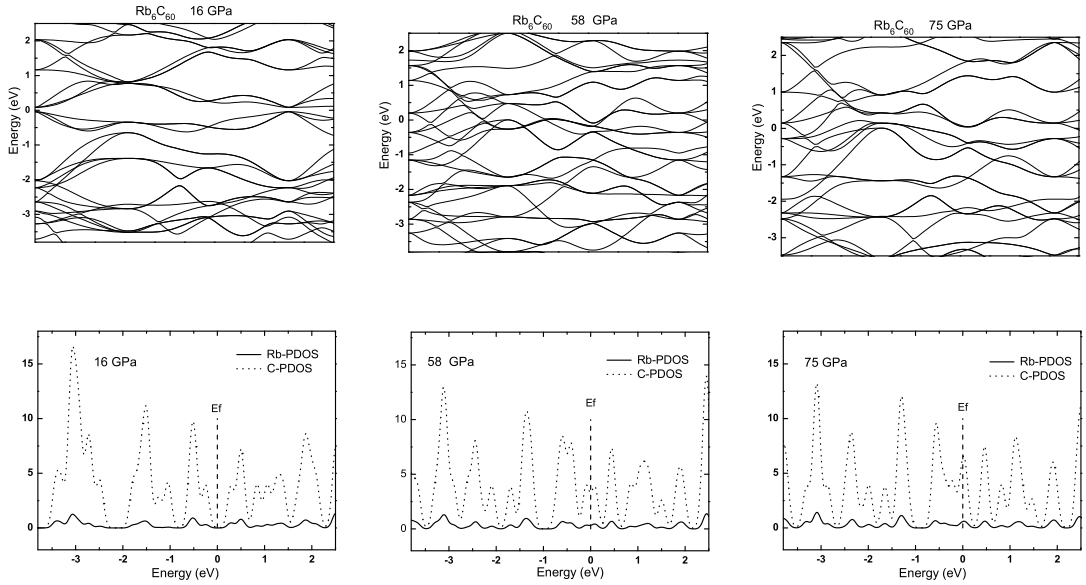

Figure 7.7: *The upper panels display the electronic band structure of Rb_6C_{60} calculated for the three different pressure values 16, 58 and 75 GPa (from left to right), around the Fermi level. The lower panel shows the corresponding PDOS on the Rb and C basis orbitals (Rb-PDOS and C-PDOS). In all pictures the Fermi level is set to zero.*

metal atoms. This also demonstrates that for all studied pressure points, the 5*s* and 6*s* electrons (of Rb and Cs atoms respectively) are transferred to the C_{60} molecule. Since the pressure evolution of the PDOS does not exhibit any change implying an increase of the alkali atoms contribution to the DOS, these *s* electrons seem to belong to the fullerene even at high pressure, although a pressure decrease of the charge transfer is observed.

Figures 7.7 and 7.8 also show the progressive metallization of the system under pressure, as previously reported in Figure 7.4. Nevertheless, a different electronic behavior is observed for the two systems as a function of pressure. We observe that in the Cs_6C_{60} system, the value of the PDOS on both Cs and C atoms is considerably smallerThis difference together with the different strutural behavior observed under pressure, allows to conclude that the intercalation of fullerenes with heavy alkali metal atoms, gives rise to systems whose pressure evolution is strongly affected by the particular type of alkali atom.

than for Rb_6C_{60} at the Fermi level, once the metallization has occurred. In particular, by comparing the PDOS computed at 58 GPa for the Rb case and that computed at 45 GPa for the Cs case, we find that the value of the C-PDOS (PDOS on C states) at the Fermi energy is 300% higher for Rb_6C_{60} compared to Cs_6C_{60}. When considering the PDOS computed at higher pressure, i.e. at 75 and 72 GPa for the Rb and Cs cases respectively, we obtain a C-PDOS about 600% higher for Rb_6C_{60} compared to Cs_6C_{60}.

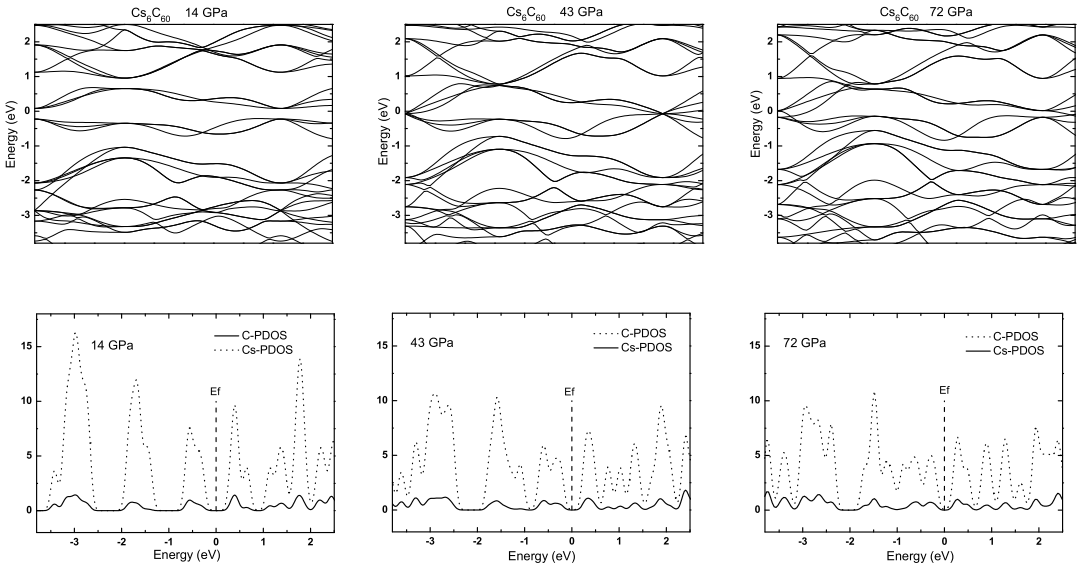

Figure 7.8: *The upper panels display the electronic band structure of Cs_6C_{60} calculated for the three different pressure values 14, 43 and 72 GPa (from left to right), around the Fermi level. The lower panel shows the corresponding PDOS on the Cs and C orbitals (Cs-PDOS and C-PDOS). In all pictures the Fermi level is set to zero.*

This difference together with the different structural behavior observed under pressure, allows us to conclude that the intercalation of fullerenes with heavy alkali metal atoms, gives rise to systems whose pressure evolution is strongly affected by the particular type of alkali atom.

7.3 Discussion

The results show the exsistence of a pressure instability of the bcc structure of Rb_6C_{60}, between 75 and 100 GPa, contrary to the case of Cs_6C_{60} where a continuous structural and electronic evolution with pressure has been observed up to around 100 GPa. We observe a discontinuous modification of the single and double C-C intramolecular bond lengths of the C_{60} volume in correspondance of the "transition" reported in Rb_6C_{60}. We also observe an abrupt opening of the gap between the highest occupied and the lowest unoccupied bands and a discontinuity in the descrease of the charge transfer from the alkali Rb atoms to the molecules.

We also studied the evolution of the charge transfer from the alkali metal ions to the fullerenes by using two different methods, the Mulliken-population analysis and the study of the electronic density inside the C_{60} molecule. Both methods show that the

charge transfer continuously decreases as a function of pressure for both systems, but this decrease is observed to be less pronounced in Cs_6C_{60}, compared to the Rb case. At the same time, the pressure induced distortion of the fullerenes increases less rapidly than in Rb_6C_{60}. In particular, the distortion parameter is 100% higher for the Rb case than in the Cs one right before the transition, i.e. at around 75 GPa.

The progressive distortion of the C_{60} molecules as a function of pressure occurs together with a progressive decrease of the charge transfer from the alkali metal atoms to the molecules, in both systems. These considerations, together with the higher pressure stability of Cs_6C_{60} compared to Rb_6C_{60} [137], experimentally observed by Raman spectroscopy measurements, suggest that the charge transfer and hence, the ionic interactions between the positively charged alkali ions and the negatively charged C_{60} molecule, which decreases slower with pressure in the Cs case compared to the Rb case, contribute to stabilize the C_{60} molecule in these structures. This can also explain the higher pressure stability of these compounds, compared to pristine C_{60} [46, 47].

Information concerning the symmetry of the new Rb_6C_{60} structure, stable above 75 GPa, cannot be derived from our calculations because the bcc unit cell symmetry has been imposed for all pressure points.

Chapter 8

Role of charge transfer on fullerene polymerization

8.1 Introduction

In this chapter, we firstly present XRD measurements performed on Rb_6C_{60} and Cs_6C_{60} at around 5 GPa as a function of temperature. The reason we explored this P-T range lies in the attempt to form C_{60} polymers. In fact, at this pressure the distance between the nearest neighbouring molecules in these systems is the same as that in solid fcc C_{60} where polymerization, at high temperature, has been observed. Since in our measurements we do not observe any phase transition leading to the polymerization of the molecules, we deduce that the presence of the Rb and Cs alkali metals and therefore of the charge transfer to the molecules, should play an important role in the formation of covalent bonds between the C_{60}s. In addition, the C_{60} polymerization has been experimentally observed at ambient conditions, as discussed in chapter 1, in fullerides with light alkali metals (like Na_2RbC_{60} and Li_4C_{60}) or with a low stoichiometric amount of heavy alkali metals (i.e. MC_{60}, M=K, Rb and Cs). Contrary to the systems studied in this work, in these compounds, the presence of ionic interactions seems to favor the formation of covalent bonds between the molecules. Hence, in fullerides with heavy alkali metals, the stoichiometric amount of the ions in the system and consequently, the Coulomb interactions between the positively charged alkali ions and the negatively charged C_{60} molecule appears to be a critical parameter for the formation of C_{60} polymers.

For this reason we performed *ab initio* DFT calculations on a very simple system consisting of 1D C_{60} chains, in order to understand if the presence of a transfer of charge to the molecule, in this simple structure, could affect polymerization. The results of the

calculations are presented and discussed in this chapter.

8.2 XRD measurements

XRD measurements have been performed on Rb_6C_{60} and Cs_6C_{60} under high pressure (HP) and high temperature (HT) conditions by using the Paris-Edinburgh (PE) cell device. The experimental details concerning: i) the quality of the samples; ii) the HP-HT cell assembly and iii) the set-up of beamline ID27, can be found in chapter 4.

Pressure and temperature are calibrated using the cross-calibration method (explained in chapter 3) and for this purpose the Vinet [84, 85] equation of state of NaCl and MgO have been used.

XRD patterns have been collected as a function of temperature by keeping the PE oil delivery constant to 70 bar. As a consequence of the B-epoxy gasket softening and expansion due to HT conditions, the *in situ* pressure is observed to decrease when increasing temperature. In Figure 8.1 the evolution of the XRD patterns as a function of temperature at a constant oil delivery is reported for both samples. In particular, XRD patterns for both increasing and decreasing temperature are reported in the same panel (Figure 8.1). For both Cs_6C_{60} and Rb_6C_{60}, the disappearence of the Bragg reflections belonging to the sample is observed, starting at 5.1 GPa and 900 K and 5 GPa and 1310 K, respectively. Only those of the HP-HT cell assembly remain observable up to the highest measured temperature. When decreasing the temperature, by keeping again the PE oil delivery constant to 70 bar, the sample does not revert to the pristine bcc structural phase in either systems. The transition is accompanied by an important increase of the background intensity in both cases, probably due to the presence of disordered or amorphous structures. While the Rb_6C_{60} background displays a broaden continuum after the transition, the Cs_6C_{60} one exhibits two broad peaks at around 5 and 7 deg. After normalizing the data to the acquisition time we observed that the $I_{MgO(200)}/I_{bkg}$ value (i.e. the ratio between the intensity of the MgO(200) reflection and the intensity of the background) increases about 350% for Cs_6C_{60} after the HT-HP treatment compared to the $I_{MgO(200)}/I_bkg$ value obtained at ambient conditions before the HT-HP treatment. For Rb_6C_{60}, we considered the intensity of the Re(101) reflection and the value of the $I_{Re(101)}/I_{bkg}$ ratio on the recovered sample increases of 400% compared to the value obtained at ambient conditions before the HT-HP treatment.

Subsequently, XRD measurements have been performed on the two recovered samples at room temperature and ambient pressure, after the HP-HT treatment. A comparison

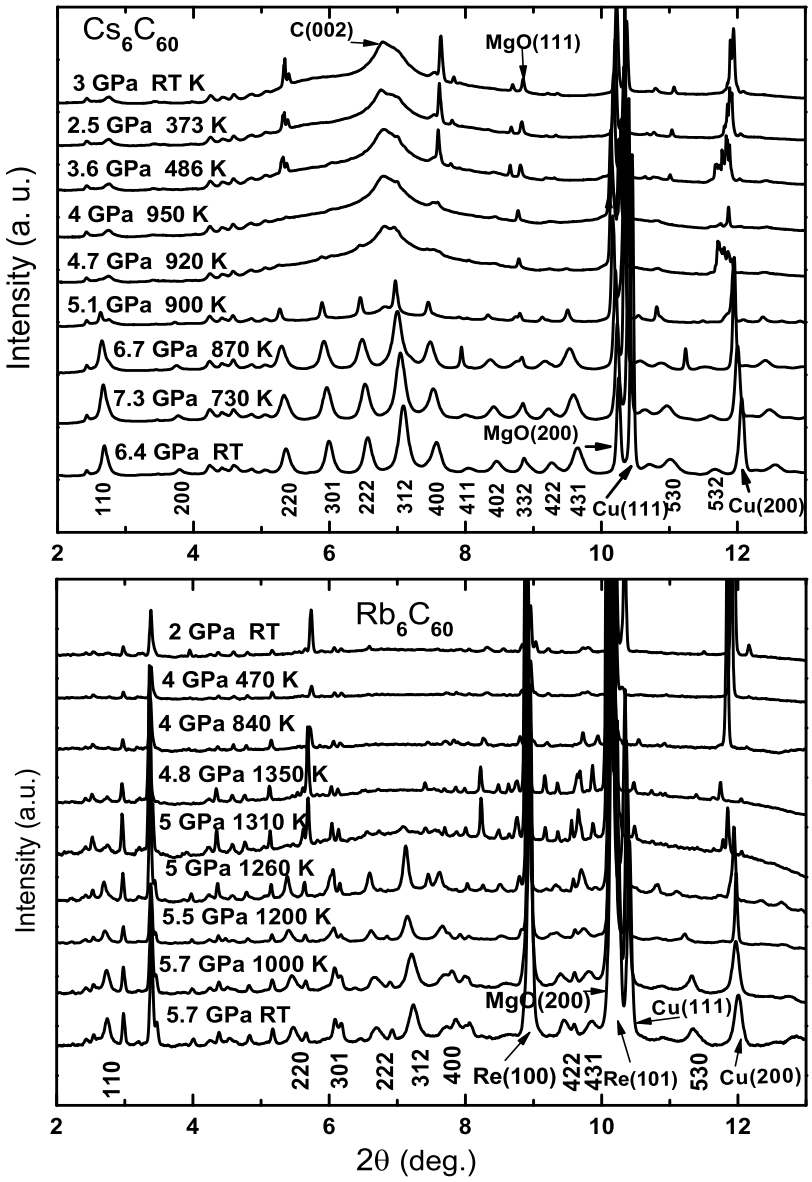

Figure 8.1: *Temperature evolution of the XRD pattern of Cs_6C_{60} (upper panel) and Rb_6C_{60} (lower panel) from room temperature (RT) up to 950 and 1350 K respectively. Data have been normalized to the intensity of the MgO(200) reflection. Labels denote the main Bragg peaks as well as reflections originating from the sample environment. 'Cu' stands for the CuBe alloy capsule. The attenuation and then the disappearence of the sample Bragg reflections is observed starting at 900 and 1310 K for Cs_6C_{60} and Rb_6C_{60} respectively.*

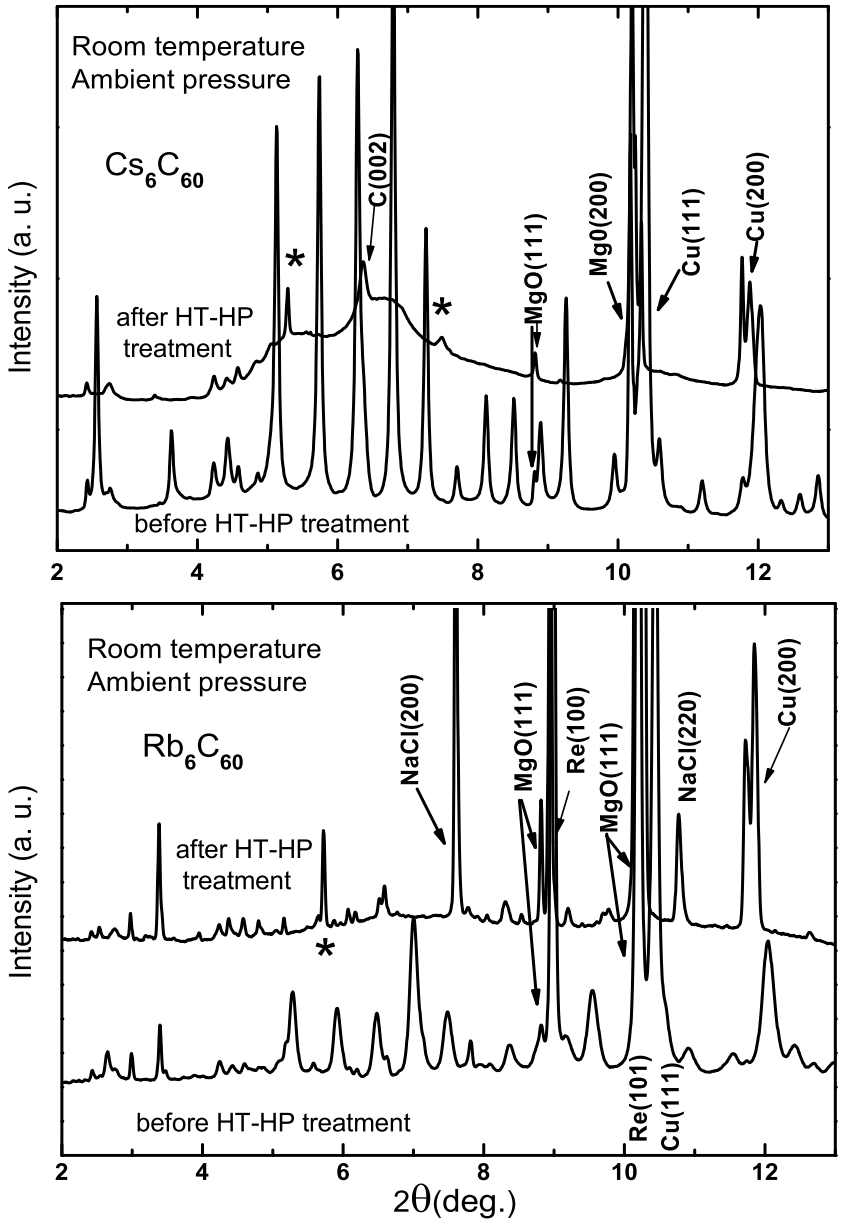

Figure 8.2: *XRD patterns of Cs_6C_{60} and Rb_6C_{60} collected at ambient pressure and room temperature after the HP-HT treatment. They are compared to the XRD data performed at ambient conditions before the HT-HP study. We can observe that the transition is irreversible in both systems. The '*' symbol indicate the Bragg reflections observed after the HT-HP treatment. Data are normalized to the background.*

between the patterns collected before and after the treatment is shown in Figure 8.2. The transformation of the sample, associated to the disappearence of the bcc phase Bragg reflections, appear to be irreversible in both cases. This transition can be clearly assigned to the amorphization of the systems as no Bragg reflections, indicating the presence of a crystalline phase, are observed. However, the Cs_6C_{60} and Rb_6C_{60} XRD data collected at ambient conditions after the HP-HT treatment exhibit some un-assigned reflections, indicated in Figure 8.2 with the '*' symbol. This could derive from the reaction, at HT, of the CuBe alloy with some element in contact with it, as its structural phase does not completely revert to the initial one. In addition, a reaction of the Cs_6C_{60} and Rb_6C_{60} compounds with the CuBe can also be envisaged.

8.3 Raman measurements

We measured the two recovered samples, after the HT-HP treatment, by Raman scattering in order to get additional information about the transformed systems. The Cs_6C_{60} sample was taken out from the the gasket in contact with air. We could retrieve the cylinder containing all the HT-HP cell components and we looked at it using an optical microscope. The different parts of the HP cell environment were not clearly recognizable at the microscope. The Raman measurements for this recovered sample were performed in contact with air.

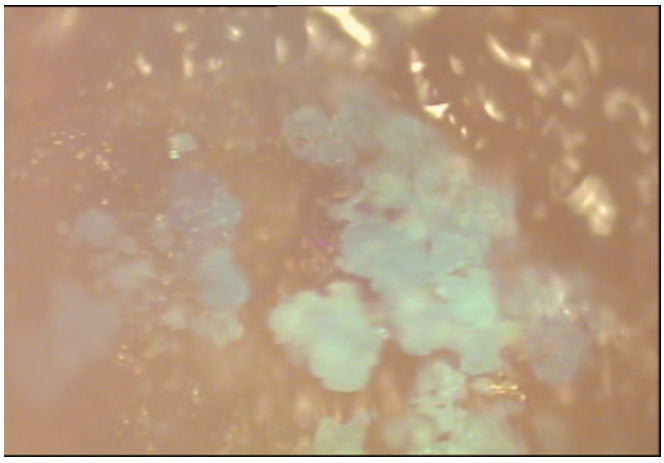

Figure 8.3: *Picture of the HP cell containing the Cs_6C_{60} sample, collected after the HT-HP treatment. The sky-blue color probably derives from Cu oxides.*

A picture of the HP cell containing the Cs_6C_{60} sample, after the HT-HP treatment, is shown in Figure 8.3. The sky-blue color probably derives from Cu oxides. The Raman measurements performed on different parts of the recovered sample are reported in

Figure 8.4.

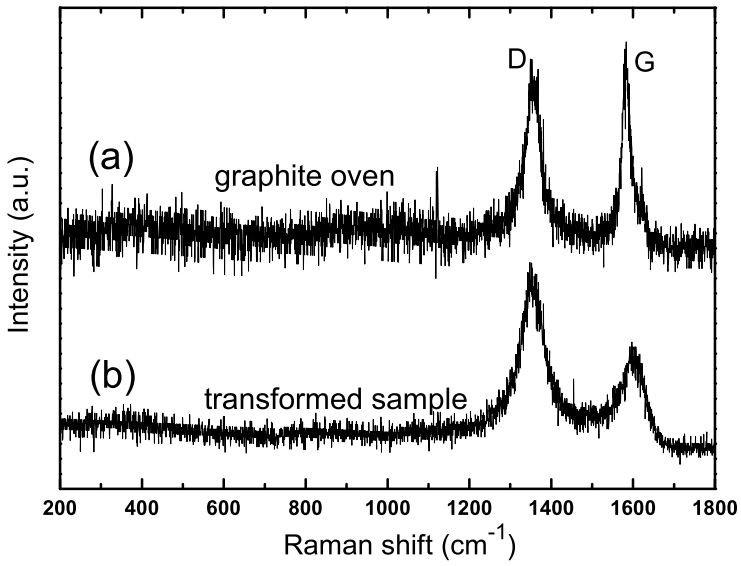

Figure 8.4: *Raman spectra collected on the Cs_6C_{60} sample after the HT-HP treatment. Spectrum a) was collected at the extremity of the HP cell where the graphite furnace should be present. Spectrum b) was instead collected in the center of the HP cell, corresponding to the transformed Cs_6C_{60} compound.*

The data show two bands corresponding to the *G* and *D* Raman lines of graphite. The *G*-line (graphite line) is localized at around 1600 cm^{-1} and a *D*-line (disordered graphite line) in the vicinity of 1350 cm^{-1}. The *G*-line has E_{2g} symmetry and its eigenvectors (shown in Figure 8.5) involve the in-plane bond-stretching of pairs of carbon sp^2 atoms. The *D* peak is a breathing mode of A_{1g} symmetry and is forbidden in perfect graphite; it only becomes active in presence of disorder.

The spectra reported in Figure 8.4 were collected in different zones of the sample, in particular in the center and in the extremity of the cylinder. Spectrum (*a*), collected at the extremity of the HP cell, shows a more intense *G*-line compared to the D-line and the I_D/T_G ratio is 0.8. On the other hand, spectrum (*b*), collected in the center of the sample displays a higher intensity of the *D* disorder peak with respect to the *G* graphite line. The I_D/T_G ratio is 1.7.

The higher value of the I_D/T_G found in the center of the HP cell compared to the extremity can be interpreted as follows. The extremity of the HP cell should in principle

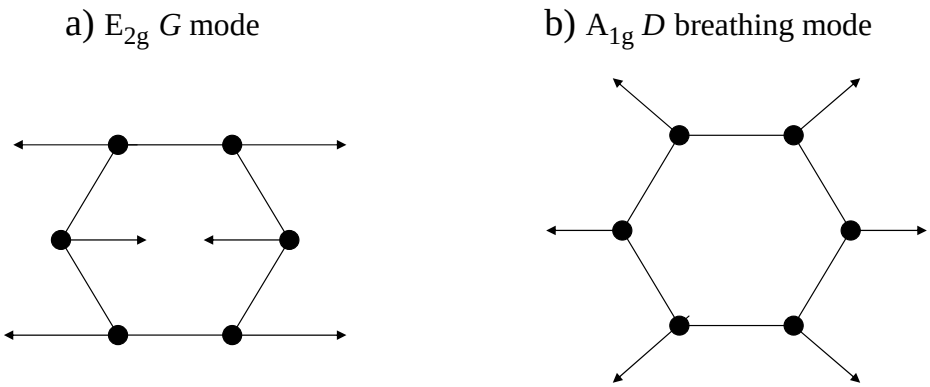

Figure 8.5: *Carbon motion in a) G and b) D modes.*

contain graphite, coming from the graphite furnace, while in the center the Raman spectrum should correspond to the transformed sample as only Cs_6C_{60} powder was placed in that zone.

As a consequence, we suggest that the Cs_6C_{60} compound irreversibly transformed into graphite displying a higher level of disorder compared to the graphite deriving from the furnace. Nevertheless, we cannot exclude the possibility of an air- or humidity- induced contamination of the sample as both manipulation and data collection were performed in contact with air.

The Raman spectra collected on the Rb_6C_{60} sample after the HP-HT treatment showed that, at least a part of it, irreversibly transformed into diamond as an intense line was observed at 1332 cm^{-1}, corresponding to the main diamond mode frequency. Unfortunately, after the measurements, the spectra were lost preventing an accurate study and hence a further discussion in this thesis. This deserves further studies in order to clarify this point as 5 GPa and $\sim$ 1300 K constitute relatively "low" thermodynamic conditions for the diamond synthesis.

8.3.1 Discussion

By coupling the results obtained from the XRD and Raman data reported in the previous sections, we can conclude that the Cs_6C_{60} and Rb_6C_{60} compounds, after a study performed at 5 GPa at high temperature, irreversibly transform into graphite and diamond, respectively, where the C_{60} molecules are no longer present. This result is quite interesting if we compare it with the behavior of the C_{60} molecules in solid C_{60}, in the same range of pressure and temperature explored for our systems. In fact, in the first chapter, when describing the phase transitions observed in solid C_{60}, we reported that between 1 and 8 GPa, around 600 K, polymerization of the molecules takes place. Nevertheless,

being both the compressibility and the dependence of nearest-neighbouring intermolecular distance from the lattice parameter different in the M_6C_{60} systems and in the fullerite[1], the real C_{60}-C_{60} distance, and not the P-T range, must be considered in order to make a meaningful comparison.

In the case of pristine C_{60}, 1D and 2D polymerization was observed (see chapter 1) between 1 and 8 GPa around 600 K, meaning that at this temperature, when the centres of the nearest molecules are at distances between 9.85 and 9.30 Å, respectively, a first order transition occurs leading to new structures (orthorhombic, tetragonal or rhombohedral) where covalent bonds between molecules are formed.

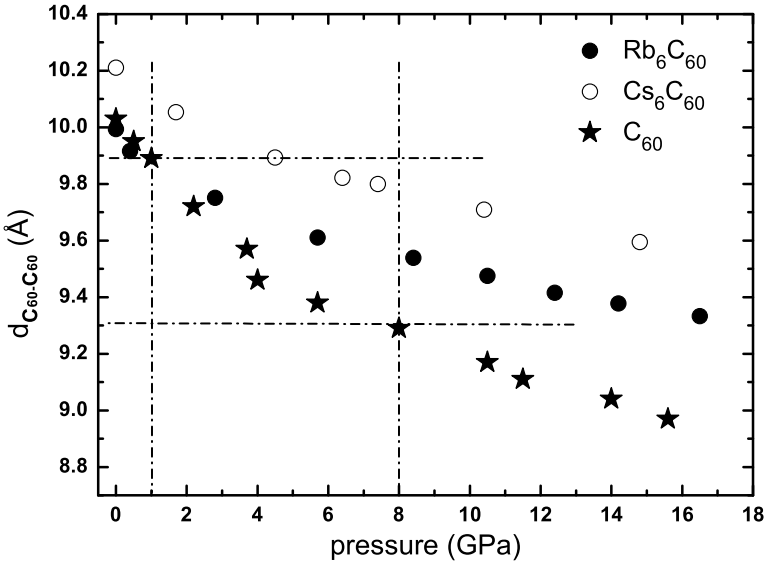

Figure 8.6: *Pressure evolution of the $d_{C_{60}-C_{60}}$ in Rb_6C_{60} and Cs_6C_{60} calculated from the equation of state obtained in chapter 3. Also the case of solid C_{60} is reported for a comparison. The vertical and horizontal dashed lines delimit the range in pressure (1–8 GPa) and distance between molecules (9.30–9.85 Å), respectively, where transitions towards polymerized structures have been observed in solid C_{60}.*

In Figure 8.6 we report the evolution of the nearest neighbouring molecule distance $d_{C_{60}-C_{60}}$ in Rb_6C_{60} and Cs_6C_{60}, as calculated from the equation of state obtained in chapter 3 and for the solid fcc C_{60}, calculated from the equation of state obtained by Duclos *et al.* [45]. The two vertical and horizontal dashed lines delimite the range in pressure (1–8

[1]In fact, the intermolecular distance in the bcc M_6C_{60} system is $d_{C_{60}-C_{60}}=\frac{a\sqrt{3}}{2}$ while in the fcc fullerite it is $d_{C_{60}-C_{60}}=\frac{a\sqrt{2}}{2}$.

GPa) and distance between molecules (9.30–9.85 Å), respectively, where polymerization has been observed for solid C_{60}. We can observe that at 5 GPa, the $d_{C_{60}-C_{60}}$ in both Cs_6C_{60} and Rb_6C_{60} is compatible with such a "distance range". Nevertheless, the formation of covalent bonds between molecules is not observed in our measurements. On the contrary, an irreversible transition towards disordered graphite and diamond for the Cs_6C_{60} and Rb_6C_{60} compounds, respectively, is observed through XRD and Raman measurements. Such transitions are thus accompanied by the breaking of the C_{60} molecules. Hence, the observation of the discussed irreversible transition in Cs_6C_{60} and Rb_6C_{60} as a function of temperature at around 5 GPa, suggests that in our systems the presence of the heavy alkali metal ions seems to prevent the polymerization of C_{60}. In addition, the MC_{60} systems (with M=K, Rb and Cs) have been observed to spontaneously polymerize at ambient conditions meaning that the presence of the ions in these compounds promotes the formation of covalent intermolecular bondings. As a consequence, the number of heavy alkali metal ions present in the fullerene-based systems and hence the quantity of transferred charge from the heavy alkali metals to the C_{60}s seems to play a fundamental role for the polymerization and probably on the behavior of the fullerenes under HP-HT conditions.

Another variable that could affect the formation of C_{60} polymers is the relative orientation of the molecules. While in pristine C_{60} the fullerenes are almost free to rotate (see chapter 1), in the Rb_6C_{60} and Cs_6C_{60} systems, the rotation is blocked by the presence of strong ionic interactions between each negative charged C_{60}^{-6} and the six positively charged alkali metal M^{+1} ions. Moreover, the resulting relative orientation between the nearest neighbouring molecules in these systems is different from that most commonly observed in the polymerized systems. In these last ones, the double bond placed at the edge of two hexagons of one molecule is facing the double bond placed at the edge of two hexagons of the neighbouring molecules. On the other hand, in the M_6C_{60} systems, two hexagons of two neighbouring molecules are facing each other in parallel (see chapter 1, Figure 1.12).

8.4 *Ab initio* DFT results

In order to get a deeper insight into the role played by the charge transfer to the C_{60} molecules on their polymerization, we performed *ab initio* DFT calculation on a simple system consisting of a chain of C_{60}s. In particular, we studied the evolution of the wavefunction of the system, around the Fermi level, as a function of two variables:

- the *distance*, *D*, between the centres of the molecules along the chain (8.74, 9.14, 9.85

and 10.5 Å);

- the *net charge*, q, consisting of 1, 2, 3 and 4 electrons transferred to the system.

The cubic unit cell, periodically repeated in the three Cartesian directions, contains 2 molecules in order to allow their relative reorientation during the study.

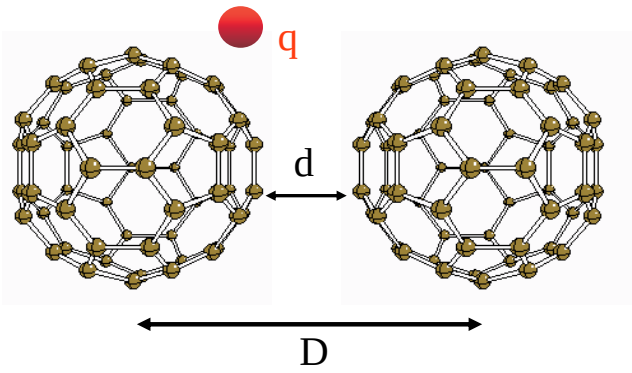

Figure 8.7: *Schematic representation of the minimum system used within the calculations. A cubic unit cell containing 2 molecules at a distance D is periodically repeated in the three Cartesian directions. The net charge of the system is varied from the neutral case up to 4 electrons.*

The lattice parameter is equal to D+d, where d is the distance between the two closest carbon atoms belonging to the two neighbouring molecules (see Figure 8.7). In this way, if the two nearest molecules at D distance are placed along the <100> direction, the distance between two neighbouring molecules along the <010> and the <001> directions is big enough to allow to consider them as not interacting. Therefore, we refer to the studied system as a chain of fullerenes. The starting relative-orientation of the molecules corresponds to that most frequently observed in the polymerization of solid fcc C_{60} [15] as discussed in chapter 1. This is shown also in Figure 8.7. According to this orientation, a double bond of one molecule (placed on the edge shared by two hexagons) is facing a double bond of the neighbouring molecule.

For each periodically repeated system, i.e. two molecules at a distance D, we studied the effect of different numbers of electrons transferred to it, from the neutral case up to a net charge of 4 electrons.

We have used the SIESTA [120] method, discussed in chapter 2, based on the density functional theory. We used variationally optimized [121, 122] double-ζ polarized basis sets. Real space integrals were performed on a mesh with a 200 Ry cutoff. In the calculations *2s* and *2p* orbitals of C atoms were explicitly included in the valence. For each calculation, we have minimized the total energy until the forces on atoms are smaller than 0.04 eV/Å.

In our calculations, the minimum neutral system, corresponding to two molecules, is represented by 480 valence electrons ($2s$+$2p$ electrons/carbon atom). This means that there are 240 occupied states since each electronic level contains 2 electrons of opposite spin. For the charged system, when a maximum of 4 additional electrons are considered, there are 242 occupied states.

8.4.1 Neutral systems

The wavefunction corresponding to the formation of two covalent σ bondings between two nearest neighbouring molecules, i.e. the polymerization, for all the studied systems in the neutral case, is shown in Figure 8.8. For the system where molecules are at D=8.74 Å, the wavefunction corresponding to the polymerization of the molecules is represented by the 238 eigenstate. Since the 238 bonding eigenstate is occupied, while the corresponding antibonding state (248) is at much higher energy and is not occupied, the ground state of this system correponds to a chain of polymerized fullerenes, i.e. each C_{60} is covalently linked to the two nearest neighbouring molecules.

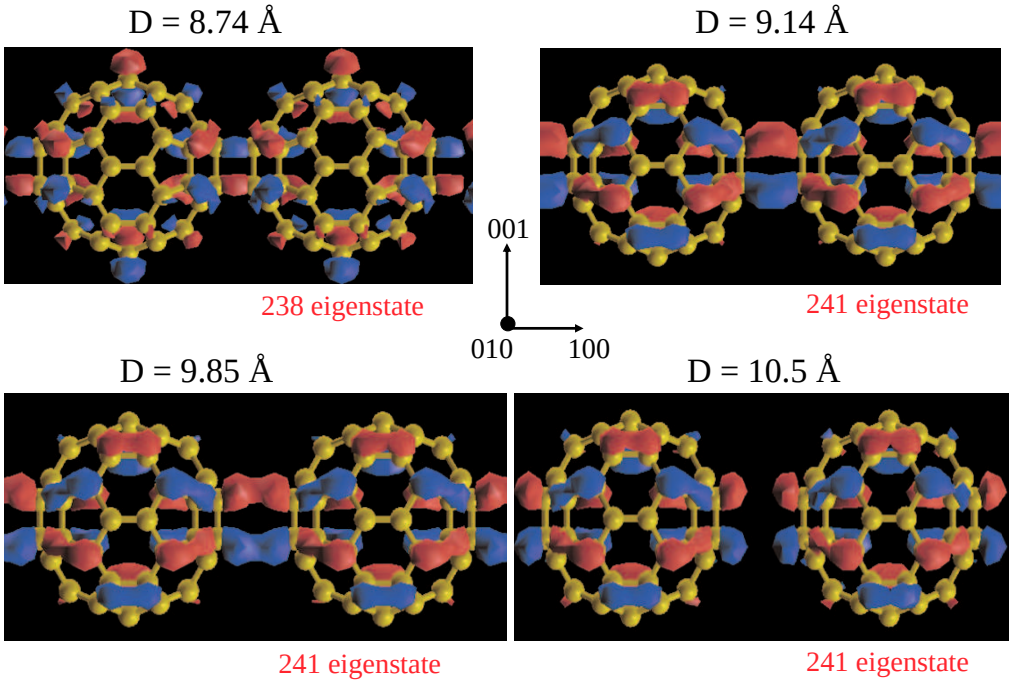

Figure 8.8: *Representation in real space of the eigenstates corresponding to covalent* **BONDING** *between molecules for each studied system, in the neutral case. In all cases, the wavefunction is plotted using the same threshold value for the isosurfaces.*

When considering larger distances between the molecules, in particular 9.14, 9.85 and 10.50 Å, the wavefunction corresponding to two covalent σ bondings between two nearest

neighbouring molecules, is the 241 eigenstate, which is not occupied in the case of neutral structures. Its symmetry is equal for the three systems as can be appreciated in Figure 8.8 but, at the same time, it is clearly different from the 238 wavefunction, corresponding to the covalent bonding state for the system with D=8.74 Å. As a matter of fact, we observe that the symmetry of the wavefunction around the Fermi level, is actually different when passing from the polymerized system (D=8.74 Å) to the non-polymerized systems (D=9.14, 9.85 and 10.50 Å).

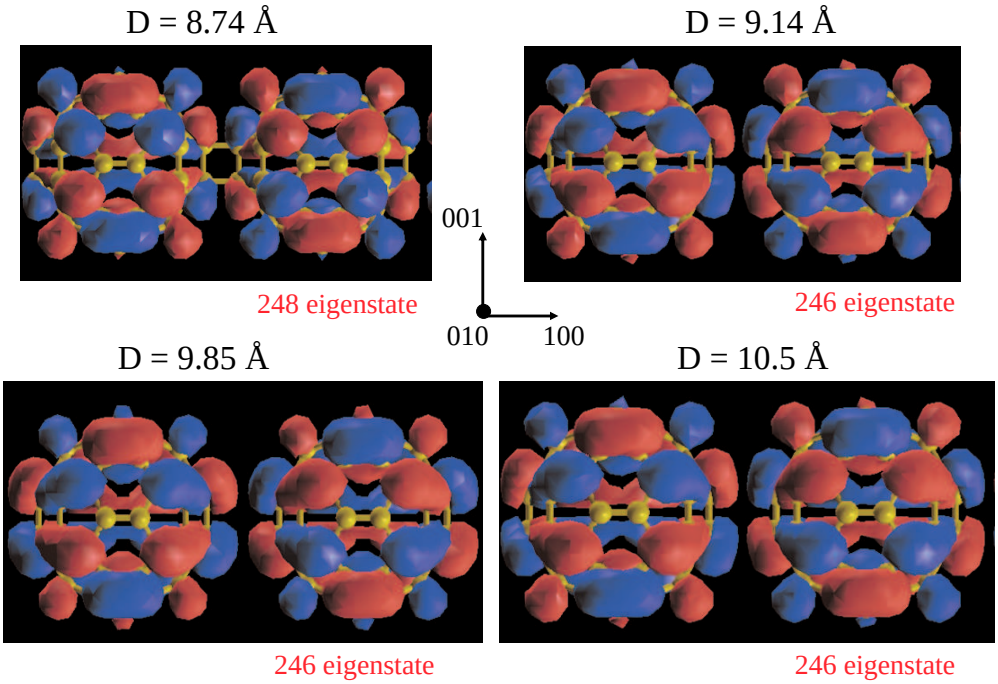

Figure 8.9: *Representation in real space of the eigenstate corresponding to the* **ANTI-BONDING** *state between molecules for each studied system, in the neutral case. In all cases, the wavefunction is plotted using the same threshold value for the isosurfaces.*

For the three systems, the 241 covalent bonding state also corresponds to the lowest unoccupied molecular orbital (LUMO) while the 240 state is the highest occupied molecular orbital (HOMO) [2]. The energy difference between the 240 and 241 state, i.e. the HOMO-LUMO gap, increases with the increase of the intermolecular distance. In particular, we obtain 0.6, 1.2 and 1.5 eV[3], respectively, for the systems where the nearest

[2]Since we are dealing with a solid and not with a molecule, we should refer to bands and not to orbitals; nevertheless since the lowest unoccupied band and the highest occupied band derive from the LUMO and HOMO, respectively, in this chapter we keep the nomenclature used for molecules in order to make reading easier.

[3]In Table 8.1 we do not report the HOMO-LUMO gap value for the systems with molecules at 8.74 Å because in this case the LUMO does not correpond to covalent σ bondings between the molecules.

neighbouring molecules are at 9.14, 9.85 and 10.50 Å (see Table 8.1). This proves that it is energetically more favourable to occupy the bonding state (LUMO) when the molecules are closer to each other in the chain.

The wavefunction corresponding to the antibonding state for the four systems is shown in Figure 8.9. While for the system with D=8.74 Å, the antibonding state corresponding to the 238 bonding state is the 248 eigenstate, for the three systems with bigger D, the antibonding state, correponding to the covalent 241 bonding state, is the 246 eigenstate. In the latter cases, the energy difference between the bonding (241) and the antibonding (246) state, decreases with the increase of the intermolecular distance. In particular, ΔE=E$_{antibonding}$-E$_{bonding}$ is 0.7, 0.4 and 0.2 eV for the systems with D equal to 9.14, 9.85 and 10.50 Å, respectively. This indicates that the bonding state is energetically more stable with respect to the antibonding state, much more for smaller intermolecular distances.

8.4.2 Charged systems

The calculations performed for the four different structures in the presence of a net charge show that the symmetry of the wavefunction around the Fermi level, in all cases, is unchanged when considering from 1 up to 4 electrons transferred to the system. The presence of additional electrons only contributes to the occupation of the electronic states which are not occupied in the neutral system. Hence, for the different systems we observe that:

- D=8.74 Å: the molecules remain polymerized up to a net charge of 4 electrons because no antibonding state is observed up to the 242 eigenstate. In particular, the 239, 240 and 242 wavefunctions correspond to intramolecular bonding states while the 241 wavefunction represents an an intermolecular bonding state through 4 σ bondings between two nearest neighbouring molecules, with different symmetry

D (Å)	HOMO-LUMO gap (eV)	E$_{antibonding}$-E$_{bonding}$ (eV)
8.74		2.26
9.14	0.6	0.7
9.85	1.2	0.4
10.50	1.5	0.2

Table 8.1: *Evolution of the HOMO-LUMO gap and the ΔE between the antibonding and the bonding state as a function of the intermolecular distance D for the 1D C_{60} chain.*

with respect to the 238 eigenstate;

- D=9.14, 9.85 and 10.50 Å: when considering a net charge of 1 or 2 electrons, the 241 eigenstate (corresponding to the presence of two covalent σ bondings between molecules) becomes occupied, thus promoting the polymerization. If a net charge of 3 or 4 electrons is considered, there is the occupation of the 242 eigenstate which corresponds to an intermolecular bonding state, with different symmetry compared to the 241 (equal to the 241 bonding state of the previous case).

D (Å)	d_{q_0}-d_{q_1} (Å)	d_{q_0}-d_{q_2} (Å)	d_{q_0}-d_{q_3} (Å)	d_{q_0}-d_{q_4} (Å)
8.74	0.001	0.001	0.001	0.001
9.14	0.042	0.072	0.066	0.056
9.85	0.027	0.057	0.044	0.41
10.50	0.016	0.027	0.031	0.035

Table 8.2: *Evolution as a function of the intermolecular distance D of the difference between the d distance (see Figure 8.7) in the neutral chain and in the charge one. The labels q_0, q_1, q_2, q_3 and q_4 indicate the neutral system, 1, 2, 3 and 4 electrons transferred to the system, respectively.*

In agreement with these results, we observe an evolution of the distance, d, between the nearest neighbouring carbon atoms coming from different molecules (see Figure 8.7) as a function of the net charge in the system. The results concerning the evolution of the distance d in the four different systems are reported in Table 8.2.

While the system with D equal to 8.74 Å, which is polymerized even in the neutral case, the presence of a net charge does not significantly affect the structure, in the other three systems, the occupation of the bonding states upon charge transfer promotes the closeness of the nearest neighbours carbon atoms coming from different molecules. Moreover, the variation of the d distance with the occupation of the 241 bonding state depends on the intermolecular distance. For systems with closer molecules, this variation is bigger. For the systems with the intermolecular distance equal to 9.14 and 9.85 Å, the smallest d distance is observed for q=2 electrons, i.e. when the 241 bonding state is the HOMO state and in addition is completely filled. On the other hand, the system with D equal to 10.50 Å, shows a minimum distance for q=4 electrons.

8.4.3 Discussion

We have performed *ab initio* DFT calculations on very simple systems consisting of infinite chains of fullerenes in order to understand if the presence of a net charge coupled with different distances between the molecules in the chain could play a role for the polymerization.

Hence, the variables of the calculations are the distance between the molecules, D, and the number of electrons transferred to the system, q.

We observe that at the intermolecular distance of 8.74 Å, the ground state of the neutral system corresponds to polymerized molecules, as the 238 occupied state corresponds to covalent sigma bonds between the molecules. By adding electrons to the system, the symmetry of the wavefunction remains unchanged, the only effect is to occupy the 240 and the 241 states. As a consequence, the covalent σ bonds are not broken since the antibonding state is at much higher energy.

When the intermolecular distance is 9.14, 9.85 or 10.50 Å, the bonding state correponds to the 241 eigenstate and since this is not occupied in the neutral systems, the molecules are not polymerized for q=0. By adding electrons to the systems, as above, the symmetry of the wavefunction remains unchanged meaning that the polymerization between molecules takes place by occuping the 241 state.

For the polymerized system (i.e. for D=8.74 Å) the presence of additional electrons does not affect the distance between the nearest neighbouring carbon atoms belonging to different molecules, as shown by the evolution of the d. This is probably due to the fact the bonds between the molecules is very strong and that the occupation of new states (intramolecular bonding states) does not weaken it. This is also shown by the big energy difference between the bonding and the antibonding state, compared to the other systems.

When the intermolecular distance is bigger, for D=9.14 and 9.85 Å, the complete occupation of the 241 covalent bonding state determines the minimum value of the distance d.

The system with D=10.50 shows instead a minimum value of d for the occupation of the 242 state which is an intermolecular bonding state through 4 σ bonds between 2 nearest neighbouring molecules. This is probably due to the fact that at this distance, the covalent σ bonds corresponding to the 241 state are very weak so that they are strengthened by the occupation of another intramolecular bonding state.

The total variation in the d distance upon occupation of the covalent bonding state decreases for the bigger intermolecular distances. This indicates that for these systems the covalent intermolecular bondings are weaker, as can also be observed in Figure 8.8

where the wavefunction isosurface value between the molecules decreases for the higher distances. In agreement with this, we observe that the energy difference between the covalent bonding state and the corresponding antibonding state is smaller for the higher distances.

In conclusion, the coupled effect between the presence of a transfer of charge and the distance between molecules could determine the formation of C_{60} polymers, in the systems that we have studied. Since the relative orientation of the nearest neighbouring molecules in the M_6C_{60} compounds is different from that considered here, it would be interesting to perform a similar study by considering a chain of fullerenes with that relative orientation in order to understand how this could affect the polymerization.

Conclusions

The research activity carried out during this thesis work was aimed to explore the phase diagram of Rb_6C_{60} and Cs_6C_{60} having as initial motivation the synthesis of carbon clathrate-type materials under high pressure and/or high temperature conditions. Such carbon networks, obtained as high dimensional polmyers starting from the Rb_6C_{60} and Cs_6C_{60} body centered cubic structures, are expected to exhibit both superconducting properties and extremely high hardness.

In particular, the goal of this work was motivated by several theoretical works indicating that such polymerized structures, characterized by sp^3 hybridized bonds between molecules, should exhibit a high critical superconducting temperature close to room temperature. Moreover, a high bulk modulus coefficient, possibly exceeding that of diamond, as observed for 3D polymerized structures obtain from pristine solid fcc C_{60}, is also expected for these structures.

The work reported in this thesis includes a series of XAS, XRD and Raman spectroscopy measurements collected for the two systems in a wide range of pressures (up to $\sim$ 50 GPa) and temperatures (from room temperature up to 1500 Kelvin) and *ab initio* DFT calculations performed on the same compounds under pressure (up to 100 GPa) (at zero Kelvin).

In chapter 4, we have reported both experimental and first principles studies on Rb_6C_{60} and Cs_6C_{60}. By coupling the complementary information obtained by XRD and EXAFS with the results obtained by *ab initio* calculations we made possible the understanding of the mechanisms taking place during the compression of such systems.

As a result, we observed that the compression of the C_{60} molecule is accompanied by an enhanced pressure-induced deformation which preserved the cubic T_h symmetry. In order to better describe the molecular distortion, we defined a distortion parameter, d, as the difference between the distances from each molecule's centre to those 36 carbons closest to the alkali metals, on one hand, and to those 24 carbon atoms located closest to other C_{60} molecules, on the other. Both experiments and calculations agree with a deformation

of the fullerene molecule which is more important for Rb than for Cs intercalation.

In chapter 5, we report a study on Cs_6C_{60} under higher pressure. We performed Raman spectroscopy measurements at room temperature up to 45.5 GPa and *ab initio* calculations up to 43 GPa. Both experiments and calculations allow us to conclude that the molecular character of the C_{60} fullerene can be maintained through alkali intercalation up to pressures at least two times higher (around 45 GPa) than for previously reported solid C_{60} (around 22 GPa). Moreover, the Raman spectra obtained by first principles calculations allow us to identify the symmetry of the six new observed lines with respect to the active Raman modes of the isolated molecule.

In chapter 6, we reported a study of Rb_6C_{60} under pressure up to around 49 GPa performed by XAS, XRD and Raman spectrscopy. We observed a clear reversible phase transition at around 35 GPa, by XRD and Raman spectroscopy, at 600 K and room temperature, respectively. The results obtained by coupling the two techniques, allow to suggest that the hexagonal unit cell structure identified after the transitions, is accompanied by the formation of 2D polymerized C_{60} molecules in the (001) plane of the hexagonal structure containing the $\overrightarrow{a}$ $\overrightarrow{b}$ unit-cell vectors. In particular, the lattice parameters of the hexagonal unit cell (a=8.360(2) Å and c=14.830(7) Å) are compatible with a distance bewteen molecules previously observed in the case of polymerized C_{60}s. In correspondence of this transition, the Raman spectroscopy measurements show a discontinuous change in the frequency of the intramolecular normal vibrations, probably associated with the breaking of some intramolecular bonds concomitant with the formation of new intermolecular covalent bonds, as occurs in the polymerization of C_{60}s.

Unfortunately, XRD and XAS studies have not been performed on Cs_6C_{60} under high pressure and/or high temperature but a different high pressure behaviour is nevertheless observed by Raman spectroscopy, for this system compared to the Rb_6C_{60}. While an abrupt change in the Raman modes frequencies is observed at 35 GPa for Rb_6C_{60}, as mentioned above, a continuous evolution of the Raman active modes is observed for Cs_6C_{60} up to the highest measured pressure, i.e. 45 GPa. The results obtained from the *ab initio* calculations, reported in chapter 7, performed as a function of pressure on the two systems allowed to better understand this different pressure behavior, observed for the two compounds.

In particular, the calculations show the existence of a pressure instability of the bcc structure of Rb_6C_{60} between 75 and 100 GPa ,contrary to the case of Cs_6C_{60}. In correspondance of this "transition" we observe a discontinuous modification of both structural and electronic properties of the Rb_6C_{60} system. In particular, we observe that at 100 GPa,

the single and double C-C intramolecular bonding lengths and the C_{60} volume abrupty increases leading to a shape change of the fullerene. In addition, an abrupt opening of the gap between the highest occupied and the lowest unoccupied bands and a discontinuity in the decrease of the charge transfer from the alkali Rb atoms to the molecules, are also obtained. On the other hand, a continuous evolution of the structural and electronic properties is observed for Cs_6C_{60} up to 98 GPa reflecting a higher pressure range of stability for this system compared to Rb_6C_{60}. The theoretical study of the pressure evolution of the charge transfer from the alkali metal ions to the fullerene molecules has been studied in two different ways, by considering the Mulliken-population analysis method and by studying the electronic density contained in each molecule. Both methods allow to conclude that the charge transfer, continuously decreases as a function of pressure for both systems and that the charge transfer decrease with pressure in Cs_6C_{60} is less pronounced compared to the Rb case. At the same time, the pressure induced distortion of the fullerenes increases less fastly than in Rb_6C_{60}. In particular, the distortion parameter is 100% higher for the Rb case than in the Cs one right before the transition observed by the calculations, i.e. at around 75 GPa.

Therefore, since the charge transfer decreases more rapidly in Rb_6C_{60} than in Cs_6C_{60} with pressure and the molecular pressure-induced distortion observed in the Rb case is bigger that in the Cs case, we suggest that the ionic interactions between the positively charged alkali ions and the negatively charged C_{60} molecule prevent the pressure deformation of the molecule promoting its pressure stability. Consequently, the Coulomb interactions seems to be responsible for the bigger pressure stability range (more than twice) of the C_{60} molecule in the studied systems compared to the non intercalated solid C_{60}, as observed from our measurements.

The XRD study, performed on Rb_6C_{60} and Cs_6C_{60} as a function of temperature at a constant pressure (around 5 GPa) and reported in chapter 8, demonstrated the occurrence of an irreversible transition at high temperature accompanied by the disappearence of all the Bragg reflections. In the non intercalated solid C_{60}, the different studies performed at the same conditions of pressure and as a function of temperature showed before the occurrence of the C_{60} polymerization and the the partial destruction of molecules. In particular, those studies showed the formation of 1D and 2D polymers in the pristine fcc C_{60} system under pressure, when the distances between the nearest neighbouring molecules are equal to those existing between two nearest neighbouring molecules in our systems. In addition, fullerides with lower stoichiometric amount of heavy alkali metals (MC_{60}, M=K, Rb and Cs) have been observed to spontaneously polymerize at ambient conditions. All

these experimental observations indicate that the particular stoichiometry of the heavy alkali metals in this fulleride and the consequent presence of ionic interactions, togeether with a fixed relative orientation between molecules different from that observed in polymerized C_{60}, must play an important role on the formation of covalent bonds between molecules. The calculations performed during this work on systems consisting on chains of fullerenes oriented by facing the double bonds edge, actually confirm the importance of the charge transfer. By studying the coupled effect of the distance between the molecules and the presence of a various net charges on the system, we observed that the the transfer of charge could promote the formation of covalent bonds between molecules.

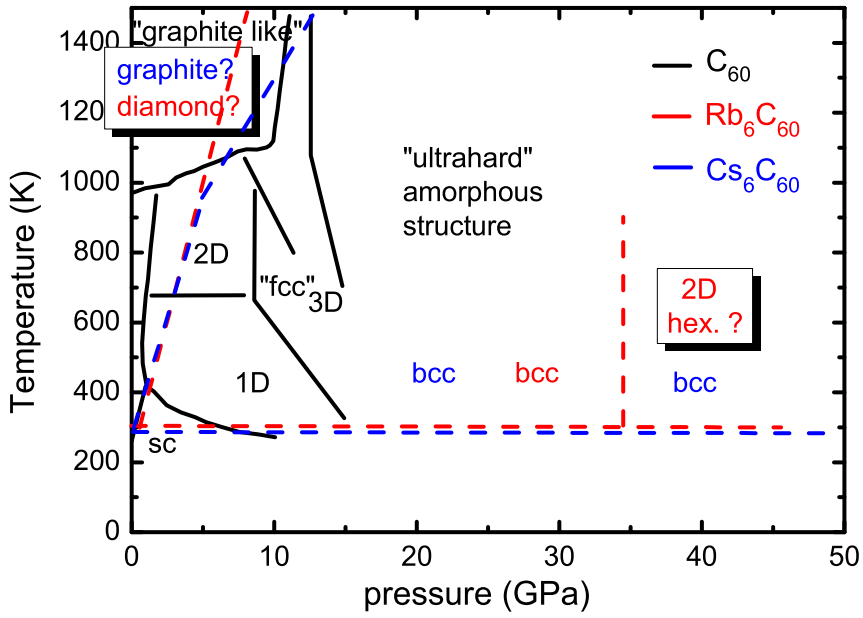

Figure 8.10: *Phase diagram of Rb_6C_{60} and Cs_6C_{60} as obtained from the in situ measurements performed during this work. A comparison with the "reaction diagram" of solid C_{60} is also reported.*

The phase diagram of Rb_6C_{60} and Cs_6C_{60} explored in this work by coupling several experimental techniques is shown in Figure 8.10 where we compare the results obtained in this thesis with those previously reported for solid C_{60}. Our results, summarized in Figure 8.10, allow to affirm that in the studied systems, compared to the case of solid fcc C_{60}, the polymerization seems to be prevented by the presence of heavy alkali metal ions as obtained by the XRD study performed at 5 GPa at high temperature. Moreover, since in

this work the formation of C_{60} polymers has probably been observed at 35 GPa and 600 K, this means that a much higher pressure, i.e. a much smaller distance between molecules, is needed in this case in order to observe the formation of covalent bonds between molecules.

In order to further progress in this work, we propose additional accurate XRD studies on Rb_6C_{60} to definitively identify not only the structure symmetry of the new phase observed at around 35 GPa and 600 Kelvin but also the atomic positions in the unit cell. This would allow to perform calculation on such new structure in order to check its pressure stability with respect to the bcc phase. In this thesis work, we observed the reversibility of the phase transition of Rb_6C_{60} at 600 Kelvin around 35 GPa. We propose to collect XRD measurements at ambient conditions, by quenching the sample from 600 Kelvin down to room or even lower temperature, at high pressure. This could allow to metastabilize the new phase down to ambient conditions and hence to check for the existence of superconducting properties by resistivity and magnetic susceptibility measurements.

Moreover, Stokes and anti-Stokes Raman spectra collected on Rb_6C_{60} at room temperature will provide the effective temperature of the sample, which could be higher than the room temperature due to the laser heating.

Concerning the Cs_6C_{60} system, we propose to collect XRD and XAS data under high pressure and high temperature conditions in order to confirm the absence of phase transitions, as suggested by Raman spectroscopy measurements.

In addition, with respect to *ab initio* calculations, the initial idea was to compare to results obtained by using the LDA and the GGA functionals but we finally didn't manage to to employ the second approximation due to lack of time. Moreover, we also planned to study the role of the charge transfer on the polymerization (chapter 8) by considering, in addition to the net charge on the system, also a background charge in order to neutralize the excess charge in the system. Consequently, we propose to perform such studies in order to provide a more complete treatment of the subject. Also, as discussed in chapter 8, we propose an additional study about the role of the net charge on 1D C_{60} chains, by considering a different relative orientation of the molecule, in particular that existing between the nearest neighbouring molecules (placed along the diagonal of the cubic cell) in M_6C_{60} systems.

Concerning the initial motivation of this work, i.e. the synthesis of high dimensional polymers of intercalated fullerene, we propose to study fullerides with lighter alkali metal ions under extreme conditions. The presence of smaller ions could promote the formation of covalent intermolecular bonds at lower pressures, compared to the fullerides studied in

this work. Alternatively, the same study on fullerides with lower stoichiometric amounts of alkali metal atoms could be envisaged.

Acknowledgements

During these three years numerous persons gave an important contribution to this work. I refer not only to the collegues and supervisors that guided me in the scientific work but also to my close relatives and family members whose endless support encouraged me most.

First of all, my deepest acknowledgements go to my thesis director, Prof. Alfonso San Miguel, whose scientific enthusiasm has been a precious constant during my work. In particular I want to thank him for giving me the possibility of working on this subject that I really liked and for providing me as much help as I needed and as much scientific freedom as I wished.

I also would like to thank all the people I worked with in these years at the ESRF for making this "synchrotron" experience unforgettable. In particular I thank my supervisor at the ESRF who was also my second thesis director, Sakura Pascarelli, for giving me the opportunity of working in her group. I want to thank her also for the experimental assistence during experiments and for helping me during all this period. I want to express my sincere gratitude to Giuliana Aquilanti for her helpfulness and patience during difficult and sometimes daunting high pressure experiments. I really appreciated all the time she spent for helping me in the preparation of my experiments. Many thanks also to Simone De Panfilis for the interesting discussions about XAS and for encouraging me during my scientific "crisis". Thanks to all my colleagues of BM29 and ID24 for the nice work ambience and also for all the science I learnt through our discussions Angela, Olivier, Gianluchino, Gemma, Marco, Matt, Lello ... I want to thank as well Sebastian for his precious technical support on the high pressure devices.

My acknowledgements also go to all my colleagues at the LPMCN. The most sincere gratitude go to Sylvie Le Floch for her essential support on the synthesis of the samples. In addition, her help for the manipulation of our air sensitive compounds was fundamental for performing this work. I also want to thank Pierre Toulemonde and Denis Machon for patiently answering all my questions about XRD and Raman spectrocopy. They also gave

me an important support during the experiments and their preparation. I want to as well thank Herve Feret for his precious technical work on the high pressure apparata we employed during the experiments.

Special acknowledgements go to Maria Victoria Fernandez-Serra for introducing me in the wide and difficult world of the DFT simulations. I also appreciated her patience and comprehension when dealing with my silly (not for me!) questions.

My sincere gratitude to Michela Brunelli for being so kind to permit me to characterize my samples by XRD during her beamtime. Her help was essential in order to establish the good synthesis parameters.

I also want to thank Dr. Leonel Marques for interesting discussions on C_{60} and its polymerization and for his help in the understanding of XRD data.

I sincerely thank David Martinez-Blanco for his important support when using the FULLPROF package. His enthusiasm when performing Rietveld fits gave me the illusion of playing a video game.

Many thanks also to Gilles Montagnac and Herve Cardon for giving me the possibility to perform Raman experiments during my thesis. Their technical support made possible the succees of interesting experiments.

I would like to thank Wilson Crichton and Mohamed Mezouar for helping me in performing and understanding x-ray diffraction experiments.

My most sincere gratitude to all my friends from Italy (in particular from Morrovalle and Civitanova) and those I have met here in Grenoble. Thanks for making this french experience unforgettable. Thank you Chiara (Kiaua), Elena, Federica, Franceso (Ofra), Mauro, Mirko, Fabiola (Futiola), Orietta, Maria, Myriam, Pedro, Miguel, Gemma, Mischa, Felisa, Otello (Otiello), Elisa, Gianluca, Fabrizio, Lorena, Roberto, Edmundo, Gaston, Andrea (Andy), Diana, Julio (Culio or Coolio), Montserrat (Mun), Guillaume, Jorge, Sandra, Manu ...

I owe my heartfelt gratitude to my family ... for many reasons ...

Finally, most thanks go to Alex (naiño) for supporting and encouraging me during all the thesis period and for tolerating my numerous mood changes (in particular) at the end of my thesis ... I liked a lot the stimulating scientific discussions about C_{60} and imogolite ...

Appendix A

Sample synthesis

In this appendix we explain the method that we used for the synthesis of the samples. Even though the synthesis procedure for similar systems can be found in literature [60, 144], we did not follow exactly these methods but we rather attempted a new synthesis scheme that arose after stimulating discussions with Prof. Laurent Duclaux.

All the preparation process has been performed in the chemistry and in the high pressure laboratory at the LPMCN of the University Lyon 1, in Lyon. In the following we describe the main steps:

- Fullerene cleaning: the first step consisted in the fullerite cleaning. The C_{60} powder enclosed in a sealed quartz tube was heated at 550 K and pumped at the same time at $5*10^{-7}$ mbar during ten hours.

- Stoichiometric mixing: the Rb_6C_{60} and Cs_6C_{60} compounds were prepared by mixing stoichiometric amounts of annealed C_{60} (99.95+ % purity) with Cs and Rb (99.98 % purity) metals in glove box, respectively. In addition, a small excess amount of alkali metals were used (respectively 2.5% and 3% wt of Cs and Rb) because they were observed to remain on the quartz tube after the synthesis. In Figure 8.11 we show a picture of the glove box used for avoiding sample degradation. The mixing process must be performed in inert atmosphere in order to avoid sample reaction or contamination due to the presence of the alkali metals, extremely sensitive to air and humidity.

- Vacuum sealing: the mixed powder placed in a quartz tube was pumped in vacuum at $5*10^{-7}$ mbar during ten hours (as for the fullerite cleaning) before sealing.

- Reaction: the solid state reaction was obtained by annealing the mixed powder enclosed in a sealed evacuated quartz tube at high temperature for several days. The

Figure 8.11: *Picture of the glove box employed during the sample synthesis in order to avoid reaction or contamination of both the Rb and Cs alkali metals and the final* Rb_6C_{60} *and* Cs_6C_{60} *compounds.*

sealed tube is placed in the middle zone of a tubular furnace, shown in Figure 8.12 where temperature is almost homogeneous. During the first year of my PhD, we performed many different sample synthesis by varing these parameters (temperature and time) before obtaining an excellent data quality. After each synthesis process we verified the sample quality by XRD. The best data quality was obtained by annealing the mixed powder at 600 K for 35-40 days.

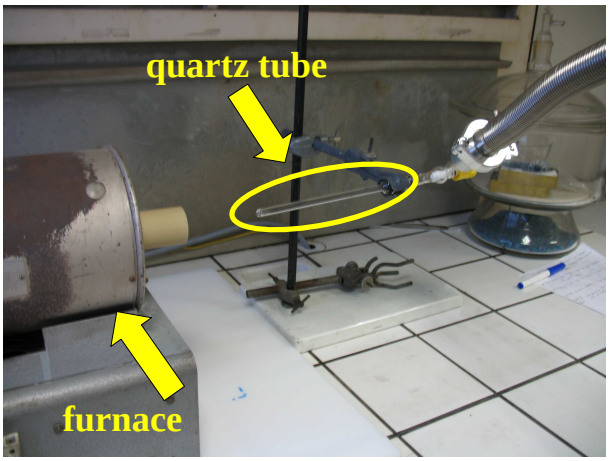

Figure 8.12: *The picture shows the quartz tube containing the powder sample pumped at* $5*10^{-7}$ *mbar. After sealing the ampoule is placed in the central zone of the furnace.*

The annealing time was found to be a critical parameter for the synthesis of the M_6C_{60} (M=Rb and Cs) compounds. By increasing it from a few days (two or three) up to 40 days, the result improved considerably. In particular, we observed that no

sign of the M_6C_{60} compound was present in the XRD patterns for the first case (a few days), while a high percentage of the M_6C_{60} phase was synthesized, in addition to other stoichiometric compounds, like M_3C_{60} and M_4C_{60}, in the second case (40 days). Moreover, we observed that by increasing the annealing temperature from 550 up to 600 K the data quality further improved. In particular, the samples prepared at 600 K during 40 days were pure M_6C_{60} phase (Figure 8.13, (c) and (d)). We also performed a synthesis of the two compounds by increasing the annealing temperature up to 700 K and by decreasing the "reaction"time down to 15 days. The sample characterization performed by XRD and Raman spectroscopy displayed the lack of Bragg reflections of the M_6C_{60} phase.

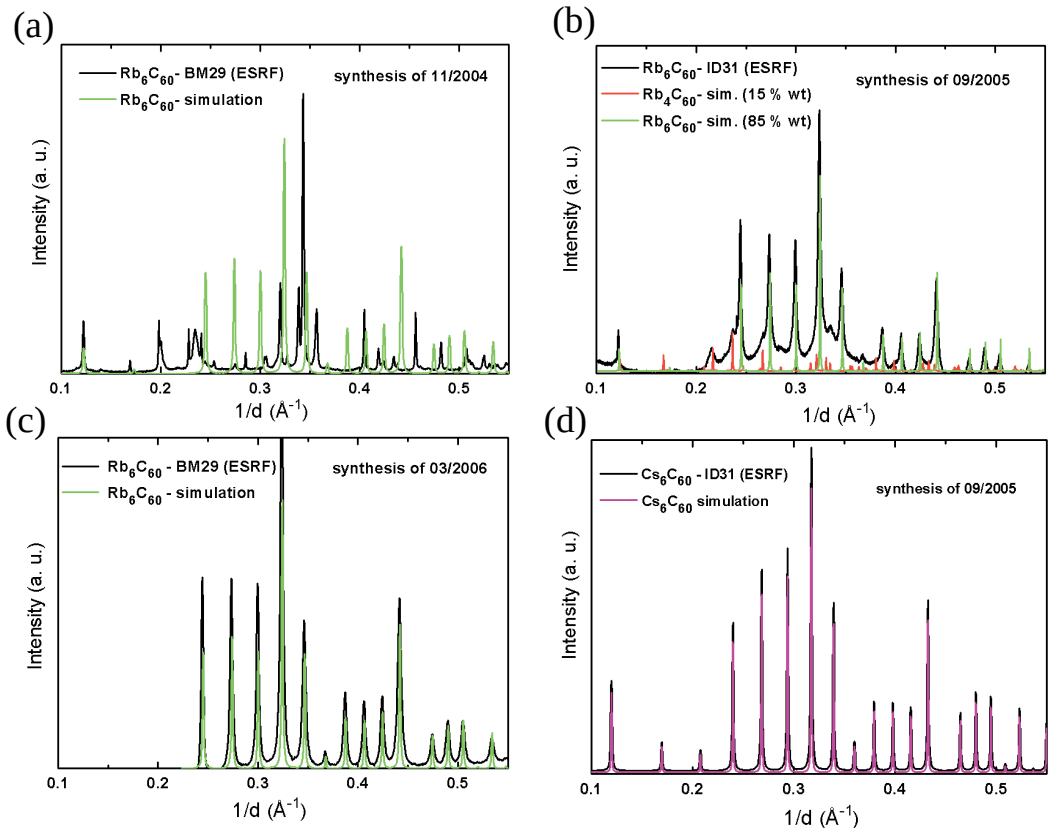

Figure 8.13: *XRD patterns collected on the some of the different samples synthesized during my first year of PhD. The experimental data are reported together with the simulated patterns obtained by considering the crystalline structures reported in literature [113]. The different synthesis have been performed by varing both temperature and time in the annealing process. For Rb_6C_{60}: (a) 550 K-3 days; (b) 600 K-30 days and (c) 600 K-40 days. For Cs_6C_{60} (d) 600 K-40 days.*

The obtained Rb_6C_{60} and Cs_6C_{60} powder compounds are extremely sensitive to air

and humidity. For this reason the sample preparation for the high pressure and high temperature experiments has been performed in glove box (Figure 8.11).

In Figure 8.13 we report some XRD patterns collected on different synthesized samples in order to check the good stoichiometry of the obtained compounds. The shown XRD data have been collected at the ID31 beamline (ESRF) and at the BM29 beamline (ESRF). We display four different patterns. The data shown in panels (a), (b) and (c) of Figure 8.13 are reported by following the chronological order of the corresponding synthesis. We can observe that the quality of the sample improved considerably for the last synthesis process.

The XRD pattern reported in panel (a) corresponds to a sample obtained by annealing the mixed powder at 550 K for three days. The Rb_6C_{60} compound is not present in the powder. The sample whose XRD pattern is shown in panel (b) displays better quality compared to the previous one, the presence of both Rb_6C_{60} ($\sim$ 85 % in wt) and Rb_4C_{60} ($\sim$ 15 % in wt) compounds. The synthesis was performed by annealing the powder at 600 K for 30 days. The most recent sample synthesis, reported in panel (c) was annealed at 600 K for 40 days and the corresponding XRD patterns shows the good quality of the sample. The XRD pattern reported in panel (d) corresponds to the Cs_6C_{60} compound, synthesized using the same values of the temperature and time variables employed for the synthesis of the Rb_6C_{60} whose XRD pattern is shown in panel (c). The data quality is excellent.

Appendix B

Bond polarizability model for the Raman spectra of fullerenes

In this appendix, we describe the bond polarizability model reported in Ref. [136] and used in chapter 5 in order to select the Raman active modes of the C_{60} molecule among the 192 calculated normal vibrations in the Cs_6C_{60} system.

The intensity of the first-order off-resonance Stokes Raman scattering for a harmonic system can be written as:

$$I_{\eta'\eta}(\omega) = C\omega_L\omega_S^3 \sum_{f=1}^{3N} \frac{\langle(\omega_f)\rangle + 1}{\omega_f} \Big|\sum_{\alpha\beta} \eta'_\alpha \eta_\beta P_{\alpha\beta,f}\Big|^2 \times \delta(\omega - \omega_f) \tag{8.1}$$

Here, C is a frequency-independent constant; ω_L and ω_S are the incident and scattered light frequencies, respectively; $\omega \equiv \omega_L = \omega_S$ is the Raman shift; η and η' are unit vectors along the incident and scattered polarization directions, respectively; $\langle n(\omega_f)\rangle \equiv [exp(\beta\hbar\omega_f) - 1]^{-1}$ is the thermal average occupation number of mode f at temperature $T = (k_B\beta)^{-1}$ and the quantity $P_{\alpha\beta,f}$ is the derivative of the electronic polarizability tensor with respect to the normal coordinate for mode f. Hence, the calculation of the Raman spectrum requires mode frequencies, mode eigenvectors and polarizability derivatives. In terms of the mode eigenvectors, $P_{\alpha\beta,f}$ is given by:

$$P_{\alpha\beta,f} = \sum_{l\gamma} \left[\frac{\partial P_{\alpha\beta}}{\partial u_\gamma(l)}\right]_0 \chi_\gamma(l|f) \tag{8.2}$$

where $[\partial P_{\alpha\beta}/\partial u_\gamma(l)]_0$ are the electronic polarizability derivatives with respect to the real-space atomic displacements $u_\gamma(l)$, evaluated at the system's equilibrium configuration. Here l=1,N labels the atomic sites, γ=1,3 labels Cartesian components and $\boldsymbol{\chi}(f)$ are the mode eigenvectors. In order to evaluate the derivatives in eq. 8.2, we assume that the static electronic polarizability of a molecule can be expressed as a sum of individual bond polarizabilities. In addition, we make the "zero order approximation", meaning that the

bond polarizability parameters are functions of the bond lengths R only, i.e. $\alpha_{\parallel} \equiv \alpha_{\parallel}(R)$ and $\alpha_{\perp} \equiv \alpha_{\perp}(R)$. This approximation neglects the dependence of a bond's polarizability on the motion of atoms not connected to that bond. The equilibrium-configuration derivatives of the polarizability with respect to the atomic displacements $u_{\gamma}(l)$ are then easily linked to derivatives with respect to the γ components of the three dimensional bond vectors $\mathbf{R}(l,B)$ from atom l to neighbouring atom B. Being the displacement of the l atom $\mathbf{u}(l)$ and keeping all other atoms fixed at their equilibrium positions, we have $\mathbf{R}(l,B) = \mathbf{R}_0(l,B) - \mathbf{u}(l)$, where $\mathbf{R}_0(l,B)$ is the equilibrium bond vector from atom l to atom B. We than obtain $P_{\alpha\beta,f}$ as a sum of three contributions:

$$
\begin{aligned}
P_{\alpha\beta,f} \;=\; & -\sum_{l}\sum_{B}\Bigg[\left(\frac{\alpha'_{\parallel}(B)+2\alpha'_{\perp}(B)}{3}\right)\mathbf{R}_0(l,B)\cdot\boldsymbol{\chi}(l|f)\delta_{\alpha\beta} + && (8.3)\\
& +[\alpha'_{\parallel}(B)-\alpha'_{\perp}(B)][\hat{\mathbf{R}}_{0\alpha}(l,B)\hat{\mathbf{R}}_{0\beta}(l,B) && (8.4)\\
& -\frac{1}{3}\delta_{\alpha\beta}]\mathbf{R}_0(l,B)\cdot\boldsymbol{\chi}(l,f) + \Big(\frac{\alpha_{\parallel}(B)-\alpha_{\perp}(B)}{R_0(l,B)}\Big) && (8.5)\\
& \times\Big(\hat{R}_{0\alpha}(l,B)\hat{\chi}_{\beta}(l|f) - \hat{R}_{0\beta}(l,B)\hat{\chi}_{\alpha}(l|f) && (8.6)\\
& -2\hat{R}_{0\alpha}(l,B)\hat{R}_{0\beta}(l,B)\mathbf{R}_0(l,B)\cdot\boldsymbol{\chi}(l|f)]\Big)\Bigg] && (8.7)
\end{aligned}
$$

Here, the primes denotes radial derivatives, the carets denote unit vectors and the sum over B extends over the bonds connected to site l. The first term in eq. 8.7 represents the change in the isotropic part of the polarizability induced by bond-stretching and the second term represents the corresponding change in the anisotropic part of the polarizability. The third term of eq. 8.7 corresponds to the change in the anisotropic part of the polarizability induced by bond rotations. In C_{60}, the A_g modes contribute to the first term and the eight H_g modes contribute to the other two.

The sum over bonds in eq. 8.7 includes two types of bonds, single and double, so there are six independent parameters that determine the Raman intensities.

In this thesis we have used the six polarizability parameters reported in Ref. [136]. They were obtained from the fits to the experimental off-resonance Raman spectrum of C_{60} measured by Chase *et al.* [145] and they are listed in Table 8.4.3.

Bond type	fit values (Ref. [136])
Single bond	
$(\alpha'_{\parallel} - \alpha'_{\perp})$	2.30 Å^2
$(2\alpha'_{\perp} + \alpha'_{\parallel})$	2.30 Å^2
$(\alpha_{\parallel} - \alpha_{\perp})$	1.28 Å^3
Double bond	
$(\alpha'_{\parallel} - \alpha'_{\perp})$	2.60 Å^2
$(2\alpha'_{\perp} + \alpha'_{\parallel})$	7.55 Å^2
$(\alpha_{\parallel} - \alpha_{\perp})$	0.32 Å^3

Table 8.3: *Raman polarizability parameters for C_{60} used in this thesis work (chapter 5). The six parameters are those reported in Ref. [136] and they were obtained by fitting the experimental off-resonance Raman spectrum of C_{60} measured by Chase et al. [145].*

Bibliography

[1] H. W. Kroto, J. R. Heath, S. C. O'Brien, R. F. Curl, and R. E. Smalley *Nature*, vol. 318, p. 162, 1985.

[2] W. Krätschmer, L. D. Lamb, K. Fostiropoulos, and D. R. Huffman *Nature*, vol. 347, p. 354, 1990.

[3] R. B. Fuller *"Inventions-The Patented Works of Buckminster Fuller", St. Martins, New York*, 1983.

[4] R. C. Haddon, A. F. Hebard, M. J. Rosseinsky, D. W. Murphy, S. J. Duclos, K. B. Lyons, B. Miller, J. M. Rosamilia, R. M. Fleming, A. R. Kortan, S. H. Glarum, A. V. Makhija, A. J. Muller, R. H. Eick, S. M. Zahurak, R. Tycko, G. Dabbagh, and F. A. Thiel *Nature (London)*, vol. 350, p. 320, 1991.

[5] M. Mezouar, L. Marques, J.-L. Hodeau, V. Pischedda, and M. Núñez-Regueiro, "Equation of state of an anisotropic three-dimensional c_{60} polymer: The most stable form of fullerene," *Phys. Rev. B*, vol. 68, p. 193414, Nov 2003.

[6] K. Tanigaki, T. W. Ebbesen, S. Saito, J. Mizuki, J. S. Tsai, Y. Shimakawa, Y. Kubo, and S. Kuroshiima *Nature*, vol. 352, p. 222, 1991.

[7] T. T. M. Palstra, O. Zhou, Y. Iwasa, P. E. Sulewski, R. M. Fleming, and B. R. Zegarski *Solid State Commun.*, vol. 93, p. 327, 1994.

[8] S. Margadonna and K. Prassides *J. of Solid State Commun.*, vol. 168, p. 639, 2002.

[9] M. M. Abd-Elmeguid, H. Pattyn, and S. Bukshpan *Phys. Rev. Lett.*, vol. 72, p. 502, 1994.

[10] C. M. Sung and M. F. Tai *Int. J. of Refractory Metals and Hard Materials*, vol. 15, p. 237, 1996.

[11] D. Connétable, V. Timoshevskii, B. Masenelli, J. Beille, J. Marcus, B. Barbara, A. M. Saitta, G.-M. Rignanese, P. Mélinon, S. Yamanaka, and X. Blase *Phys. Rev. Lett.*, vol. 91, p. 247001, 2003.

[12] X. Blase, C. Adessi, and D. Connétable *Phys. Rev. Lett.*, vol. 93, p. 237004, 2004.

[13] N. Breda, R. A. Broglia, G. Coló, G. Onida, D. Provasi, and E. Vigezzi *Phys. Rev. B*, vol. 62, p. 130, 2000.

[14] M. Núñez-Regueiro, O. Bethoux, J.-L. Hodeau, L. Marques, J. M. Tonnerre, and B. Bouchet-Fabre *Fullerenes: Recent Advances in the Physics and Chemistry of Fullerenes, edited by K. M. Kadish and R. S. Ruoff*, pp. 519–529, 1994.

[15] M. Núñez-Regueiro, L. Marques, J.-L. Hodeau, C. H. Xu, and G. E. Scuseria *Fullerene Polymers and Fullerene Polymer Composites, edited by P. C. Eklund and A.M. Rao*, vol. 38, p. 241.

[16] B. Sundqvist, A. Soldatov, O. Andersson, A. Lundin, and P.-A. Persson *Fullerenes: Recent Advances in the Physics and Chemistry of Fullerenes, edited by K. M. Kadish and R. S. Ruoff*, vol. 2, pp. 891–905, 1995.

[17] M. S. Dresselhaus, G. Dresselhaus, and P. C. Eklund *Science of Fullerenes and Carbon Nanotubes (San Diego: Academic)*, 1996.

[18] B. Sundqvist *Adv. in Phys.*, vol. 48, p. 1, 1999.

[19] L. Forró and L. Mihály *Rep. Prog. Phys.*, vol. 64, p. 649, 2001.

[20] R. Moret *Acta Cryst.*, vol. A61, p. 62, 2005.

[21] Y. Koike, H. Suematsu, K. Higuchi, and S. Tanuma *Solid State Commun.*, vol. 27, p. 623, 1978.

[22] M. Kobayashi and I. Tsujikawa *J. Phys. Soc. Jpn.*, vol. 46, p. 1945, 1979.

[23] Y. Iye and S. Tanuma *Phys. Rev. B*, vol. 25, p. 4583, 1982.

[24] E. A. Ekimov, V. A. Sidorov, E. D. Bauer, N. N. Mel'nik, N. J. Curro, J. D. Thompson, and S. M. Stishov *Nature*, vol. 428, p. 542, 2004.

[25] T. E. Weller, M. Ellerby, S. S. Saxena, R. P. Smith, and N. T. Skipper *Nature Physics*, vol. 1, p. 39, 2005.

[26] S. Yamanaka, E. Enishi, H. Fukuoka, and M. Yasukawa *Inorg. Chem*, vol. 39, p. 56, 2000.

[27] M. Calandra and F. Mauri *Nature Physics*, vol. 95, p. 237002, 2005.

[28] L. Marques, M. Mezouar, J.-L. Hodeau, M. Núñez-Regueiro, N. R. Serebryanaya, V. A. Ivdenko, V. D. Blank, and G. A. Dubitsky *Science*, vol. 283, p. 1720, 1999.

[29] E. Burgos, E. Halac, R. Weht, H. Bonadeo, E. Artacho, and P. Ordej/'on *Phys. Rev. Lett.*, vol. 85, p. 2328, 2000.

[30] R. C. Haddon *Acc. Chem. Res.*, vol. 25, p. 127, 1992.

[31] R. C. Haddon, L. E. Brus, and K. Raghavachari *Chem. Phys. Lett.*, vol. 125, p. 459, 1986.

[32] H. P. Lüthi and J. Almlöf *Chem. Phys. Lett.*, vol. 135, p. 357, 1987.

[33] S. Satpathy *Chem. Phys. Lett.*, vol. 130, p. 545, 1986.

[34] R. O. Jones and O. Gunnarsson *Rev. Mod. Phys.*, vol. 61, p. 689, 1989.

[35] W. E. Pickett *Solid State Physics*, vol. 48, p. 225.

[36] R. Moret, S. Ravy, and J. M. Godard *J. Phys. I (France)*, vol. 3, p. 1085, 1993.

[37] P. Launois, S. Ravy, and R. Moret *Phys. Rev. B*, vol. 52, p. 5414, 1995.

[38] L. Pintschovius, S. L. Chaplot, R. Roth, and G. Heger *Phys. Rev. Lett.*, vol. 75, p. 2843, 1995.

[39] P. Launois, S. Ravy, and R. Moret *Int. J. Mod. Phys. B*, vol. 13, pp. 253–281, 1999.

[40] B. Sundqvist, O. Andersson, A. Lundin, and A. Soldatov *Solid State Commun.*, vol. 93, p. 109, 1995.

[41] W. I. F. David, R. M. I. nd T. S. J. Dennis, J. P. Hare, and K. Prassides *Europhys. Lett.*., vol. 18, p. 219, 1992.

[42] O. Blaschko, W. Rom, and I. N. Goncharenko *J. Phys.: Condens. Matter*, vol. 8, p. 4235, 1996.

[43] S. J. Woo, S. H. Lee, E. Kim, K. H. Lee, Y. H. Lee, S. Y. Hwang, and I. C. Jeon *Phys. Lett. A*, vol. 162, p. 501, 1992.

[44] R. S. Ruoff *Nature*, vol. 350, p. 663, 1991.

[45] S. J. Duclos, K. Brister, R. C. Haddon, A. R. Kortan, and F. A. Thiel *Nature*, vol. 351, p. 380, 1991.

[46] D. W. Snoke, Y. S. Raptis, and K. Syassen *Phys. Rev. B*, vol. 45, p. 14419, 1992.

[47] M. Núñez-Regueiro, P. Monceau, and J.-L. Hodeau *Nature*, vol. 355, p. 237, 1992.

[48] A. San Miguel *Chem Soc. Rev.*, vol. 35, p. 876, 2006.

[49] V. D. Blank, S. G. Buga, G. A. Dubitsky, N. R. Serebryanaya, M. Y. Popov, and B. Sundqvist *Carbon*, vol. 36, p. 319, 1998.

[50] R. Moret, P. Launois, P. A. Persson, and B. Sundqvist *Europhys. Lett.*, vol. 40, p. 55, 1997.

[51] M. Núñez-Regueiro, L. Marques, and J.-L. Hodeau *In Physics of Fullerene-Based and Fullerene-Related Materials, edited by W. Andreoni*, vol. 23, p. 409, 2000.

[52] R. Moret, P. Launois, T. Wagberg, and B. Sundqvist *European Physical Journal B*, vol. 15, p. 253, 2000.

[53] M. Núñez-Regueiro, L. Marques, J.-L. Hodeau, O. Bèthoux, and M. Perroux *Phys. Rev. Lett.*, vol. 74, p. 278, 1995.

[54] R. Moret, P. Launois, T. Wagberg, B. Sundqvist, V. Agafonov, V. A. Davydov, and A. V. Rakhmanina *European Physical Journal B*, vol. 37, p. 25, 2000.

[55] V. D. Blank, V. M. Levin, , and N. R. Serebryanaya *JETP*, vol. 87, p. 741, 1998.

[56] L. A. Chernozatonskii, N. R. Serebryanaya, and B. N. Mavrin *Chem. Phys. Lett.*, vol. 316, p. 199, 2000.

[57] S. Yamanaka, A. Kubo, K. Inumaru, K. Komaguchi, N. S. Kini, T. Inoue, and T. Irifune *Phys. Rev. Letter*, vol. 96, p. 076602, 2006.

[58] T. Yildrim, O. Zhou, J. E. Fischer, R. A. Stronging, M. A. Cichy, A. B. Smith, C. L. Lin, and R. Jelinek *Nature*, vol. 360, p. 568, 1992.

[59] A. F. Hebard, M. J. Rosseinsky, R. C. Haddon, D. W. Murphy, S. H. Glarum, T. T. M. Palstra, A. P. Ramirez, and A. R. Kortan *Nature*, vol. 350, p. 600, 1991.

[60] R. M. Fleming, A. P. Ramirez, M. J. Rosseinsky, D. W. Murphy, R. C. Haddon, S. M. Zahurak, and A. V. Makhija *Nature*, vol. 352, p. 787, 1991.

[61] K. Prassides, C. Christides, I. M. Thomas, J. Mizuki, K. Tanigaki, I. Hirosawa, and T. W. Ebbesen *Science*, vol. 263, p. 950, 1994.

[62] P. Launois, R. Moret, E. Llusca, J. Hone, and A. Zetti *Physical Review Letters*, vol. 81, p. 4420, 1998.

[63] B. Verbeck, H. Michel, and A. V. Nikolaev *J. Chem Phys.*, vol. 23, p. 10462, 2002.

[64] M. S. Dresselhaus, G. Dresselhaus, and P. C. Eklund *Science of Fullerenes and Carbon Nanotubes (Academic Press Inc.)*, 1996.

[65] S. Margadonna, D. Pontiroli, M. Belli, M. R. T. Shikora, and M. Brunelli *J. A. Chem. Soc.*, vol. 126, p. 15032, 2004.

[66] M. Riccó, T. Shikora, M. Belli, D. Pontiroli, M. Pagliari, G. Ruani, D. Palles, S. Margadonna, and M. Tomaselli *Phys. Rev. B*, vol. 72, p. 155437, 2005.

[67] R. Röding, T. Wågberg, and B. Sundqvist *Chem. Phys. Lett.*, vol. 413, p. 157, 2005.

[68] O. Zhou, J. E. Fischer, N. Coustel, S. Kycia, Q. Zhu, A. R. McGhie, W. J. Romanow, J. P. McCauley, A. B. Smith, and D. E. Cox *Nature (London)*, vol. 351, p. 462, 1991.

[69] W. Andreoni, F. Gygi, and M. Parrinello *Phys. Rev. Lett.*, vol. 68, p. 823, 1992.

[70] S. C. Erwin and M. R. Pederson *Phys. Rev. Lett.*, vol. 67, p. 1610, 1991.

[71] A. A. Sabouri-Dodaran, M. Marangolo, C. Bellin, F. Mauri, G. Figuet, G. Loupias, M. Mezouar, W. Crichton, C. Hérold, F. Rachdi, and S. Rabii *Phys. Rev. B*, vol. 70, p. 174114, 2004.

[72] A. Filipponi, A. Di Cicco, and C. R. Natoli *Phys. Rev. B*, vol. 52, pp. 15122–15134, 1995.

[73] A. Filipponi and A. Di Cicco *Phys. Rev. B*, vol. 52, p. 15135, 1995.

[74] C. V. Raman *Indian J. Phys.*, vol. 2, p. 387, 1928.

[75] K. Nakamoto *Infrared and Raman Spectra of Inorganic and Coodination Compounds, Wiley and Sons edition.*

[76] E. B. Wilson, J. C. Decius, and P. C. Cross *Molecular vibrations, Dover edition.*

[77] P. Hohenberg and W. Kohn *Phys. Rev.*, vol. 136, p. b864, 1964.

[78] W. Kohn and L. J. Sham *Phys. Rev.*, vol. 140, p. a1133, 1965.

[79] L. Kleinman and D. M. Bylander *Phys. Rev. Lett.*, vol. 48, p. 1452, 1982.

[80] N. Troullier and J. L. Martins *Phys. Rev. B*, vol. 43, p. 1993, 1991.

[81] J. M. Besson, R. J. Nelmes, G. Hamel, J. S. Loveday, G. Weill, and S. Hull *Physica B*, vol. 180 & 181, pp. 907–910, 1992.

[82] P. Grima, A. Polina, J. P. Itiè, M. Mezouar, W. G, and J. M. Besson *J. Phys. Chem. Solids*, vol. 56, p. 525, 2005.

[83] G. Morard, M. Mezouar, N. Rey, R. Poloni, A. Merlen, S. Le Floch, P. Toulemonde, S. Pascarelli, A. San Miguel, C. Sanloup, and G. Fiquet *High Press. Res.*, vol. 27, p. 223, 2007.

[84] P. Vinet, J. R. Smith, J. Ferrante, and J. H. Rose, "Temperature effects on the universal equation of state of solids," *Phys. Rev. B*, vol. 35, pp. 1945–1953, Feb 1987.

[85] Y. Le Godec, D. Martinez-Garcia, M. Mezouar, G. Syfosse, J.-P. Itiè, and J.-M. Besson *High Press. Res.*, vol. 18, p. 339, 2000.

[86] Y. Le Godec, D. Martinez-Garcia, M. Mezouar, G. Syfosse, J.-P. Itiè, and J.-M. Besson *2000 Proc. AIRAPT-17: Science and Technology of High Pressure, edited by M. H. Manghnani, W. J. Nellis, M. F. Nicol*, vol. 9, pp. pp 925–928, 2.

[87] W. Crichton, M. Mezouar, T. Grande, S. Stolen, and A. Grzechnik *Nature*, vol. 414, pp. 622–625, 2001.

[88] A. Jayaraman *Rev. of Mod. Phys.*, vol. 55, p. 65, 1983.

[89] J. A. Xu, H. K. Mao, and P. M. Bell *Science*, vol. 232, p. 1404, 1996.

[90] J. C. Chervin, B. Canny, J. M. Besson, and P. Pruzan *Rev. Sci. Instrum.*, vol. 26, p. 2595, 1995.

[91] R. Le Toullec, J. P. Pinceaux, and P. Loubeyre *High Pressure Res.*, vol. 1, p. 77, 1988.

[92] A. V. Valkenburg *Conference International sur les Hautes-Pressions, Le Creusot, Saone-et-Loire, France, 1965.*

[93] H. K. Mao and P. M. Bell *Science*, vol. 200, p. 1145, 1978.

[94] M. I. Eremets *High Pressure Experimental Methods (Oxford University press, Oxford, 1996)*.

[95] R. A. Forman, G. J. Piermarini, and S. Bloch *Science*, vol. 176, p. 284, 1972.

[96] J. D. Barnett, S. Bloch, G. J. Piermarini, and R. A. Forman *Rev. Sci. Instrum.*, vol. 44, p. 1, 1972.

[97] G. J. Piermarini, S. Bloch, J. D. Barnett, and R. A. Forman *J. Appl. Phys.*, vol. 46, p. 2774, 1975.

[98] H. K. Mao, P. M. Bell, J. W. Schaner, and D. J. Steinberg *J. Appl. Phys.*, vol. 49, p. 3276, 1978.

[99] H. L. Ruoff *High Pressure Science and Technology, edited by Timmerhaus and M. S. Barber (Plenum New York, 1979)*, vol. 1, p. 754.

[100] H. K. Mao *Simple molecular systems at very high density, edited by P. L. A. Polian and N. Boccara (Plenum New York, 1989)*, p. 221.

[101] V. L. Vos and J. A. Schouten *J. Appl. Phys.*, vol. 69, p. 6744, 1991.

[102] E. E. Koch *Handbook on Synchrotron Radiation, North-Holland, Amsterdam*, 1983.

[103] A. Filipponi, M. Borowski, D. T. Bowron, S. Ansell, A. Di Cicco, S. De Panfilis, and J.-P. Itiè *Rev. Sci. Instr.*, vol. 71, pp. 2422–2432, 2000.

[104] G. Aquilanti, W. Crichton, and S. Pascarelli *High Press. Res.*, vol. 23, p. 301, 2003.

[105] M. Hagelstein, A. Fontaine, and J. Goulon *J. Appl. Phys.*, vol. 32, p. 240, 1993.

[106] M. Hagelstein, A. S. Miguel, A. Fontaine, and J. Goulon *J. Phys. IV, Colloque C2*, vol. 7, p. C2 303, 1997.

[107] J. Pellicer-Porres, A. San Miguel, and A. Fontaine *J. Synchrotron Rad.*, vol. 5, p. 1250, 1998.

[108] A. San Miguel, M. H. J. Borrel, G. Marot, and M. Reiner *J. Synchrotron Rad.*, vol. 5, p. 1396, 1998.

[109] R. P. Phizackerley, Z. U. Rek, B. S. G, S. D. Conradson, K. O. Hodgson, T. Matsuchita, and H. Oyanagi *J. Appl. Cryst.*, vol. 16, p. 220, 1993.

[110] M. Mezouar, W. A. Crichton, S. Bauchan, F. Thurel, H. Witsch, F. Torrecillas, G. Blattmann, P. Marion, Y. Dabin, J. Chavanne, O. Hignette, C. Morawe, and C. Borel *J. Synchrotron Rad.*, vol. 12, p. 659, 2005.

[111] A. M. Rao, P. C. Eklund, J.-L. Hodeau, L. Marques, and M. Núñez-Regueiro *Phys. Rev. B*, vol. 55, p. 4766, 1997.

[112] D. P. Hammersley, S. O. Svensson, M. Hanfland, A. N. Fitch, and D. Hausermann *High Press. Res.*, vol. 14, p. 235, 1996.

[113] O. Zhou and D. E. Cox *J. Phys. Chem. Solids*, vol. 53, p. 1373, 1992.

[114] J. Rodriguez-Carvajal *Physica B*, vol. 192, p. 55, 1993.

[115] F. D. Murnaghan *J. Matt.*, vol. 49, p. 235, 1937.

[116] P. Vinet, J. R. Smith, J. Ferrante, and J. H. Rose *Physical Review B*, vol. 35, pp. 1945–, 1987.

[117] P. Vinet, J. Ferrante, J. R. Smith, and J. H. Rose *J. Phys. C: Solid State Phys.*, vol. 19, pp. L467–, 1986.

[118] F. Birch *Phys. Rev.*, vol. 71, p. 809, 1947.

[119] A. Kodre, I. Arčon, J. P. Gomilšek, R. Prešeren, and R. Frahm *J. Phys. B: At. Mol. Opt. Phys.*, vol. 35, pp. 3497–3513, 2002.

[120] J. M. Soler, E. Artacho, J. D. Gale, A. García, J. Junquera, P. Ordejón, and D. S. Sanchez-Portal *J. Phys: Condens. Matter*, vol. 14, pp. 2745–2779, 2002.

[121] J. Junquera, O. Paz, D. Sánchez-Portal, and E. Artacho vol. 64, p. 235111, 2001.

[122] E. Anglada, J. M. Soler, J. Junquera, and E. Artacho vol. 66, p. 205101, 2002.

[123] K. Ranjan, K. Dharamvir, and V. K. Jindal *Indian J. of Pure and Applied Physics*, vol. 43, p. 654, 2005.

[124] A. San-Miguel, A. Polian, M. Gauthier, and J. P. Itié *Phys. Rev. B*, vol. 48, pp. 8683–8693, Sep 1993.

[125] J. Pellicer-Porres, A. Segura, V. Muñoz, and A. San Miguel *Phys. Rev. B*, vol. 60, pp. 3757–3763, Aug 1999.

[126] G. Dresselhaus, M. S. Dresselhaus, and P. C. Eklund *Phys. Rev. B*, vol. 45, p. 6923, 1992.

[127] G. Meijer and D. S. Bethune *Chem. Phys. Lett.*, vol. 175, p. 1, 1990.

[128] K.-A. Wang, Y. Wang, P. Zhou, J. M. Holden, S. Ren, G. T. Hager, H. F. Ni, P. C. Eklund, G. Dresselhaus, and M. S. Dresselhaus *Phys. Rev. B*, vol. 45, p. 1955, 1991.

[129] P. Zhou, K.-A. Wang, Y. Wang, P. C. Eklund, M. S. Dresselhaus, and R. A. Jishi *Phys. Rev. B*, vol. 46, p. 2595, 1992.

[130] Y. S. Raptis, D. W. Snoke, K. Syassen, S. Roth, P. Bernier, and A. Zahab *High Pres. Res.*, vol. 9, p. 41, 1992.

[131] R. E. Stanton and M. D. Newton *J. Phys. Chem.*, vol. 92, p. 2141, 1998.

[132] R. Poloni, M. V. Fernandez-Serra, S. Le Floch, S. De Panfilis, P. Toulemonde, D. Machon, W. Cricthon, S. Pascarelli, and A. San Miguel *submitted to Phys. Rev. B*, 2007.

[133] R. A. Jishi and M. S. Dresselhaus *Phys. Rev. B*, vol. 45, p. 6914, 1992.

[134] S. Fujiki, Y. Kubozono, S. Emura, Y. Takabayashi, S. Kashino, A. Fujiwara, K. Ishii, H. Suematsu, Y. Murakami, Y. Iwasa, T. Mitani, , and H. Ogata *Phys. Rev. B*, vol. 62, p. 5366, 2000.

[135] G. Lucazeau *J. of Raman Spectroscopy*, vol. 34, p. 478, 2003.

[136] S. Guha, J. Menéndez, J. B. Page, and G. B. Adams *Phys. Rev. B*, vol. 53, p. 13106, 1996.

[137] R. Poloni, D. Machon, M. V. Fernandez-Serra, S. Le Floch, S. Pascarelli, G. Montagnac, H. Cardon, and A. San Miguel *submitted to Phys. Rev. B*, 2007.

[138] M. Hagelstein, A. San Miguel, T. Ressler, A. Fontaine, and J. Goulon *J. de Physique IV*, vol. 7, p. 303, 1997.

[139] S. Pascarelli, O. Mathon, and G. Aquilanti *J. of Alloys and Comp.*, vol. 362, p. 33, 2004.

[140] N. Sata, G. Shen, M. L. Rivers, and S. R. Sutton *Phys. Rev. B*, vol. 65, p. 104114, 2002.

[141] D. Louër and R. Vargas *J. Appl. Cryst.*, vol. 15, pp. 542–545, 1982.

[142] D. H. Chi, Y. Iwasa, X. H. Chen, T. Takebonu, T. Ito, T. Mitani, E. Nishibori, M. Takata, M. Sakata, and Y. Kubozono *Chem. Phys. Lett.*, vol. 359, p. 177, 2002.

[143] T. Takenobu, D. H. Chi, S. Margadonna, K. Prassides, Y. Kubozono, A. N. Fitch, K. Kato, and Y. Iwasa *J. Am. Chem. Soc.*, vol. 125, p. 1897, 2003.

[144] M. J. Rosseinsky, A. P. Ramirez, S. H. Glarum, D. W. Murphy, R. C. Haddon, A. F. Hebard, T. T. M. Palstra, A. R. Kortan, S. M. Zahurak, and A. V. Makhija *Phys. Rev. Lett.*, vol. 66, pp. 2830–2832, 1991.

[145] B. Chase, N. Herron, and E. Holler *J. Phys. Chem.*, vol. 96, p. 4262, 1992.

Fullerènes intercalées avec des métaux alcalins lourds sous haute pression et haute température: Rb_6C_{60} and Cs_6C_{60}

Dans cette thèse nous explorons le diagramme de phase des fullerènes intercalées avec des métaux alcalins lourds, Rb_6C_{60} and Cs_6C_{60}, à très haute pression (up to 50 GPa) et à très haute température (de l'ambiante à 1500 K).

Ce travail inclue des expériences d'absorption de rayons X, de diffraction de rayons X, de spectroscopie Raman, ainsi que des calculs DFT *ab initio* à haute pression.

Le couplage entre expériences et calculs permet d'observer que la présence de la forte interaction ionique entre chaque molécule et les ions alcalins, empêche la polymérisation des fullerènes sous pression. Dans le cas de Cs_6C_{60}, ceci a permis d'étendre le domaine de stabilité en pression des molécules de C_{60} d'au moins un facteur deux par rapport aux cristaux de C_{60} non-intercalés. Dans le cas de Rb_6C_{60} une transition réversible est observée à 35 GPa.

Nous avons mis en évidence la déformation progressive de la molécule de fullerène sous pression dans les systèmes étudiès. La compressibilité des deux cristaux a été mesurée et calculée.

DISCIPLINE

Physique

MOTS CLES

C_{60}, fullerènes intercalées, diagramme de phase, diffraction de rayons X, absorption de rayons X, spectroscopie Raman, calculs *ab initio*, haute pression.

INTITULE ET ADRESSE DE L'U.F.R. OU DU LABORATOIRE

Université Claude Bernard - Lyon 1

Laboratoire de Physique de la Matière Condensé et Nanostructures

43 Bvd du 11 Novembre 1918

F-69622 Villeurbanne, Cedex